

DISS. ETH No. 27169

**SENSIBLE THERMAL-ENERGY STORAGE
FOR ADIABATIC COMPRESSED AIR
ENERGY STORAGE PLANTS: DESIGN AND
OPTIMIZATION**

A thesis submitted to attain the degree of
DOCTOR OF SCIENCES of ETH ZURICH
(Dr. sc. ETH Zurich)

presented by

PHILIPP ROOS

MSc ETH ME

born on 09.11.1990

citizen of Entlebuch (LU)

accepted on the recommendation of

Prof. Dr. Aldo Steinfeld, examiner

Prof. Dr. Christos Markides, co-examiner

Dr. Andreas Haselbacher, co-examiner

2021

ABSTRACT

This thesis investigates sensible thermal-energy storage (TES) for advanced adiabatic compressed air energy storage (AA-CAES) using analytical and numerical models.

TES using packed-beds of fluvial rocks have been shown to offer high exergy efficiencies at low costs, but the formation of a temperature profile across the packed-bed, a so-called thermocline, and its degradation over time, leads to outflow-temperature differences during charging and discharging resulting in detrimental performance of downstream applications. In AA-CAES plants, this causes potential structural damage to the air storage volume during charging and decreasing turbine power during discharging.

The goals of this thesis are fourfold. First, thermocline-control (TCC) methods with a focus on AA-CAES specific operating conditions are assessed regarding their performance gains. Second, AA-CAES plants are assessed by means of an analytical model to advance the understanding of the physics involved and to provide fast estimates of plant performance and layouts regarding cavern and TES sizes. Third, AA-CAES plants are assessed numerically under quasi-steady-state (QSS) conditions and using TCC to achieve constant power, and under variable grid operating conditions to gain insights into the potential problems that arise under these conditions. Finally, the use of a numerical optimization algorithm is analyzed with the goal of automating the plant design process.

Two TCC methods, extraction and mixing TCC, implemented by con-

necting multi-tank TES (MTTES) with pipes and valves are assessed. The concept of MTTES is interesting to AA-CAES because it enables the use of smaller tanks that potentially enable smaller cavern diameters, and it potentially provides operational flexibility. The numerical assessment includes adiabatic and diabatic conditions, and compares single-tank TES to MTTES systems consisting of two, three, and four tanks. For adiabatic conditions, the simulations show improved performance for all multi-tank systems, with diminishing improvements as the number of tanks increases. The mixing method performs better than the extraction method. The mixing method delivers an outflow temperature drop of 5.1% using two tanks whose total volume is 2.15 times smaller than that of the single-tank system. For diabatic conditions, more than three tanks are not beneficial. With two tanks, the mixing method attains a temperature drop of 5.8% with a volume that is 2.5 times smaller than that of the single-tank system. The exergy efficiency of the two-tank system is 91.3% compared to 98.1% of the single-tank system. The specific material costs of the two-tank system are 1.5 times lower than those of the single-tank system.

The analytical plant model is developed based on deriving QSS equations at the end of charging and discharging of the plant for isochoric caverns. The resulting model enables the estimation of key performance indicators such as the efficiency and volumetric energy density with closed-form expressions using component efficiencies and pressure ratios for one- and two-stage AA-CAES plants. The model can be used to obtain initial plant designs in terms of the plant efficiency and required storage and TES volume using only pressure ratios, component efficiencies, and the required storage capacity. The model also enables insights into the physics of the plant behavior, with the most important point, that a two-stage plant exhibits an efficiency minimum due to the turbine at symmetrical compression ratios for the low- and high-pressure cavern, equal to the square root of the maximum high-pressure compression ratio. This is a somewhat unfortunate result because such a setup is favorable due to equal compression work of the low- and high-pressure compressor at the end of charging, leading to lower

construction costs.

The newly developed numerical AA-CAES plant model is verified using the analytical plant model and used for the assessment of power control using MTTES with mixing TCC. The assessment is conducted by sizing the plant with the analytical plant model and comparing the single-tank TES plant performance at QSS providing unsteady power output with a plant equipped with MTTES in the high- and low-pressure caverns at QSS providing constant power output. The results show that the numerical simulations including thermal losses and idle periods lie within 7% of the predicted efficiency and discharge energy capacity of the analytical model. The plant using MTTES achieves an efficiency of 69.3% and a discharge capacity of 464 MWh under diabatic conditions in a 24-hour storage cycle providing constant charge and discharge power, which, compared to the plant equipped with single-tank TES, is only 3% lower. Additionally, the performance of a plant equipped with MTTES is assessed under variable operating conditions, where the turbine power is only controlled by the inflow temperature. The results prove the suitability of this approach, enabling constant output powers at varying power levels and following a load curve, but overheating of the MTTES system is identified as a potential problem.

The numerical optimization algorithm is used to optimize an AA-CAES plant with a weighted objective function including the plant efficiency and costs. A verification with the analytical plant model is presented to increase the trustworthiness of the optimization, showing that analytically predicted maxima and minima are found with sufficient accuracy. The optimizations of the plant are performed using turbomachinery efficiency maps and simplified TES models with the optimizer choosing the high- and low-pressure cavern pressure ratios, and the high-pressure cavern length for objective weights ranging between 0 and 1. The results are presented as Pareto fronts and show clear trade-offs between the plant costs and efficiency, for example enabling a potential cost reduction of 48% resulting in an efficiency drop from 76.8% to 75%. The results underline the potential usefulness of numerical optimization for AA-CAES plants and TES.

ZUSAMMENFASSUNG

Diese Arbeit untersucht sensible Wärmespeicher für den Einsatz in adiabatischen Druckluftspeicherkraftwerken mithilfe von analytischen und numerischen Modellen.

Sensible Festbett-Wärmespeicher weisen hohe Exergieeffizienzen bei geringen Kosten auf, aber die Bildung eines Temperaturprofils über dem Speicher, eine sogenannte Thermokline, und deren Ausbreitung im Laufe der Zeit führt am Auslass zu einem Temperaturanstieg beim Laden und einem Temperaturabfall beim Entladen, was bei nachfolgenden Komponenten zu Leistungseinbußen führen kann. In Druckluftspeicherkraftwerken führt dies zu einer möglichen Beschädigung des Luftspeichervolumens während des Ladens und zu einer Verringerung der Turbinenleistung während des Entladens.

Die Ziele dieser Arbeit können in vier Punkte unterteilt werden. Zunächst werden Methoden zur aktiven Beeinflussung der Thermokline mit einem Schwerpunkt auf Druckluftspeicherkraftwerk-spezifischen Betriebsbedingungen untersucht und aufgrund ihrer Leistungssteigerungen bewertet. Zweitens werden Druckluftspeicherkraftwerke mithilfe eines analytischen Modells analysiert, um das physikalische Verständnis zu verbessern und schnelle Abschätzungen der Anlagenleistung und des Anlagenlayouts mit Bezug auf Kavernen- und Wärmespeicher-Größen zu liefern. Drittens werden Druckluftspeicherkraftwerke unter quasi-stationären und variablen Bedingungen unter Verwendung von aktiven Thermokline-Regelmethoden zur Erzielung einer konstanten Turbinenleistung numerisch analysiert. Schließlich wird

die Verwendung eines numerischen Optimierungsalgorithmus mit dem Ziel analysiert, den Anlagenentwurfsprozess zu automatisieren.

Es werden zwei Thermokline-Regelmethode bewertet, die Extraktions- und Mischverfahren, die durch Verbinden von mehreren Wärmespeichern mit Rohren und Ventilen implementiert werden. Das Konzept von Mehrfach-Wärmespeichern ist für Druckluftspeicherkraftwerke interessant, da es die Verwendung kleinerer Tanks ermöglicht, die möglicherweise kleinere Kavernen-Durchmesser ermöglichen, und Flexibilität bietet, nur einzelne Wärmespeicher für kurze Betriebsphasen zu verwenden. Die numerische Bewertung umfasst adiabatische und diabatische Bedingungen und vergleicht Wärmespeicher mit einem Tank mit Mehrfach-Wärmespeichern, die aus zwei, drei und vier Tanks bestehen. Unter adiabatischen Bedingungen zeigen die Simulationen eine verbesserte Leistung für alle Mehrfach-Wärmespeicher, wobei die Verbesserungen mit zunehmender Anzahl von Tanks abnehmen. Das Mischverfahren ist besser als das Extraktionsverfahren. Die Mischmethode liefert einen Auströmtemperaturabfall von 5.1% unter Verwendung von zwei Tanks, deren Gesamtvolumen 2.15-mal kleiner ist als das des Einzeltanksystems. Bei diabatischen Erkrankungen sind mehr als drei Wärmespeicher nicht vorteilhaft. Bei zwei Tanks erreicht die Mischmethode einen Temperaturabfall von 5.8% bei einem Volumen, das 2.5-mal kleiner ist als das des Einzeltanksystems. Die Exergieeffizienz des Zwei-Tank-Systems beträgt 91.3% gegenüber 98.1% des Ein-Tank-Systems. Die spezifischen Materialkosten des Zwei-Tank-Systems sind 1.5-mal niedriger als die des Ein-Tank-Systems.

Das analytische Druckluftspeicherkraftwerk-Anlagenmodell basiert auf der Aufstellung von Gleichungen am Ende des Ladens und Entladens des Kraftwerks für isochore Kavernen unter quasi-stationären Bedingungen. Das resultierende Modell ermöglicht die Abschätzung von Leistungsindikatoren wie dem Wirkungsgrad und der volumetrischen Energiedichte mit Ausdrücken in geschlossener Form unter Verwendung von Komponenteneffizienzen und Druckverhältnissen für ein- und zweistufige Druckluftspeicherkraftwerke. Das Modell kann verwendet werden, um erste Anlagenauslegungen hinsichtlich

der Effizienz und des erforderlichen Speicher- und Wärmespeicher-Volumens zu erhalten, wobei nur Druckverhältnisse, Komponenteneffizienzen und die erforderliche Speicherkapazität benötigt werden. Das Modell ermöglicht auch Einblicke in die Physik des Anlagenverhaltens, wobei der wichtigste Punkt darin besteht, dass eine zweistufige Anlage aufgrund der Turbine bei symmetrischen Verdichtungsverhältnissen für die Nieder- und Hochdruckkaverne, errechnet durch die Quadratwurzel des maximalen Hochdruckkompressionsverhältnisses, ein Minimum des Wirkungsgrades aufweist. Dies ist ein etwas unglückliches Ergebnis, da ein solcher Aufbau aufgrund der gleichen Kompressionsarbeit des Nieder- und Hochdruckkompressors am Ende des Ladevorgangs zu bevorzugen ist, da dies zu niedrigeren Baukosten führt.

Das neu entwickelte numerische Druckluftspeicher-Anlagenmodell wird anhand des analytischen Anlagenmodells verifiziert und zur Bewertung der Leistungsregelung mit Mehrfach-Wärmespeichern mit dem Mischverfahren verwendet. Die Bewertung erfolgt durch Dimensionierung der Anlage mit dem analytischen Anlagenmodell und Vergleich der Leistung einer konventionellen Anlage mit einem Wärmespeicher bei quasi-stationären Bedingungen, die eine abfallende Turbinenleistung liefert, mit einer Anlage, die mit Mehrfach-Wärmespeichern in den Hoch- und Niederdruckkavernen ausgestattet ist bei quasi-stationären Bedingungen und eine konstante Leistung liefert. Die Ergebnisse zeigen, dass die numerischen Simulationen einschließlich Wärmeverlusten und Wartezuständen innerhalb von 7% des vorhergesagten Wirkungsgrads und der Energiekapazität des analytischen Modells liegen. Die Anlage mit Mehrfach-Wärmespeichern erreicht unter diabatischen Bedingungen in einem 24–Stunden-Speicherzyklus einen Wirkungsgrad von 69.3% und eine Entladekapazität von 464 MWh bei konstanter Lade- und Entladeleistung was im Vergleich zur Anlage mit Einzeltanksystem nur 3% niedriger ist. Zusätzlich wird die Leistung einer mit Mehrfach-Wärmespeicher ausgestatteten Anlage unter variablen Betriebsbedingungen bewertet, bei denen die Turbinenleistung nur durch die Einströmtemperatur gesteuert wird. Die Ergebnisse belegen die Eignung dieses Ansatzes, der konstante Turbinenleistungen bei unterschiedlichen Leistungsstufen einer Lastkurve

folgend ermöglicht. Eine Überhitzung des MTTES-Systems wird jedoch als potenzielles Problem identifiziert.

Der numerische Optimierungsalgorithmus wird verwendet, um ein Druckluftspeicherkraftwerk mit einer gewichteten Zielfunktion gebildet aus der Anlageneffizienz und den Kosten zu optimieren. Eine Überprüfung mit dem analytischen Anlagenmodell wird präsentiert, um die Vertrauenswürdigkeit der Optimierung zu erhöhen. Dies zeigt, dass analytisch vorhergesagte Maxima und Minima mit ausreichender Genauigkeit gefunden werden. Die Optimierungen der Anlage werden unter Verwendung von variablen Turbomaschinen-Effizienzen und vereinfachten Wärmespeicher-Modellen durchgeführt, wobei der Optimierer die Hoch- und Niederdruckkavernen Druckverhältnisse und die Hochdruckkavernenlänge für Zielgewichte zwischen 0 und 1 auswählt. Die Ergebnisse werden als Pareto-Fronten dargestellt und zeigen klare Kompromisse zwischen den Anlagenkosten und der Effizienz. Dies ermöglicht beispielsweise eine potenzielle Kostenreduzierung von 48%, was zu einem Effizienzabfall von 76.8% auf 75% führt. Die Ergebnisse unterstreichen den potenziellen Nutzen der numerischen Optimierung Druckluftspeicher-Anlagen und Wärmespeicher.

ACKNOWLEDGEMENTS

I would like to thank Prof. Aldo Steinfeld for the opportunity to conduct my doctoral studies under his supervision at the Professorship of Renewable Energy Carriers (PREC) at ETH Zurich.

I am thankful to Prof. Christos Markides, Professor of Clean Energy Technologies at the Imperial College London, for serving as co-examiner of this thesis.

I would like to thank Dr. Andreas Haselbacher, my direct supervisor and co-examiner of this thesis, for his excellent support, guidance and patience.

Special thanks go to the project partners of the SCCER phase II, Giw Zanganeh from ALACAES, Maurizio Barbato and Jonathan Roncolato from SUPSI, Alexander Fuchs, Jared Garrison, and Turhan Demiray from FEN, Philipp Jenny, Martin Scholtysik, and Emmanuel Jacquemoud from MAN Energy Solutions, Michel Arnal from BKW, and Warren Schenler from PSI.

I want to thank all former and current members of the PREC group at ETH for the fun times, their support and scientific discussions and advice. Special thanks go to my former office buddies Dr. Fabian Dähler, who will be remembered dearly as a remarkable, brilliant, and kind colleague and friend, and Michael Wild, thank you for the fun times, valuable scientific advice and discussions, and the coffee breaks and game nights.

I gratefully acknowledge the work done by the students Pablo Gassmann, Dimitrios Tziritas, and Chia-Ling Yang, performing their Master theses, and Saskia Kohler, Pablo Gassmann, and Maciej Szybiak performing their

Semester theses under my supervision.

I am grateful for the funding by Innosuisse through the Swiss Competence Center for Energy Research on Heat and Electricity Storage that made this work possible.

Finally, I am extremely grateful for my family and friends, for their support and love. I want to thank my grandfather Amandus for his help and guidance, my grandmother Beate for always believing in me, my father Kurt for his love and support, and Leandra for your love, support and patience.

CONTENTS

Abstract	i
Zusammenfassung	v
Acknowledgements	ix
Contents	xi
Nomenclature	xv
1 Introduction	1
1.1 Energy storage and its role in a carbon-free future	1
1.2 Thermal-energy storage for AA-CAES	4
1.3 AA-CAES plant design	5
1.3.1 Analytical plant model	7
1.3.2 Numerical plant model	8
1.3.3 AA-CAES system integration	8
1.4 Numerical optimization algorithm as design tool	9
2 Multi-tank thermal-energy storage	11
2.1 Introduction	11
2.2 Operation of MTTES systems	15
2.2.1 Basic operating modes	15

2.2.2	Extraction method	17
2.2.3	Mixing method	20
2.3	Assessment strategy	25
2.4	Assessment of MTTES systems	28
2.4.1	Operating conditions and simulation parameters	28
2.4.2	Adiabatic conditions	31
2.4.3	Diabatic conditions	38
2.5	Summary, conclusions, and future work	44
3	Analytical modeling of AA-CAES plants	47
3.1	Introduction	47
3.2	One-stage plant	53
3.2.1	Plant layout, assumptions, and implications	53
3.2.2	Cavern and turbomachinery models	55
3.2.3	Plant efficiency	60
3.2.4	Storage capacity and density	63
3.2.5	Cavern volume	65
3.2.6	Discussion	66
3.3	Two-stage plant	69
3.3.1	Plant layout, assumptions, and implications	70
3.3.2	Cavern and turbomachinery models	73
3.3.3	Plant efficiency	76
3.3.4	Compressor and turbine work	81
3.3.5	Storage capacity and density	84
3.3.6	Cavern volumes	84
3.3.7	Energy breakdown	89
3.3.8	Discussion	93
3.4	Summary, conclusions, and future work	97
4	Numerical investigation of AA-CAES plant design	101
4.1	Introduction	101
4.2	Model description	106
4.2.1	Compressor	106

4.2.2	Turbine	107
4.2.3	TES	108
4.2.4	Cavern	109
4.2.5	Heat exchanger and re-heater	109
4.2.6	Throttling valve	110
4.3	Plant layout	110
4.4	Operation modes	113
4.5	Plant sizing	113
4.6	Performance assessment	117
4.7	Results	118
4.7.1	Verification	118
4.7.2	Quasi-steady operating conditions	119
4.7.3	Variable operating conditions	135
4.8	Summary, conclusions, and future work	139
5	Multi-objective optimization of AA-CAES plants	143
5.1	Introduction	143
5.2	Design method	145
5.2.1	AA-CAES and TES model	145
5.2.2	Optimization package	147
5.2.3	Coupling	147
5.3	Formulation of optimization problems	150
5.4	Results	153
5.4.1	Verification	153
5.4.2	Constant efficiencies	154
5.4.3	Variable efficiencies	157
5.5	Summary, conclusions, and future work	160
6	Conclusions and recommendations for future work	161
6.1	Multi-tank thermal-energy storage	161
6.2	Analytical modeling of AA-CAES	163
6.3	Numerical modeling of AA-CAES	164
6.4	Numerical optimization	166

A Numerical model	167
List of figures	171
List of tables	179
Bibliography	181
Curriculum vitae	193
List of publications	195

NOMENCLATURE

Latin Symbols

A	cross section area	m^2
c	specific heat capacity	J/kgK
E	energy	J
H	height	K
h	enthalpy	J/kg
i	index	–
k	thermal conductivity	W/mK
N	number	–
p	pressure	bar
Q	heat flow rate	W
R	specific gas constant	J/kgK
R	upper radius	m
r	lower radius	m
S	surface area	m^2
s	entropy	J/kg
T	temperature	K
t	time	s
V	volume	m^3
W	work	W
x	axial coordinate	m

Greek Symbols

Δ	difference	
ϵ	relative error	—
ϵ	void fraction	—
η	efficiency	—
γ	specific heat ratio	—
Ω	outlet temperature tolerance	K
ρ	density	kg/m ³
Θ	cycling tolerance	—
Ξ	exergy	J
ξ	integration variable	—
ζ	utilization factor	—

Superscripts

$(\dot{\cdot})$	rate
$(\overline{\cdot})$	temporal average
$(\widetilde{\cdot})$	non-dimensional
c	charge
d	discharge

Subscripts

atm	atmospheric
cav	cavern
el	electric
ex	exergetic
gen	generator
hp	high-pressure
int	intermediate
in	inflow
limit	limit value
lp	low-pressure
max	maximum
min	minimum

<i>mot</i>	motor
<i>net</i>	net quantity
<i>out</i>	outflow
<i>ref</i>	reference
<i>target</i>	target value
<i>th</i>	thermal
<i>total</i>	total quantity
<i>c</i>	charge
<i>c</i>	compressor
<i>d</i>	discharge
<i>e</i>	exact
<i>f</i>	fluid
<i>m</i>	mechanical
<i>p</i>	polytropic
<i>s</i>	isentropic
<i>s</i>	solid
<i>t</i>	total
<i>t</i>	turbine

Abbreviations

AA-CAES	advanced adiabatic compressed air energy storage
CAES	compressed air energy storage
CASSI	compressed air storage simulation
CSP	concentrated solar power
D-CAES	diabatic compressed air energy storage
EB	extreme boundary
HPC	high-pressure compressor
HPT	high-pressure turbine
HTF	heat-transfer fluid
HX	heat exchanger
I-CAES	isothermal compressed air energy storage
KPI	key performance indicator

LDC	low-density concrete
LPC	low-pressure compressor
LPT	low-pressure turbine
MADS	mesh adaptive direct search algorithm
MTTES	multi-tank thermal-energy storage
NOMAD	nonlinear optimization with the MADS algorithm
PB	progressive boundary
PHS	pumped hydro storage
QSS	quasi-steady-state
TCC	thermocline control
TES	thermal-energy storage
TIM	turbine inlet mass flow
TIP	turbine inlet pressure
TIT	turbine inlet temperature
UHPC	ultra-high-performance concrete
VIGV	variable inlet guide vanes

INTRODUCTION

1.1 Energy storage and its role in a carbon-free future

Limiting global warming to 1.5 °C above pre-industrial levels is projected to decrease the potential environmental impacts and risks according to the IPCC [1] and is the main target stipulated in the Paris Agreement [2]. Achieving this ambitious target requires global CO₂ emissions to reach net zero at the latest by the year 2055. Following this treaty, the European Union plans to cut carbon emissions by 80 – 95% until the year 2050 [3]. Switzerland follows a similar path with the “Energy Strategy 2050”, and the decision of the federal council to pursue the goal of net-zero carbon emissions by 2050 [4].

The key driver for the decarbonization of the economies and societies in Europe is electricity generation from renewable sources [5], enabling both the reduction of the carbon footprint of power generation, and the reduction of carbon emissions through electrification in the transport, industry and residential sectors. This results in a tremendous challenge for the power

sector, which has to simultaneously transform its energy sources and handle increased electricity demand from electrification. The bright side of this challenge ahead is the fact that water, wind, and solar electricity generation is becoming economically competitive compared to conventional, fossil electricity generation [6, 7] and the fact that renewable energy sources are abundant, exemplified by roughly 0.74% of global land area that would be required to power the world with solar energy [8].

A part of the challenge regarding renewable energy sources is their intermittent nature, making it difficult for existing energy systems to match supply and demand. A possible solution is offered by energy-storage systems, which, if widely adopted, are capable of balancing the intermittent electricity supply with demand [7]. Today, the overarching majority of existing large-scale energy storage systems are pumped hydro electricity storage (PHS) plants, amounting to more than 98% of existing storage systems larger than 10 MW [9]. The situation is similar in Europe, where PHS accounts for about 49 GW and 1313 GWh of power and capacity, respectively, with the former corresponding to about 5% of Europe's total generation capacity [10], indicating that currently there is not enough storage capacity to integrate large amounts of renewable energy. It is estimated that for a net-zero carbon emission European energy system up to 80 GW of additional electricity storage generation capacity could be necessary [11]. Even though the technical potential for new PHS plants is considerable [12], other forms of occupation, such as tourism and natural conservation areas, often stand in the way of new PHS projects, motivating the search for alternative solutions.

A promising potential alternative is compressed air energy storage (CAES), a technology that is based on a separated Brayton cycle, usually in the form of a gas turbine where the compression and expansion steps are disconnected. Such a plant can store electrical energy by driving the compressor with an electric motor, storing the compressed air in a storage volume, and generating electrical energy later by expanding the compressed air from the storage volume in the turbine that is driving a generator. The advantages compared to PHS are that CAES is not as geographically limited

because the storage volume can be built underground through leeching of salt deposits or excavating rock caverns for large applications and at a smaller scale also artificial storage volumes, such as steel tanks, are feasible [13], and that it has been shown to be economically competitive [14]. CAES can be divided in three concepts based on their idealized thermodynamic compression and expansion pathways:

- Diabatic CAES (D-CAES): The compression heat is rejected to the ambient during the charging process, leaving ambient temperature air flowing into the storage volume. During discharging, the air from the storage volume is re-heated by burning fossil fuels before entering the turbine. This is the state-of-the-art technology represented by the only two existing commercial plants to date, namely Huntorf, located in Germany, operational since 1978, with a power rating of 60 MW and 290 MW for the compressor and turbine respectively, and a discharge capacity of 642 MWh [15, 16], and McIntosh, located in the US, operational since 1991, with a power rating of 50 MW and 110 MW for the compressor and turbine respectively, and a discharge capacity of 2640 MWh [16]. Typical round-trip efficiencies for D-CAES lie in the range of 42 – 54%, depending on the use of the exhaust heat of the turbine. The rather low efficiency and the necessity to burn fossil fuels make this technology noncompetitive for today’s standards.
- Advanced adiabatic CAES (AA-CAES): The compression heat is captured in a thermal-energy storage (TES) during charging, and the air is re-heated by the TES during discharging before expansion, eliminating the need to burn fossil fuels. This also increases the round trip-efficiency which is projected to reach 65 – 75%, depending on the studies, their assumptions, and system designs [16, 17, 18, 19, 20]. These are only projections because no pilot or commercial project has presented quantitative experimental results for the round-trip efficiency.
- Isothermal CAES (I-CAES): This concept is based on isothermal compression and expansion, which requires heat removal and heat addition

during the compression and expansion, respectively, to prevent temperature changes. The technological complexity of I-CAES make it the least mature concept and it is mostly researched at smaller scales with prototypes and theoretical studies [16]

Following this short concept presentation it becomes clear that for large-scale, emission-free energy storage only AA-CAES can be considered as a realistic contender in the short to medium term. Research on AA-CAES can be categorized by the boundaries of the analyses, resulting in research projects being conducted on (1) component, mostly TES, (2) plant, and (3) system integration levels. All three levels are covered in more or less detail in this thesis and a detailed introduction and outline will be given in sections 1.2 to 1.4.

1.2 Thermal-energy storage for AA-CAES

TES is a key component of AA-CAES, but so far this topic has received not a lot of attention compared to research on concentrated solar power (CSP) plants, where this topic has been broadly covered [21, 22]. Following the insights on CSP, general requirements for TES are high efficiency, low costs, high cycle stability, low environmental impact, and high energy density. An additional requirement is defined by comparing the D-CAES and AA-CAES concepts. In D-CAES, the fossil fuel burner upstream of the turbine the turbine is a control element for the power output of the plant, which is a necessity for grid operation [23]. The TES in an AA-CAES plant can be considered a replacement of the burner, requiring the TES to have some temperature control mechanism as well. Suitable TES technologies that meet those requirements can be identified by considering the classifications and characteristics of existing TES concepts, which include sensible, latent, and thermochemical storage with direct or indirect contact between the heat transfer fluid (HTF) and the storage material [24].

Thermochemical and latent storage concepts offer high energy densities and enable temperature control [25, 26], but especially at high temperatures

their development is still in an early stage, leading to high costs, unknown long-term stability and uncertain efficiency. On the contrary, sensible storage concepts are the state-of-the-art technology, with applications ranging from two-tank molten-salt systems for CSP [22], steam accumulators for steam turbines [27], to packed beds with air as HTF used for process heat [28]. They offer energy-efficient solutions at comparably low-costs and high cycle stability. Previous work on an AA-CAES pilot experiment has shown packed-bed TES using rocks as storage material with direct heat transfer between the packed bed and air as HTF to be an efficient and cost effective solution [19, 29]. However, an inherent drawback of packed-bed TES is the formation of a thermal gradient, a so-called thermocline, forming between the inlet and outlet of the TES, which degrades over time. This can result in considerable temperature drops during discharging and decreased volumetric storage densities [29]. This problem can be addressed by implementing thermocline-control (TCC) methods, which divide a packed bed into segments and control the HTF flow through those segments to decrease the thermocline degradation, which also enables outflow temperature control [30, 31, 32, 33].

In chapter 2 of this thesis, a new implementation strategy for TCC methods is presented for packed-bed, multi-tank TES (MTTES) and assessed with a focus on AA-CAES specific operating conditions.

1.3 AA-CAES plant design

AA-CAES plant design studies so far mostly focused on quasi-steady operation, where the efficiency for a repeating charge, discharge cycle is evaluated, see Hartmann et al. [34], Barbour et al. [35], Tola et al. [18]. Most studies predict efficiencies in the range of 65 – 75%, and some include investigations on off-design behavior, such as the work from Sciacovelli et al. [17]. These assessments are mostly based on models that numerically integrate the governing equations describing the plant components, including varying degrees of model verification and validation. This is unsatisfactory for four reasons. First, numerical analyses are usually tailored to specific problems,

for example a specific plant design, which makes it difficult to draw universal conclusions that could be applied to other research projects. Second, code verifications should always be performed when new numerical models are presented and they are most valuable when authors use the same or at least similar analytical solutions. Third, validations are valuable, but often difficult to accomplish. In the case of AA-CAES it is especially difficult due to the lack of existing commercial or pilot AA-CAES plants and the low-quality and quantity of data from existing plants such as the Huntorf operational data presented by Crotogino et al. [15]. Notable exceptions are the works presented by Wang et al. [36], who showed results for a $500 \text{ kW}_{\text{el}}/326 \text{ kWh}_{\text{el}}$ pilot plant with water as HTF and storage medium and reported a plant efficiency of 22.6%, and the work of Geissbühler et al. [19] and Becattini et al. [20] who also experimentally tested at pilot-scale, without the inclusion of turbomachinery, providing a proof-of-concept and validation data for the pressurized hard-rock cavern and sensible and latent TES. Because of the already large scale of such pilot plant projects, often authors limit their validation efforts to individual components, for example the TES or the compressed air storage volume, see for example Sciacovelli et al. [17]. And fourth, AA-CAES plants are unlikely to be operated in a quasi-steady operating schedule, for example with one complete charge and discharge cycle on a 24-hour basis. It is much more likely that such a plants operating schedule is dictated by the electricity market of the electricity network to which the plant is connected, requiring a plant design that is tailored to the environment it operates in. Rouindej et al. [23, 37] presented such a data-driven design study of AA-CAES plants and could show that depending on the performance requirements a plant could be built considerably smaller.

This thesis addresses points one, two, and four, by first, developing an analytical model for a generalized AA-CAES plant, second, by using this analytical model to verify a newly developed numerical AA-CAES plant model and use the numerical model to estimate quasi-steady performance, and third, by assessing the impact of variable operating schedules on the plant performance with the use of MTTES. A detailed introduction to these

three points will be given in sections 1.3.1 to 1.3.3.

1.3.1 Analytical plant model

Analytical models for AA-CAES are based on the governing equations describing the physics involved in the plants charge and discharge process. The equations include for example the energy and mass balance of the cavern, and governing equations of the compressor, turbine, TES, and heat exchangers. By integrating these equations in time, a solution for the quasi-steady-state of the system, describing plant performance indicators, can be found, but because the exact analytical solution of such time integrals is often impossible to find, many simplifying assumptions are usually necessary. This means that such analytical models are not replacing numerical models, but that they are complementary, provided the analytical solution is accurate enough, by providing general insights into how the performance indicators behave with changing boundary conditions, and by providing a tool to quickly establish a rough system design for a given set of requirements.

Literature on analytical modeling of AA-CAES is quite limited, but mentionable examples are the works of Zaugg [38], Glendenning [39], Frutschi [40], and Grazzini and Milazzo [41]. None of these references presented a complete AA-CAES model, with Zaugg [38] omitting the charging process, Glendenning [39] and Frutschi [40] only considering constant-pressure air storage volumes, and Grazzini and Milazzo [41] excluding the temperature effects inside the air storage volume.

This thesis set the goal to develop a generalized analytical AA-CAES model that accurately describes the most important physical aspects of the plant, therefore making it suitable for general performance predictions, finding initial plant designs, and the verification of numerical models. The resulting analytical plant model is presented in chapter 3.

1.3.2 Numerical plant model

Numerical integration of the plant's governing equations makes it possible to include more complexity, such as time-dependent mass flow rates, thermal losses of the TES, or variable efficiencies of the turbomachines, which enables getting results that are closer to reality. This makes numerical models the tool of choice, if a detailed plant design has to be found and evaluated. Many research papers have dealt with numerical modeling of AA-CAES in the past. Many of them investigated the quasi-steady performance of different types of AA-CAES plant layouts, see Wolf [42], Hartmann et al. [34], Barbour et al. [35] and Tola et al. [18], but only few studies included off design conditions like the work presented by Sciacovelli et al. [17].

In this thesis, a newly developed numerical plant model is presented, verified with the analytical plant model introduced in section 1.3.1, and used to predict the plant performance of a specific AA-CAES plant layout that was drafted with the goal of using industrial, already existing components.

The resulting model and assessment is presented in chapter 4 and available as open-source project [43].

1.3.3 AA-CAES system integration

System integration requires the boundaries of the analysis to be increased. In the case of AA-CAES, or any electricity storage device for that matter, this requires the inclusion of the electricity grid to which the plant is connected to. Previous studies by Rouindej et al. [23, 37] analyzed grid data with a focus on statistics to extract operating requirements for AA-CAES plants. Their results showed that depending on the user-defined targets for the plant, the main sizing parameters of storage capacity and charging, discharging power, vary significantly. For example, they showed that a turbine with 10% of the maximum considered power rating covers 50% of the generation requirement, and 13% of the maximum compressor power rating covers 50% of the charging requirement.

Zhao et al. [44] and Sciacovelli et al. [17] included off-design performance of the compressors and turbines for different loads. Both concluded, Zhao et al. [44] for D-CAES and Sciacovelli et al. [17] for AA-CAES, that considering off-design component performance decreases the plant efficiency once varying loads below the design value are requested.

This shows that it is crucial to consider the environment the plant is operating in, for which an analysis is presented in chapter 4.

1.4 Numerical optimization algorithm as design tool

The design space of AA-CAES is vast. Considering power ratings of turbomachinery, TES geometries, cavern volumes, and operating parameters, brute-force simulations become impractical very quickly. This is where numerical optimization algorithms can help to decrease the computational time and potentially enable insights to design regions that are not obvious.

Numerical optimization approaches have been shown to be suitable design methods for TES, see Marti et al. [45], and CAES, see Ahrens et al. [46], Succar et al. [47], and Hong and Chen [48].

The goal in this thesis is to develop a numerical optimization approach, connecting the newly developed numerical plant model, see section 1.3.2, and a gradient-free optimization method that enables the inclusion of discontinuous design variables, e.g. different insulation materials for the TES.

Chapter 5 presents the newly developed optimization design tool and first simulations.

MULTI-TANK THERMAL-ENERGY STORAGE ¹**2.1 Introduction**

Thermal-energy storage (TES) is a key component of advanced adiabatic compressed air energy storage (AA-CAES) and concentrated solar power (CSP) plants. In CSP plants, TES allows electricity to be generated during periods of low or no insolation and thereby improves the plant economics, see Madaeni et al. [49]. The design of TES systems for CSP plants has received a lot of attention, see, e.g., the overviews of Kuravi et al. [21] and Pelay et al. [22], while by comparison the design of TES systems for AA-CAES plants has received less attention. In AA-CAES plants, the TES is used to extract the heat of compression from the air. By resupplying the thermal energy to the air prior to expansion, AA-CAES plants avoid the need to burn fossil fuels and can reach round-trip efficiencies of 60-75%, see Budt

¹Material in this chapter has been published in P. Roos and A. Haselbacher, “Thermocline control through multi-tank thermal-energy storage systems”, Applied Energy, vol. 281, p. 115971, 2021. doi: 10.1016/j.apenergy.2020.115971

et al. [16] and Sciacovelli et al. [17].

The relative lack of attention on the design of TES systems for AA-CAES plants is unsatisfactory because it can be argued to be more challenging than the design of TES systems for CSP plants. For example, the operation of a CSP plant is largely dictated by local insolation conditions that can be forecast with good accuracy, as described by Schroedter-Homscheidt and Wilbert [50]. The operation of an AA-CAES plant, however, is dictated by the instantaneous state of the electric grid to which it is connected. Therefore, the plant operation is determined not just by local insolation and wind patterns, but it may also be affected by international electricity markets, whose fluctuations in turn are influenced by large-scale insolation and wind patterns, see Wolff and Feuerriegel [51]. Evidence of the irregular operating characteristics of the diabatic CAES plant in Huntorf, Germany was presented by Crotogino et al. [15].

Prior work on TES design for AA-CAES has largely ignored the influence of irregular operating conditions. A notable exception is the work of Sciacovelli et al. [17], who showed that considering irregular operating conditions impacts the efficiency and is therefore crucial for plant designs. The importance of including irregular operating conditions for diabatic CAES plants is demonstrated by the results of Nikolakakis and Fthenakis [52], which indicate that unsteady operation lowers the profitability by 15-30%. It is expected that this conclusion applies to AA-CAES plants, too. Another notable exception is the work of McTigue et al. [53]. They analyzed the impact of perturbed cycle durations on a stand-alone TES, i.e., one that is not embedded in an AA-CAES plant, and found that exergy losses may be increased or decreased depending on the duration of the perturbations.

The overarching goal of our work is to make a contribution to the design of TES systems for AA-CAES plants. The central issues addressed in our work concern not just the unsteady operation of such plants, but also the limited space available to the TES. The latter issue arises because the plant configurations we are investigating place the TES in caverns excavated from hard rock, see our prior work described by Geissbühler et al. [19] and

Becattini et al. [20]. To keep the excavation costs low, the diameter of the caverns should match the diameters attainable by current industrial excavation methods. For example, the diameters of existing tunnel boring machines are typically less than about 18 m [54, 55]. This places a premium on TES designs that minimize the volume required to store a specified amount of thermal energy. Such designs have a large volumetric storage density and a large utilization factor, which is defined as

$$\zeta = \frac{\text{utilized storage capacity}}{\text{maximum storage capacity}}. \quad (2.1)$$

One way of achieving high utilization factors is through the thermocline control (TCC) methods investigated by Geissbühler et al. [32, 33]. Their investigation led to two main conclusions for packed-bed TES with a fixed volume. First, TCC methods can deliver relative increases in the utilization factor of 38.8% and 73.4% at quasi-steady conditions for a stand-alone TES operating with air or molten salt as heat-transfer fluids (HTF), respectively, at the expense of small decreases in the cycle exergy efficiency. Second, when considering a CSP plant operating on a Rankine cycle and molten salt as HTF, the increased utilization factors translate into an increase in the annual average plant efficiency from 14.6% to 16.1% and a relative increase in the annual net electricity generated solely from thermal energy supplied by the TES of 26.0%. TCC methods can also be advantageous when dealing with irregular cycle durations. White et al. [31] worked on the optimization of a segmented packed bed enabling extraction and injection of heat transfer fluid, which reduced the minimum achievable loss by up to 50% and potentially enables a more constant power output for CAES plants. McTigue et al. [53] showed that the sliding-flow TCC method (to use the nomenclature of Geissbühler et al. [32]) can reduce the effect of perturbations in the cycle durations on the exergy losses, especially for short cycle durations.

The TCC concepts investigated by Geissbühler et al. [32, 33] can be viewed as vertically stacked TES units. For large storage capacities, vertical stacking may be problematic for two reasons. First, it leads to tall storages, which should be avoided because of the aforementioned restrictions on the

diameter of the excavated volume. Second, it requires a structural design that can support the considerable weight of the stacked packed beds, which increases the cost of the TES. The two problems can be circumvented if the units are not stacked vertically, but placed next to each other, leading to a so-called multi-tank TES (MTTES).

Considerable work on MTTES has been carried out at low temperatures for water as both storage medium and HTF, see Chen et al. [56] and Dickinson et al. [57, 58]. We refrain from providing a detailed review of this work because its conclusions are not relevant given our focus on packed beds of rocks with air as HTF and higher temperatures.

To the best of our knowledge, high-temperature MTTES has so far been investigated only by Ortega-Fernández et al. [59] and Cárdenas and Garvey [60]. Based on simulations, Ortega-Fernández et al. [59] concluded that splitting a TES into smaller units that are operated in parallel does not provide a significant performance improvement as measured by the outflow temperatures during charging and discharging. However, they did not operate the MTTES in a manner that allowed the thermoclines to be controlled, which explains the absence of significant performance improvements.

Cárdenas and Garvey [60] studied two-tank TES systems that are subjected to a perturbed sinusoidal energy flow during charging and discharging. Using simulations, they designed a two-tank system whose large and small tanks were supplied with the low- and high-frequency energy flows, respectively. They showed that exergy losses of the two-tank system were 25.5% lower than those of the single-tank storage. These results must be interpreted with caution, however, as the heat losses to the surroundings were neglected. Depending on the amount of insulation, this may not be justified as the surface area of the two-tank system was 18.7% larger than that of the single-tank storage.

The purpose of this work is to present a first assessment of MTTES at high temperatures by focusing on nominal operating conditions, by which we mean constant charging and discharging durations and constant inflow temperatures during charging and discharging. The assessment of MTTES

under operating conditions that are more reflective of those to which future AA-CAES will be subjected will be presented in a forthcoming publication. The question we address in this work is whether MTTES can outperform a single-tank TES in terms of the required total volume, efficiency, and material costs. In contrast to the work of Cárdenas and Garvey [60], we do not neglect the heat losses to the ambient.

2.2 Operation of MTTES systems

2.2.1 Basic operating modes

An MTTES system consists of two or more tanks that are connected by pipes and valves. Depending on the valve settings, two basic modes of operating such a system may be defined: parallel or serial. In the following, we first explain how an MTTES system composed of two tanks of equal volume can be operated before considering the operation of systems composed of more than two tanks.

Figure 2.1(a) depicts a two-tank system being charged and discharged in parallel mode. During charging, the mass flow supplied to the system, denoted by \dot{m}_c , is split between the two tanks such that

$$\dot{m}_c = \dot{m}_{c,1} + \dot{m}_{c,2}, \quad (2.2)$$

where $\dot{m}_{c,1} > 0$ and $\dot{m}_{c,2} \geq 0$. The temperature of the HTF flowing into each tank is equal to the inflow temperature of the system,

$$T_{c,\text{in},i} = T_{c,\text{in}}. \quad (2.3)$$

If the mass flow is split equally between the two tanks, the thermoclines in the two tanks will be identical. This, together with the increased thermal losses caused by the larger surface area compared to a single tank of the same total volume, means that MTTES systems operated in parallel with equal mass flows offer no benefits as measured through the key performance indicators listed in section 2.3. Significant benefits can result if the mass flows are allowed to be unequal as well as time-dependent, however.

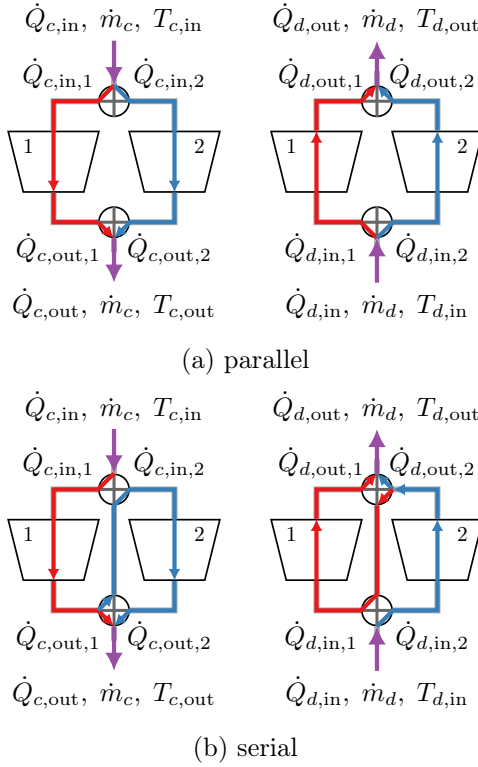


Figure 2.1: Two-tank TES system for (a) parallel and (b) serial operation during charging (left) and discharging (right). The flow paths are indicated by the red and blue arrows. The system inflow and outflow streams are depicted by purple arrows.

Figure 2.1(b) shows a two-tank system being charged and discharged in serial mode. For charging, all of the mass flow supplied to the system flows through the first tank,

$$\dot{m}_{c,1} = \dot{m}_c, \quad (2.4)$$

$$T_{c,in,1} = T_{c,in}, \quad (2.5)$$

and the second tank is fed at least partly by the outflow from the first tank,

$$0 < \dot{m}_{c,2} \leq \dot{m}_{c,1}, \quad (2.6)$$

$$T_{c,\text{in},2} = T_{c,\text{out},1}. \quad (2.7)$$

Charging in serial mode, as for the parallel mode, can result in significant performance benefits only if unequal and time-dependent mass flows are used.

The equations for parallel and serial discharging follow from those for charging by replacing $T_{c,\text{in}}$ with $T_{d,\text{in}}$ and, for the serial mode, by discharging the second tank first.

For MTES systems consisting of $N > 2$ tanks, the parallel and serial modes are analogous to those described above, with the exception that $N - 1$ of the mass flows $\dot{m}_{c,i}$ and $\dot{m}_{d,i}$ may be zero.

The parallel operating mode was investigated by Ortega-Fernández et al. [59] and Cárdenas and Garvey [60]. In this work, we focus on the serial operating mode and how it can be used to implement, in the context of MTES, the TCC methods that were investigated by Geissbühler et al. [32, 33] for a single tank. In the following, we restrict our attention to the extraction and mixing TCC methods, which were shown to result in the highest exergy efficiencies and utilization factors among the methods investigated by Geissbühler et al. [32, 33].

2.2.2 Extraction method

The extraction method is characterized by switching between the tanks in a binary manner using a switching criterion that is based on the allowable maximum outflow temperature. At the beginning of charging, the HTF flows only through the first tank until its outflow temperature reaches the switching criterion,

$$\dot{m}_{c,1} = \dot{m}_c \quad \text{if} \quad T_{c,\text{out},1}(t) \leq T_{c,\text{out},\text{target}}, \quad (2.8)$$

$$\dot{m}_{c,i} = 0 \quad \text{for} \quad 2 \leq i \leq N, \quad (2.9)$$

where $T_{c,\text{out,target}}$ is the target outflow temperature during charging. Once that target temperature is reached, the valves adjust to route the HTF not just through the first but also through the second tank until that tank's outflow temperature reaches the switching criterion,

$$\dot{m}_{c,1} = \dot{m}_{c,2} = \dot{m}_c \quad (2.10)$$

$$\text{if } T_{c,\text{out},2}(t) \leq T_{c,\text{out,target}} < T_{c,\text{out},1}(t),$$

$$\dot{m}_{c,i} = 0 \quad \text{for } 3 \leq i \leq N, \quad (2.11)$$

and then the HTF is directed to the third tank. This procedure is repeated until the HTF flows through the N th tank.

In addition to the switching criterion, for all tanks except the last, we use a stopping criterion to turn off the flow of the HTF when the difference between the outflow and inflow temperatures falls below a specified temperature difference,

$$\dot{m}_{c,i} = 0 \quad \text{for } 1 \leq i < N \quad (2.12)$$

$$\text{if } T_{c,\text{out},i}(t) \geq T_{c,\text{in}} - \Delta T_{c,\text{stop}},$$

where $\Delta T_{c,\text{stop}} < T_{c,\text{in}} - T_{c,\text{out,target}}$. The motivation for the stopping criterion is wanting to avoid the pumping work that is associated with letting the HTF flow through a nearly fully charged tank.

During discharging, the extraction TCC method proceeds analogously, except that the switching criterion is based on $T_{d,\text{out,target}}$ and that at the beginning of discharging, the HTF flows only through the N th tank until the switching criterion is reached,

$$\dot{m}_{d,N} = \dot{m}_d \quad \text{if } T_{d,\text{out},N}(t) \geq T_{d,\text{out,target}}, \quad (2.13)$$

$$\dot{m}_{d,i} = 0 \quad \text{for } 1 \leq i \leq N - 1. \quad (2.14)$$

Once that target temperature is reached, the valves adjust to route the HTF not just through the last but also through the second last tank until that

tank's outflow temperature reaches the switching criterion,

$$\dot{m}_{d,N} = \dot{m}_{d,N-1} = \dot{m}_d \quad (2.15)$$

$$\text{if } T_{d,\text{out},N-1}(t) \geq T_{d,\text{out},\text{target}} > T_{d,\text{out},N}(t),$$

$$\dot{m}_{d,i} = 0 \quad \text{for } 1 \leq i \leq N-2, \quad (2.16)$$

and then the HTF is directed to tank $N-2$. This procedure is repeated until the HTF flows through the first tank. The stopping criterion is defined as

$$\dot{m}_{d,i} = 0 \quad \text{for } 1 < i \leq N$$

$$\text{if } T_{d,\text{out},i}(t) \leq T_{d,\text{in}} + \Delta T_{d,\text{stop}}, \quad (2.17)$$

where $\Delta T_{d,\text{stop}} < T_{d,\text{out},\text{target}} - T_{d,\text{in}}$.

The switching of the HTF is illustrated schematically in fig. 2.2(a) for an MTTES system consisting of four tanks. The solid and dashed lines indicate the flow of the HTF during charging and discharging, respectively, and red, blue, green, and orange lines represent the HTF flowing into, through, and out of tanks one, two, three, and four, respectively.

Exemplary results for the four-tank system during one charge-discharge cycle at the quasi-steady state, obtained using the numerical method described in appendix A, are presented in fig. 2.2(b). The plot at the bottom shows the temporal evolutions during charging of the non-dimensional mass flows through the four tanks and the outflow temperature of the system, defined as

$$\tilde{m}_{c,i}(\tilde{t}) = \frac{\dot{m}_{c,i}(t)}{\dot{m}_c}, \quad (2.18)$$

$$\tilde{T}_{c,\text{out}}(\tilde{t}) = \frac{T_{c,\text{out}}(t) - T_{d,\text{in}}}{T_{c,\text{in}} - T_{d,\text{in}}}, \quad (2.19)$$

where $0 \leq \tilde{t} \leq 1$ is a non-dimensional time defined as $\tilde{t} = t_c / \Delta t_c$. The plot

at the top shows the corresponding temporal evolutions during discharging,

$$\tilde{m}_{d,i}(\tilde{t}) = \frac{\dot{m}_{d,i}(t)}{\dot{m}_d}, \quad (2.20)$$

$$\tilde{T}_{d,\text{out}}(\tilde{t}) = \frac{T_{d,\text{out}}(t) - T_{d,\text{in}}}{T_{c,\text{in}} - T_{d,\text{in}}}, \quad (2.21)$$

where the non-dimensional time is defined as $\tilde{t} = t_d/\Delta t_d$. The results show clearly the step-function behavior of the mass flows resulting from the binary operation of the valves as well as the resulting temperature peaks that are characteristic of the extraction method. The plots in the middle show the non-dimensional thermoclines defined by

$$\tilde{T}(\tilde{x}, \tilde{t}) = \frac{T(x, t) - T_{d,\text{in}}}{T_{c,\text{in}} - T_{d,\text{in}}}, \quad (2.22)$$

where $\tilde{x} = x/H$ with H denoting the height of the tanks, at the four non-dimensional times during charging and discharging that are indicated in the bottom and top plots. The gray backgrounds in fig. 2.2(b) correspond to those in fig. 2.2(a) to connect the exemplary results to the schematic flow paths.

2.2.3 Mixing method

The mixing method results from controlling the flow of the HTF through a pair of tanks such that a fraction of the HTF flowing out of the first tank flows into the second tank and that the temperature of the mixed outflows equals a predefined target value. The target value can be any constant or time-dependent value between the inflow temperatures during charging and discharging. If the target temperature cannot be achieved, a new pair of tanks is formed by dropping one of the two tanks and adding a new second tank. The dropped tank follows the same stopping criterion defined by eqs. (2.12) and (2.17) for charging and discharging, respectively. This process is continued until the last pair of tanks are activated or until the charging or discharging has been completed as shown schematically in fig. 2.3(a).

For each pair of tanks, the fraction of the HTF flowing out of the first tank that is routed into the second tank is easily derived from an energy balance. Denoting the first and second tanks by the indices i and $i + 1$ and assuming that the thermal losses of the pipes and valves connecting the tanks are negligible, we have during charging,

$$\dot{Q}_{c,\text{out}}(t) = (\dot{Q}_{c,\text{out},i}(t) - \dot{Q}_{c,\text{in},i+1}(t)) + \dot{Q}_{c,\text{out},i+1}(t),$$

where

$$\begin{aligned} \dot{Q}_{c,\text{out}} &= \dot{m}_c \int_{T_{\text{ref}}}^{T_{c,\text{out},\text{target}}} c_{p,f}(\xi) d\xi, \\ \dot{Q}_{c,\text{out},i}(t) - \dot{Q}_{c,\text{in},i+1}(t) &= (\dot{m}_c - \dot{m}_{i+1}(t)) \int_{T_{\text{ref}}}^{T_{c,\text{out},i}(t)} c_{p,f}(\xi) d\xi, \\ \dot{Q}_{c,\text{out},i+1}(t) &= \dot{m}_{i+1}(t) \int_{T_{\text{ref}}}^{T_{c,\text{out},i+1}(t)} c_{p,f}(\xi) d\xi, \end{aligned}$$

with $T_{c,\text{out},\text{target}}$ and T_{ref} denoting the desired outflow temperature and an arbitrary reference temperature, respectively. If the specific heat capacity of the HTF is constant, we obtain

$$\frac{\dot{m}_{i+1}(t)}{\dot{m}_c} = \frac{T_{c,\text{out},i}(t) - T_{c,\text{out},\text{target}}}{T_{c,\text{out},i}(t) - T_{c,\text{out},i+1}(t)}. \quad (2.23)$$

An analogous derivation for discharging results in

$$\frac{\dot{m}_i(t)}{\dot{m}_d} = \frac{T_{d,\text{out},\text{target}} - T_{d,\text{out},i+1}(t)}{T_{d,\text{out},i}(t) - T_{d,\text{out},i+1}(t)}. \quad (2.24)$$

Exemplary results for the four-tank system during one charge-discharge cycle at the quasi-steady state, again obtained using the numerical method described in appendix A, are presented in fig. 2.3(b). The structure of the figure follows that of fig. 2.2(b) with the exception of the plots in the middle, which are organized into only three rows because the mixing method operates the four tanks in three pairs. The figure shows clearly how the mass flows are varied to keep the outflow temperatures constant over the entire discharging phase and nearly the entire charging phase.

The deviations from constant outflow temperatures can be explained as follows. At the beginning of the charging phase, the outflow temperature cannot be kept constant because the outflow temperatures of tanks one and two are lower than the target temperature. Conversely, near the end of the charging phase, the outflow temperature again cannot be held constant because the outflow temperature of tank four exceeds the target temperature. (One option for addressing this lack of constancy is mixing with bypass air at charging temperature in the beginning of the charging phase.) This option was not considered in this study to prevent excessive exergy destruction. Note that near the end of discharging, the outflow temperature equals the target temperature, in contrast to charging. This difference is due to the truncated conical tanks.

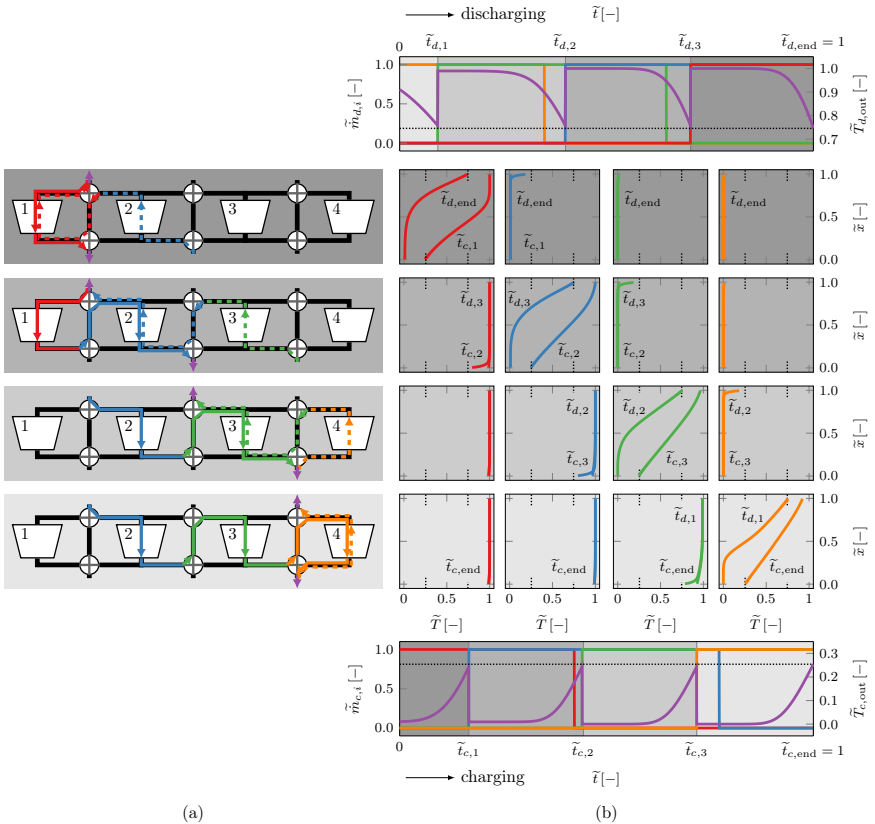


Figure 2.2: Charging and discharging of an MTTES system consisting of four tanks with extraction TCC. In subfigure (a), the charging and discharging paths are indicated by full and dashed lines, respectively, and red, blue, green, and orange lines representing the HTF flowing towards, through, and out of tanks one, two, three, and four, respectively. In subfigure (b), the top and bottom plots show the non-dimensional mass flows (same colors as in subfigure (a)) and the non-dimensional outflow temperatures (purple lines) as a function of non-dimensional time during discharging and charging, respectively. The plots in the middle show the thermoclines in the four tanks at the four times during charging and discharging that are indicated in the top and bottom plots. The dotted lines in subfigure (b) indicate the maximum allowable outflow temperatures.

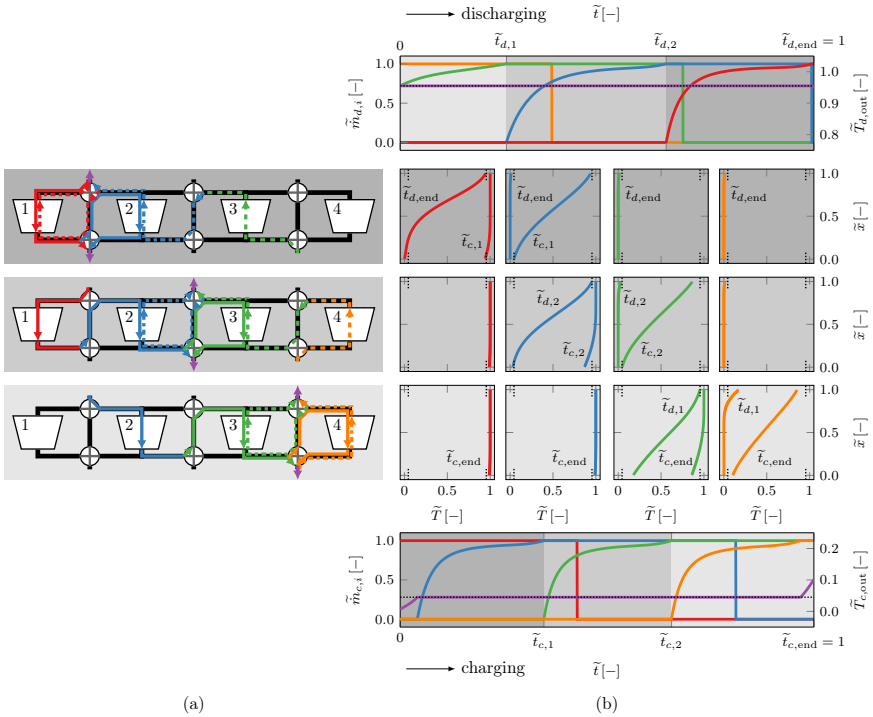


Figure 2.3: Charging and discharging of an MTTES system consisting of four tanks with mixing TCC. In subfigure (a), the charging and discharging paths are indicated by full and dashed lines, respectively, and red, blue, green, and orange lines representing the HTF flowing towards, through, and out of tanks one, two, three, and four, respectively. In subfigure (b), the top and bottom plots show the non-dimensional mass flows (same colors as in subfigure (a)) and the non-dimensional outflow temperatures (purple lines) as a function of non-dimensional time during discharging and charging, respectively. The plots in the middle show the thermoclines in the four tanks at the three times during charging and discharging that are indicated in the top and bottom plots. The dotted lines in subfigure (b) indicate the maximum allowable outflow temperatures.

2.3 Assessment strategy

We assess MTTES systems using four key performance indicators. The first is the non-dimensional outflow temperature change during discharging,

$$\Delta \tilde{T}_{d,\text{out,max}} = \frac{T_{c,\text{in}} - T_{d,\text{out,min}}}{T_{c,\text{in}} - T_{d,\text{in}}} = 1 - \tilde{T}_{d,\text{out}}(1), \quad (2.25)$$

where $\tilde{T}_{d,\text{out}}(1)$ is given by eq. (2.21). In the context of AA-CAES plants, small changes in the outflow temperature during discharging are beneficial because they allow the turbines to be operated near their design points.

The second is the non-dimensional storage volume,

$$\tilde{V} = \frac{V_{\text{total}}}{V_{\text{ideal}}} = \frac{1}{V_{\text{ideal}}} \sum_{i=1}^N V_i \quad (2.26)$$

where V_i is the volume of tank i , N is the number of tanks, and V_{ideal} is an ideal storage volume. An expression for the ideal storage volume can be derived from the following simple argument. Imagine that a TES is charged with a mass flow \dot{m} and temperature $T_{c,\text{in}}$ over a duration Δt and that the outflow temperature should be $T_{d,\text{in}}$. The thermal energy that the TES should capture is therefore

$$E_{\text{capt}} = \dot{m} \Delta t c_{p,f} (T_{c,\text{in}} - T_{d,\text{in}}), \quad (2.27)$$

where $c_{p,f}$ is the specific heat capacity of the HTF. (The same expression results if the TES is discharged with an inflow temperature $T_{d,\text{in}}$ and the outflow temperature should be $T_{c,\text{in}}$.) The maximum thermal energy an ideal packed-bed TES, i.e., one with a perfectly steep thermocline that is located at the bottom/top of the storage at the end of charging/discharging, can store is

$$E_{\text{max,ideal}} = [(1 - \epsilon) \rho_s c_{p,s} + \epsilon \rho_f c_{p,f}] (T_{c,\text{in}} - T_{d,\text{in}}) V_{\text{ideal}}, \quad (2.28)$$

where ϵ is the void fraction of the packed bed, ρ_s is the density of the storage material, ρ_f is the density of the HTF, and $c_{p,s}$ is the specific heat capacity

of the storage material. Equating eqs. (2.27) and (2.28) gives

$$V_{\text{ideal}} = \frac{\dot{m}\Delta t c_{p,f}}{(1-\epsilon)\rho_s c_{p,s} + \epsilon\rho_f c_{p,f}}. \quad (2.29)$$

The non-dimensional storage volume can be related to the utilization factor defined by eq. (2.1) in the following manner. Assuming temperature-independent properties and a cylindrical TES for simplicity, the utilized storage capacity is

$$E_{\text{util}} = [(1-\epsilon)\rho_s c_{p,s} + \epsilon\rho_f c_{p,f}]A \int_0^H (T(x, t_{c,\text{end}}) - T(x, t_{d,\text{end}})) dx,$$

where A is the cross-sectional area of the TES, x is the vertical coordinate, $t_{c,\text{end}}$ and $t_{d,\text{end}}$ are the times at which successive charging and discharging phases end, whereas the maximum storage capacity is

$$E_{\text{max}} = [(1-\epsilon)\rho_s c_{p,s} + \epsilon\rho_f c_{p,f}](T_{c,\text{in}} - T_{d,\text{in}})V,$$

where $V = AH$. Therefore,

$$\tilde{V}\zeta = \frac{E_{\text{max}}}{E_{\text{max,ideal}}} \frac{E_{\text{util}}}{E_{\text{max}}} = \frac{E_{\text{util}}}{E_{\text{max,ideal}}}.$$

In this work, we use the non-dimensional storage volume instead of the utilization factor to simplify the estimation of the storage volume for specific operating conditions. As will be shown in section 2.4, simulations lead to a relation of the form

$$\tilde{V} = \tilde{V}(\Delta\tilde{T}_{d,\text{out,max}}), \quad (2.30)$$

so we can determine \tilde{V} for a desired $\Delta\tilde{T}_{d,\text{out,max}}$, and with V_{ideal} obtained from eq. (2.29), the total storage volume required for the specific operating conditions follow at once from eq. (2.26).

The third key performance indicator is the cycle exergy efficiency, defined following Geissbühler et al. [29] as

$$\eta_{\text{ex}} = \frac{\Xi_{d,\text{net}} - \Xi_{\text{th,pump}}}{\Xi_{c,\text{net}}}, \quad (2.31)$$

where $\Xi_{d,\text{net}}$ is the net exergy recovered by the HTF during discharging, $\Xi_{c,\text{net}}$ is the net exergy supplied by the HTF during charging, and $\Xi_{\text{th,pump}}$ is the thermal exergy required for pumping. The net exergy recovered during discharging is given by

$$\begin{aligned}\Xi_{d,\text{net}} &= \Xi_{d,\text{out}} - \Xi_{d,\text{in}} \\ &= \int_0^{\Delta t_d} \dot{m} \{ h_f(T_{d,\text{out}}) - h_f(T_{d,\text{in}}) \\ &\quad - T_0 [s_f(T_{d,\text{out}}) - s_f(T_{d,\text{in}})] \} dt,\end{aligned}\quad (2.32)$$

where h_f and s_f are the specific enthalpy and specific entropy of the HTF, respectively, and T_0 is taken to be the ambient temperature. The net exergy supplied during charging is defined in the same manner. The specific entropy is taken to depend on the temperature only,

$$s_f(T) = \int_{T_0}^T c_{p,f}(\xi) \frac{d\xi}{\xi}. \quad (2.33)$$

The calculation of $\Xi_{\text{th,pump}}$ is described in Geissbühler et al. [29]. It should be noted that the thermal exergy required for pumping includes only the pressure drops through the packed beds. The pressure drops through the pipes and valves between the TES units are neglected in this first assessment.

The final key performance indicator is the specific material cost,

$$\frac{\text{material costs}}{\text{net energy output per cycle}} = \frac{C_{\text{system}}}{E_{d,\text{net}}}, \quad (2.34)$$

where

$$\begin{aligned}E_{d,\text{net}} &= E_{d,\text{out}} - E_{d,\text{in}} \\ &= \int_0^{\Delta t_d} \dot{m} (h_f(T_{d,\text{out}}) - h_f(T_{d,\text{in}})) dt.\end{aligned}\quad (2.35)$$

2.4 Assessment of MTTES systems

2.4.1 Operating conditions and simulation parameters

The assessment was carried out for operating conditions that were extracted from simulations of the nominal cycling of a prospective 100 MW_{el}/500 MWh_{el} AA-CAES plant. By “nominal cycling”, we mean constant charging and discharging durations of 5 h and constant mass flows during charging and discharging of 200 kg/s. (As mentioned in the introduction, the assessment of MTTES systems under more realistic operating conditions will be covered in a forthcoming publication.)

The prospective plant is based on two-stage compression and expansion trains, which allows the compression and expansion ratios of each train to be limited to a maximum of 10, and contains two caverns. The pressure in the first cavern, located after/before the low-pressure compressor/turbine, remains at 10 bars. The pressure in the second cavern, located after/before the high-pressure compressor/turbine, varies between 70 and 100 bars. MTTES systems are placed in each cavern to cool/heat the compressed air before it flows into/out of the caverns, see Geissbühler et al. [19]. The simulations presented below were performed for MTTES systems located in the low-pressure cavern because this accentuates the importance of pressure losses in the packed beds.

In the simulations, we considered MTTES systems with up to four tanks of equal volume, dimensioned such that the total storage volume is equal to that of the single tank, which means that the surface area grows as the number of tanks increases. To quantify the impact of thermal losses through the growing surface areas, both adiabatic and diabatic conditions were simulated. For the diabatic conditions, the durations of the idle phases were chosen such that a complete charge-idle-discharge-idle cycle takes 24 h. The operating conditions are summarized in table 4.1.

Following earlier work by Zanganeh et al. [61], Becattini et al. [62], and Geissbühler et al. [19], we considered tanks containing packed beds of fluvial

Table 2.1: Operating conditions used in assessment of MTTES systems.

Quantity	Symbol(s)	Value
Mass flow rate	\dot{m}_c, \dot{m}_d	200 kg/s
Charging temperature	$T_{c,in}$	320 °C
Discharging temperature	$T_{d,in}$	20 °C
Ambient temperature	T_{amb}	20 °C
Stopping criterion	$\Delta T_{c,stop}, \Delta T_{d,stop}$	3 °C
Charging/discharging durations	$\Delta t_c, \Delta t_d$	5 h
Idling durations	Δt_{idle}	7 h
System pressure	p	10 bar

rocks on account of their low cost and suitability at high temperatures. The diameters of the rocks were 3 cm in all simulations. The tanks are shaped like truncated cones following Zanganeh et al. [61]. This shape was shown in the simulations of Iliev et al. [63] to reduce the forces that a packed bed of irregular polyhedral particles exerts on the tank wall when subjected to heating and cooling cycles, which implies that the rocks are less likely to fragment and thereby lead to non-uniform heat transfer and higher pressure drops. For simplicity, with reference to fig. 2.4, the geometry of the tanks was considered to have a fixed aspect ratio defined by $r/R = 0.77$ and $H/R = 0.94$ (rounded to two decimals).

Figure 2.4 also shows the arrangement of the construction and insulation layers, which was chosen to be similar to those used by Zanganeh et al. [61] and Geissbühler et al. [29]. The materials used in each layer and the corresponding thicknesses are given in table 2.2. For simplicity, the thicknesses are taken to be constants for all MTTES systems, irrespective of the number of tanks and their volume. The thicknesses of the insulation layers were chosen to result in an exergy efficiency of 98% for a single-tank TES with $R = 16.0$ m, $r = 12.26$ m, and $H = 15.0$ m. The thermophysical properties and volumetric costs of the materials are listed in table 2.3. It should be noted that the specific heats and thermal conductivities of some

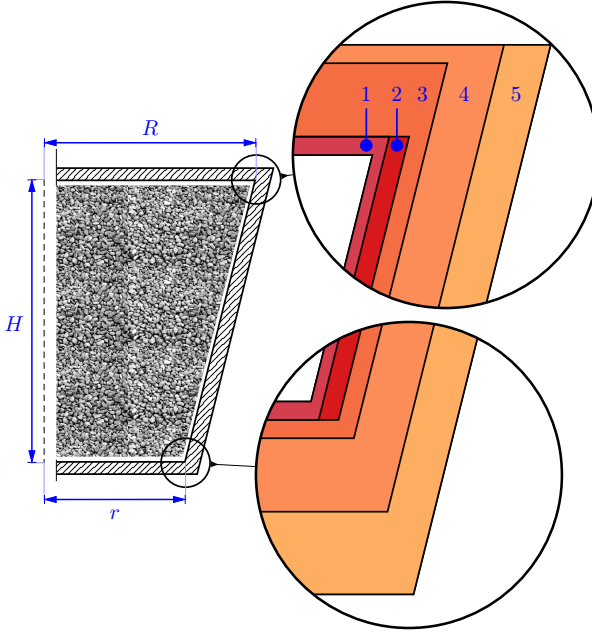


Figure 2.4: Schematic depiction of the tank geometry and the construction and insulation material layers. The materials and thicknesses of the layers are given in table 2.2.

of the materials were considered to be temperature-dependent.

The simulations were carried out with the previously verified and validated code of Geissbühler et al. [29, 19] and Becattini et al. [20], modified to handle MTTES systems as described in appendix A. The modifications include an iterative procedure for the extraction and mixing methods, which finds the smallest achievable $\Delta\tilde{T}_{d,\text{out},\text{max}}$ for a given non-dimensional volume by adjusting $T_{d,\text{out},\text{target}}$ based on the outflow temperature at the end of a discharging phase at the quasi-steady state. The curves given by eq. (2.30) that will be presented below can therefore be interpreted as Pareto fronts. To achieve faster convergence of the iterative procedure, constant air prop-

Table 2.2: Thicknesses of construction and insulation layers shown in fig. 2.4. Note: UHPC and LDC stand for ultra-high-performance and low-density concrete, respectively.

Index	Material	Cover	Wall	Bottom
1	UHPC	0.10 m	0.05 m	0.10 m
2	LDC	–	0.10 m	–
3	Microtherm [®]	0.40 m	0.10 m	0.10 m
4	Foamglass [®]	0.10 m	0.30 m	0.40 m
5	Reinforced concrete	–	0.25 m	0.45 m

erties were used in all simulations. These properties were determined for a system pressure of 10 bars and an average system temperature of 170 °C, resulting in the air properties shown in table 2.3 and a dynamic viscosity of air of $2.46 \cdot 10^{-5}$ Pa s [65]. The heat-transfer coefficient was corrected for intra-particle conduction using the method of Bradshaw et al. [66].

2.4.2 Adiabatic conditions

In fig. 2.5, we compare the extraction and mixing methods for up to four tanks with the single tank in terms of $\Delta\tilde{T}_{d,\text{out,max}}$ and \tilde{V} defined by eqs. (2.25) and (2.26), respectively. An ideal storage would be characterized by $\Delta\tilde{T}_{d,\text{out,max}} = 0$ and $\tilde{V} = 1$. The single tank is seen to be far from ideal and to exhibit the expected trend: Small temperature drops require large volumes and small volumes result in large temperature drops.

The performance of the extraction method shows clear improvements over the single tank: For a given temperature drop, smaller volumes can be used and for a given volume, smaller temperature drops are attained. The improvements are more pronounced for smaller temperature drops and diminish with an increasing number of tanks. The performance of the mixing method exhibits the same overall trends, but exceeds that of the extraction method.

Table 2.3: Thermophysical properties and costs of materials. Whenever a range of a property is given without further indication, the values are temperature-dependent as described by Zanganeh et al. [61] with the exception of *, where the temperature-dependent properties were taken from manufacturer data [64].

Material	c [J/kgK]	ρ [kg/m ³]	k [W/mK]	Costs [\$/m ³]
Air	1022.7	8.19	0.037	0
Rocks	758.5 – 928.7	2635	3.64 – 2.10	66
UHPC	500	2500	1.85 – 2.20	3421
LDC	663	1500	0.37 – 0.52	737
Microtherm [®]	1020	250	0.025 – 0.028*	4269
Foamglass [®]	840	120	0.05	616
Reinforced concrete	784	2400	0.765	188

For the extraction method, four two-tank systems are seen to form a kink, as highlighted by the gray disk. The kink is caused by these systems being too large for the extraction method to perform as intended, for the chosen operating conditions, during discharging. Systems that are too large can be seen to offer only marginally better performance than single tanks. This becomes clearer from fig. 2.6, which presents the thermoclines at the end of charging and discharging and the outflow temperatures during discharging for the four two-tank systems contained in the gray disk. (In this and subsequent similar figures, \tilde{x} is the ratio of the axial coordinate and the height of all tanks in a system.) For the largest system, the maximum temperature at the end of charging in the second tank (and therefore its initial outflow temperature during discharging) is below the target outflow temperature. As a result, the extraction method cannot be used during discharging and the system operates like the single-tank TES during discharging. This becomes even clearer when looking at the outflow temperatures $\tilde{T}_{d,\text{out}}$ and $\tilde{T}_{d,\text{out},2}$ presented in fig. 2.6. The step increases, which indicate the instant when

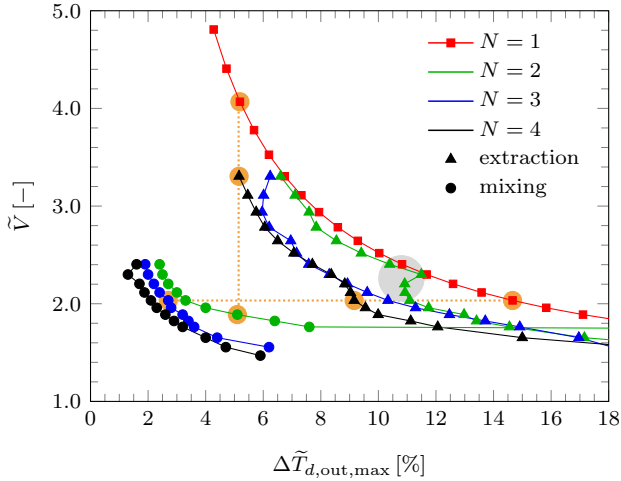


Figure 2.5: Non-dimensional storage volume as a function of $\Delta\tilde{T}_{d,out,max}$ and N for adiabatic conditions. The behaviors of the multi-tank systems highlighted by the gray and orange disks are discussed in the text and shown in figs. 2.6 to 2.8, respectively.

the outflow of the second tank is directed to the inlet of the first tank, are only present for the three smaller systems.

Kinks similar to those for the two-tank system with the extraction method are also visible for three- and four-tank systems. The kinks could be remedied by changing the operating conditions or considering tanks with different volumes and aspect ratios. Considering MTTES systems with tanks of different volumes and aspect ratios is beyond the scope of this work as the large number of variables that characterize such systems requires an efficient optimization approach such as that used by Marti et al. [45].

The performance improvements associated with MTTES systems apparent in fig. 2.5 can be quantified by comparing either the outflow-temperature drop for a given volume or vice versa. An example of the former comparison can be given by the systems characterized by $\tilde{V} = 2.0$ (highlighted by or-

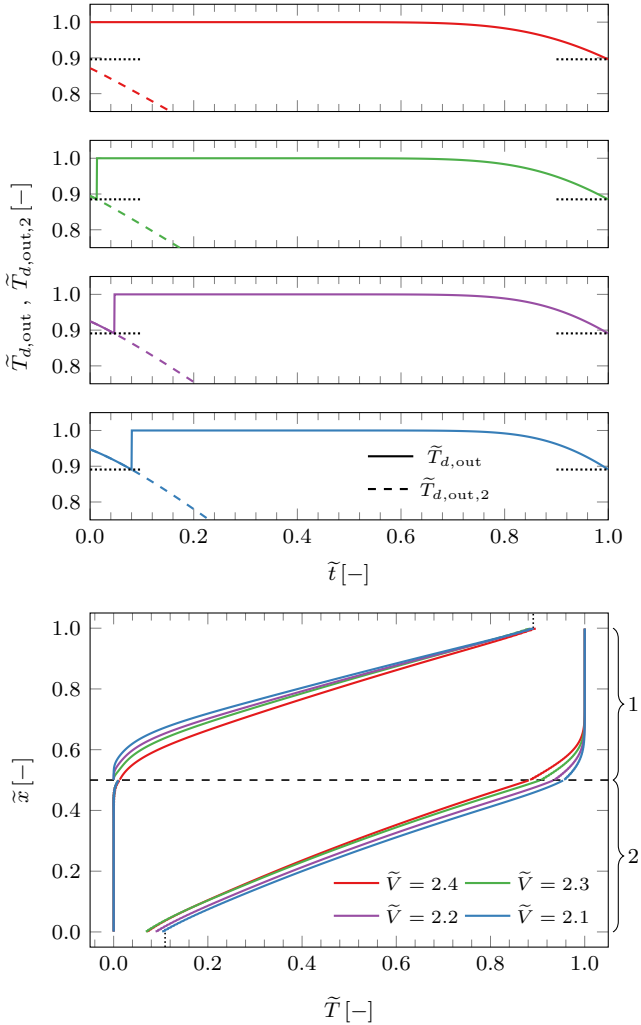


Figure 2.6: Thermoclines at the ends of charging and discharging (bottom plot) and outflow temperatures during discharging (top four plots) for the four two-tank systems with the extraction method highlighted by the gray disk in fig. 2.5. The dashed line and the parentheses indicate the division into two tanks.

ange disks and connected by the horizontal dashed line), for which fig. 2.7 presents the thermoclines and the outflow temperatures during discharging and table 2.4 lists important characteristics and selected key performance indicators. The line colors in fig. 2.7 match those of the highlighted systems fig. 2.5. The thermocline degradation is seen to be highest for the single tank, consistent with the larger values of the outflow-temperature drop. The different behaviors of the outflow temperatures reflect the different operating modes and are similar to the behaviors shown in figs. 2.2(b) and 2.3(b). The three-tank system with mixing achieves the lowest temperature drop, the steepest thermocline, and a constant outflow temperature over the entire discharging phase. The utilization factor of all three systems does not vary much as shown in table 2.4.

Conversely, a comparison of systems characterized by $5.1\% \leq \Delta\tilde{T}_{d,\text{out,max}} \leq 5.2\%$, (highlighted by the orange disks and the vertical dashed line) is presented in fig. 2.8 in terms of the thermoclines and the outflow temperatures during discharging and table 2.5 compiles important characteristics and selected key performance parameters. The line colors in fig. 2.8 match those of the highlighted systems fig. 2.5. The thermocline degradation of the single tank is again seen to be strongest, but now the four-tank system with extraction does not seem to fare significantly better. The two-tank system with mixing is seen to achieve the highest utilization factor and the steepest thermocline.

Table 2.4: Summary of selected characteristics and key performance indicators for the systems with equal \tilde{V} highlighted by orange disks in fig. 2.5.

System	N	V_{total} [m ³]	$\Delta\tilde{T}_{d,\text{out,max}}$ [%]	ζ [%]	$\frac{S_{\text{total}}}{S_{\text{total},1}}$ [-]	$\frac{S_{\text{total}}}{V_{\text{total}}}$ [m ⁻¹]
Single-tank	1	4132.1	14.66	59.7	1.00	0.37
Extraction	4	4132.1	9.16	59.8	1.59	0.59
Mixing	3	4132.1	2.70	59.2	1.44	0.53

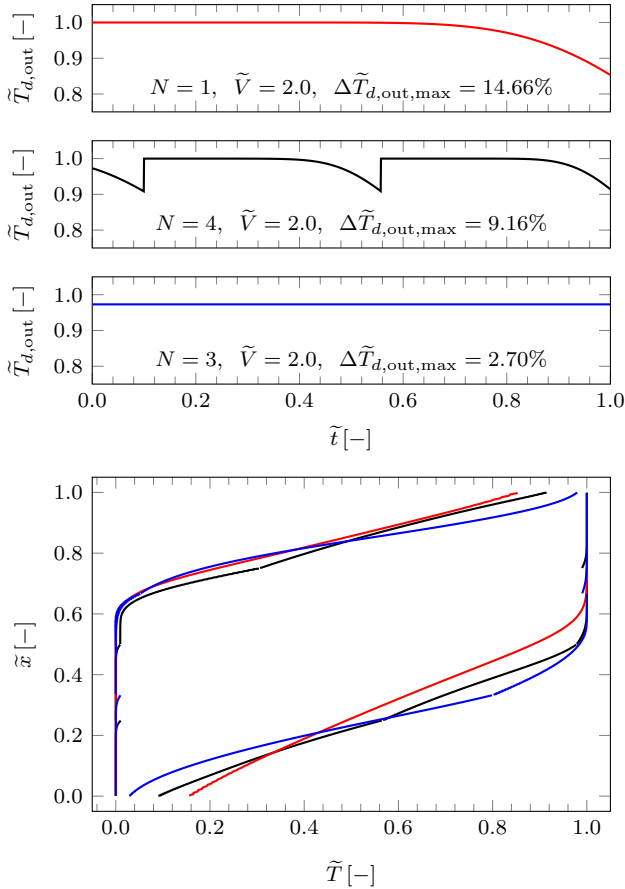


Figure 2.7: Thermoclines at the ends of charging and discharging (bottom plot) and outflow temperatures during discharging (top three plots) for the systems with equal \tilde{V} highlighted by the orange disks in fig. 2.5. The line colors match those in fig. 2.5. The breaks in the thermoclines indicate the division into tanks.

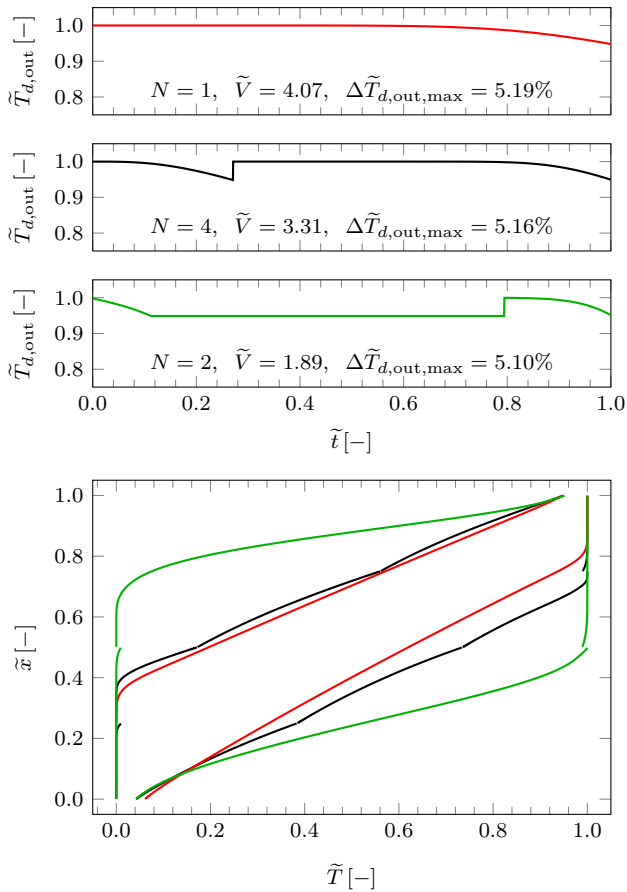


Figure 2.8: Thermoclines at the ends of charging and discharging (bottom plot) and outflow temperatures during discharging (top three plots) for the systems with similar $\Delta\tilde{T}_{d,out,max}$ highlighted by the orange disks in fig. 2.5. The line colors match those in fig. 2.5. The breaks in the thermoclines indicate the division into tanks.

In summary, under adiabatic conditions, MTTES systems operated with the extraction or mixing methods offer significantly improved performance. For a given outflow-temperature drop, the total storage volume can be decreased or for a given total storage volume, a much lower outflow-temperature drop can be achieved. The mixing method is found to outperform the extraction method.

Table 2.5: Summary of characteristics and selected key performance indicators for the systems with nearly equal $\Delta\tilde{T}_{d,\text{out,max}}$ highlighted by the orange disks in fig. 2.5.

System	N	V_{total} [m ³]	$\Delta\tilde{T}_{d,\text{out,max}}$ [%]	ζ [%]	$\frac{S_{\text{total}}}{S_{\text{total},1}}$ [-]	$\frac{S_{\text{total}}}{V_{\text{total}}}$ [m ⁻¹]
Single-tank	1	8264.1	5.19	30.3	1.00	0.29
Extraction	4	6714.6	5.16	37.1	1.38	0.50
Mixing	2	3836.9	5.10	62.9	0.76	0.48

Compared to single tanks, multi-tank systems suffer from increased surface-area-to-volume ratios $S_{\text{total}}/V_{\text{total}}$, as indicated by tables 2.4 and 2.5. This may raise concerns about the performance of multi-tank systems under diabatic conditions. However, table 2.5 also indicates that when multi-tank systems are compared to a single tank for the same drop in the outflow temperature, then $S_{\text{total}}/S_{\text{total},1}$, the ratio of the surface area of the multi-tank system to the surface area of the single tank, may actually decrease because of the multi-tank system's substantially reduced total volume. Thus, the performance of multi-tank systems relative to a single tank under diabatic conditions merits further investigation.

2.4.3 Diabatic conditions

Because the mixing method outperformed the extraction method under adiabatic conditions, the remainder of the assessment will focus on the performance of the mixing method relative to that of a single tank.

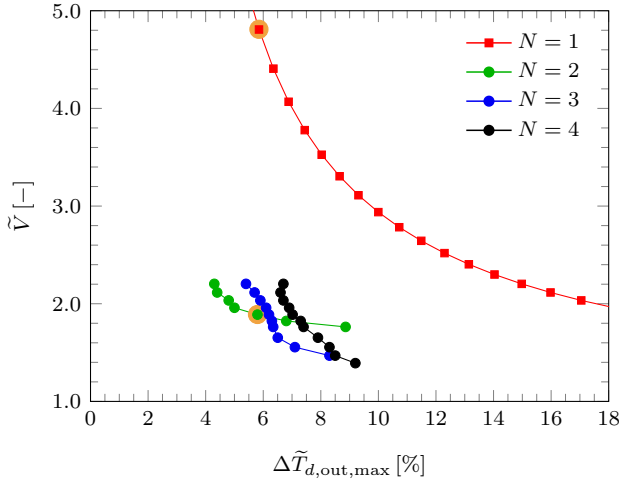


Figure 2.9: Non-dimensional storage volume as a function of $\Delta\tilde{T}_{d,out,max}$ and N for diabatic conditions and the mixing method ($N > 1$). For the systems highlighted by the orange disks, additional information is provided in table 2.7 and the thermoclines and outflow temperatures during discharging are shown in fig. 2.12.

Figure 2.9 shows that even under diabatic conditions, the mixing method allows for much smaller volumes for a given drop in the outflow temperature during discharging. Compared to the results for adiabatic conditions presented in fig. 2.5, two observations can be made. First, the curves for the mixing method are shifted toward the right, indicating that larger drops in the outflow temperature must be accepted for the same volume. This trend is expected because thermal losses reduce the thermal energy that is extracted during discharging. Second, the rightward shifts increase with the number of tanks, which is also expected because the constant total volume means that the surface area and therefore the thermal losses increase with the number of tanks. As a result, whereas the four-tank system led to the smallest temperature drops of 1.3% under adiabatic conditions, under dia-

batic conditions the smallest temperature drops of about 4.3% are achieved by the two-tank system.

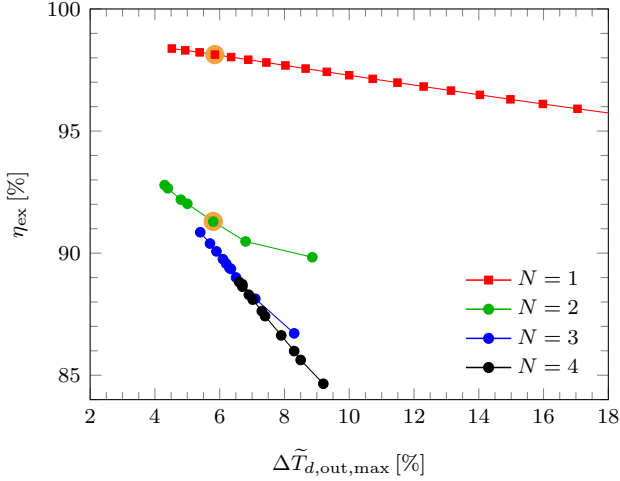


Figure 2.10: Exergy efficiency determined from eq. (2.31) as a function of $\Delta\tilde{T}_{d,\text{out,max}}$ and N for diabatic conditions and the mixing method ($N > 1$). For the systems highlighted by the orange disks, a breakdown of the exergy losses is presented in table 2.6.

Figure 2.10 indicates that the mixing method leads to lower exergy efficiencies than the single tank. This is not just due to the inherent losses associated with mixing and the thermal losses, but also due to the increased internal heat transfer caused by the steeper thermoclines, as can be seen from the exergy loss breakdown presented in table 2.6. It should be noted that the exergy efficiencies plotted in fig. 2.10 are lower than those reported by Geissbühler et al. [33] in their assessment of the mixing method for TCC of single tanks. One explanation for this difference is that Geissbühler et al. [33] neglected thermal losses from the ports used to implement TCC, whereas the thermal losses associated with the additional top and bottom surfaces caused by dividing a single into multiple tanks are included in our

Table 2.6: Exergy loss breakdown for the systems highlighted by the orange disks in fig. 2.9.

N	Mixing [%]	Internal HT [%]	Thermal losses [%]	Pumping work [%]
1	0.00	0.71	1.06	0.10
2	3.17	2.61	2.30	0.64

assessment.

Figure 2.10 also shows that the exergy efficiencies of the multi-tank systems decrease rapidly for systems with larger drops in the outflow temperature. Considered by itself, this trend suggests that the mixing method should only be used for applications in which small drops of the outflow temperature are essential. While high exergy efficiencies should always be a goal of TES design, it must be kept in mind that the ultimate objective of any storage must be to enhance the system into which the storage is integrated. In other words, lower performance and higher costs of a TES can be acceptable if they are offset by increased performance and/or reduced costs of the system. An instructive example of such an offset was presented by Geissbühler et al. [33], in which a thermocline TES with mixing TCC and molten salt as HTF was shown, despite the lower exergy efficiency relative to a storage without TCC, to increase both the annually averaged efficiency of a CSP plant from 14.6% to 16.1% as well as the annual net electricity generated solely from thermal energy extracted from the TES by 26.0%. Whether AA-CAES plants will benefit from MTTES is the subject of a forthcoming publication, in which we will also investigate the optimization of the tank geometry and the insulation thicknesses.

The specific material costs are presented in fig. 2.11. For temperature drops lower than about 8%, the two-tank system exhibits the lowest costs, whereas for drops larger 8% and lower than about 12.5%, the three-tank system is the least costly. Figure 2.11 must be interpreted with caution

because, as already mentioned, valves and piping are not yet included in the material costs.

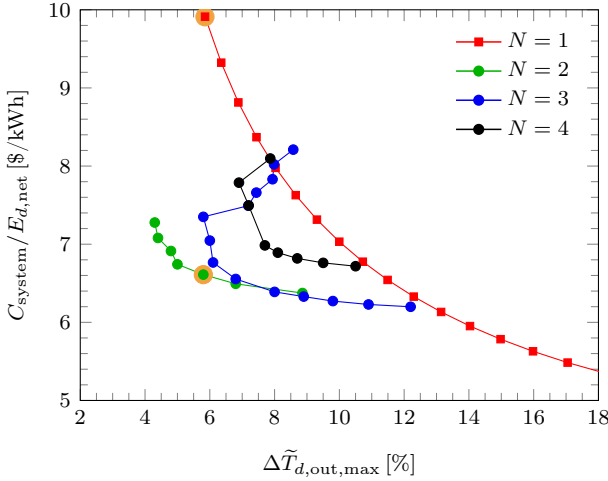


Figure 2.11: Specific material costs as a function of $\Delta\tilde{T}_{d,\text{out,max}}$ and N for diabatic conditions and the mixing method ($N > 1$).

The impact of the mixing method can be demonstrated by comparing the two-tank system and the single tank that are indicated by orange disks in figs. 2.9 to 2.11. They were selected to have nearly identical values of $\Delta\tilde{T}_{d,\text{out,max}}$ of 5.85% and 5.80%, respectively. The thermoclines and outflow temperatures are presented in fig. 2.12 whereas characteristics and selected key performance indicators are given by table 2.7. The two-tank system with mixing has a volume that is about 2.5 times smaller than that of the single tank, a utilization factor that is about 2.4 times larger, an exergy efficiency that is 6.8% lower, and specific material costs that are about 1.5 times lower.

In summary, for diabatic conditions and a given outflow-temperature drop, MTTES systems using the mixing method can attain reduced volumes and material costs compared to a single tank. These improvements are

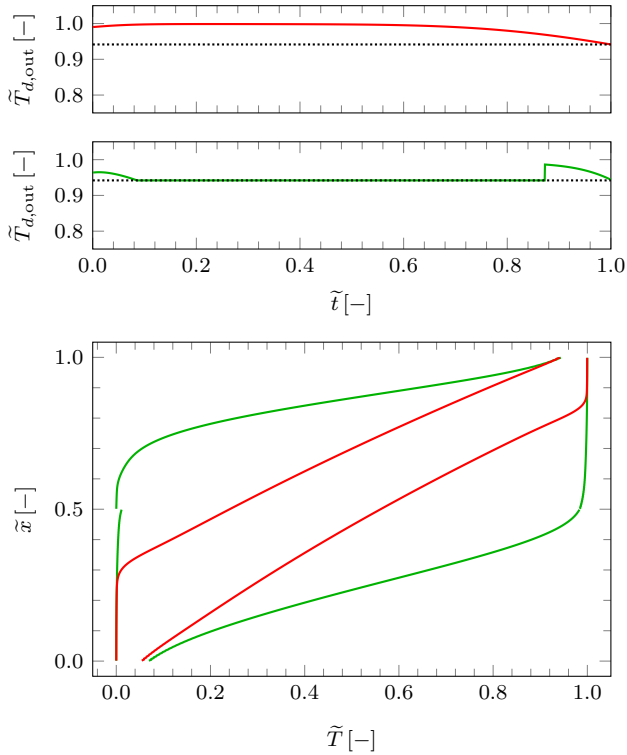


Figure 2.12: Thermoclines at the ends of charging and discharging (bottom plot) and outflow temperatures during discharging (top two plots) for the systems highlighted by the orange disks in fig. 2.9. The line colors match those in fig. 2.9. The breaks in the green lines indicate the division into two tanks.

Table 2.7: Summary of characteristics and selected key performance indicators for the systems highlighted by the orange disks in fig. 2.9.

N	V_{total} [m ³]	$\Delta\tilde{T}_{d,\text{out,max}}$ [%]	ζ [%]	η_{ex} [%]	$\frac{C_{\text{system}}}{E_{d,\text{net}}}$ [\$/kWh]	$\frac{S_{\text{total}}}{S_{\text{total},1}}$ [-]	$\frac{S_{\text{total}}}{V_{\text{total}}}$ [1/m]
1	9766.7	5.85	25.4	98.1	9.91	1.00	0.28
2	3836.9	5.80	61.6	91.3	6.61	0.68	0.48

achieved at the expense of lower exergy efficiencies. The increased thermal losses and insulation material costs caused by higher surface-to-volume ratios means that there is no benefit to considering more than three tanks for the conditions used in this study.

2.5 Summary, conclusions, and future work

MTTES systems were presented as a method to implement TCC, allowing the drop in the outflow temperature during discharging to be controlled and the volumetric storage density and utilization factor to be increased. Such systems can be of interest if they allow a downstream turbine to operate closer to its design point and if the space available to the TES system is limited, as in AA-CAES plants with hard-rock caverns.

MTTES systems based on the extraction and mixing TCC methods were assessed through simulations and comparisons with single tanks. The assessment assumed fluvial rocks as storage material and compressed air at 10 bar as the HTF and considered up to four tanks of equal volume and fixed aspect ratio. We introduced the storage volume relative to an ideal storage volume as a performance indicator. The ideal storage volume is the volume that would be required to store a given amount of thermal energy assuming infinitely steep thermoclines and constant outflow temperatures equal to the respective inflow temperatures.

The assessment of MTTES systems under adiabatic conditions showed

that the extraction and mixing methods can deliver lower drops in the outflow temperature during discharging for the same volume or require smaller volumes for the same drop in the outflow temperature. These improvements diminished as the number of tanks increased. The mixing method performed significantly better than the extraction method. With three tanks, the mixing method resulted in an outflow temperature drop of 2.70%, which is 5.4 times smaller than that of the single tank for the same total volume. Conversely, to reach a temperature drop of 5.10%, the mixing method with two tanks required a volume that was 2.15 times smaller than that of the single tank.

For diabatic conditions, the mixing method also showed better performance than the single tank, but increasing the number of tanks beyond three was not beneficial. With two tanks, the mixing method attained a temperature drop of 5.8% with a volume that is 2.5 times smaller than that of the single tank. For this temperature drop, the exergy efficiency of the two-tank system was 91.3% compared to 98.1% of the single-tank system and the specific material costs of the two-tank system were 1.5 times lower than those of the single-tank system.

The overarching conclusions drawn from the assessment are that MTTES systems can offer significant benefits, and that more extensive assessments are required. These assessments must consider MTTES systems integrated into AA-CAES plants, for example, to determine how the performance and cost of such plants is impacted by the decreased exergy efficiencies, the reduced volumes required to store a given amount of thermal energy, and the reduced specific material costs. For AA-CAES plants with hard-rock caverns, the reduced volumes may be particularly beneficial since they lead to reduced excavation costs. Also beneficial may be the mixing method's ability to provide time-dependent outflow temperatures during discharging, which may simplify attaining constant plant output power, especially for more realistic operating conditions involving unequal charging and discharging durations.

In future assessments, we plan to include valve and piping costs, to consider MTTES systems composed of tanks with unequal volumes and

aspect ratios, and to optimize the performance and cost of the systems with respect to tank geometry and insulation-layer thicknesses.

**ANALYTICAL MODELING OF ADVANCED
ADIABATIC COMPRESSED AIR ENERGY
STORAGE PLANTS ¹**

3.1 Introduction

Compressed air energy storage (CAES), see Budt et al. [16], is regarded as a promising technology for the bulk storage of electrical energy. The operating principle of CAES is simple: When the supply of electrical energy exceeds the demand, the excess powers a motor that drives a compressor ingesting ambient air and the compressed air is stored. When the demand for electrical energy outstrips the supply, the compressed air is released and expanded in a turbine that drives a generator.

So-called diabatic CAES (D-CAES) has proven itself at the utility scale

¹Material in this chapter is taken from P. Roos and A. Haselbacher, “Analytical modeling of advanced adiabatic compressed air energy storage plants”, to be submitted for publication, 2021.

through the plants at Huntorf (Germany, 321 MW_{el}, since 1978) and McIntosh (USA, 100 MW_{el}, since 1991), in which the compressed air is stored in caverns leached from salt deposits, see Crotogino and Quast [67] and Daly et al. [68]. In D-CAES plants, the thermal energy generated by the compression of the air is rejected to reduce the temperature of the air flowing into the cavern. The air flowing out of the cavern must therefore be heated to prevent ice buildup in the turbine. In the Huntorf and McIntosh plants, heat is supplied by combusting fossil fuels, which not only leads to relatively low cycle efficiencies of 45-50%, but also results in greenhouse-gas emissions.

In advanced adiabatic CAES (AA-CAES), the thermal energy generated by the compression of the air is not rejected, but captured in a thermal-energy storage (TES) before entering the cavern. On exiting the cavern, the air is heated in the TES before being expanded in the turbine, thereby obviating the need for combusting fossil fuels. AA-CAES plants are therefore not only free of emissions, but also projected to achieve cycle efficiencies of 65-75%.

At present, AA-CAES plants exist only at the pilot scale. Wang et al. [36] presented results from an above-ground pilot plant that used steel tanks with a volume of 100 m³ to store the air and pressurized water tanks acted as the TES. Average cycle efficiencies of 22.6% were reported. Geissbühler et al. [19] and Becattini et al. [20] presented results obtained with an underground pilot plant in Switzerland containing a hard-rock cavern of about 1942 m³. A combined sensible/latent TES was used at temperatures of up to about 550 °C. Cycle efficiencies, determined from measured and estimated data, were given as 63-74%.

Because of the absence of utility-scale AA-CAES plants, projections of their performance are by necessity based on models. Most of the models reported in the literature are numerical, i.e., they numerically integrate in time equations governing the behaviors of compressors, TES units, caverns, and turbines and provide numerical values of key performance indicators such as the cycle efficiency. Recent examples of such models can be found in Hartmann et al. [34], Barbour et al. [35], Sciacovelli et al. [17], and Tola et al.

[18]. The main advantage of these models is the ease with which they can be extended to include complexities such as real-gas effects, variable turbomachinery efficiencies, and temperature-dependent thermophysical properties. The main disadvantage is that they are not conducive to generating physical insight, i.e., they do not directly indicate which parameters have the largest influence on key performance indicators such as the plant efficiency and the volumetric energy density or what the limiting values of these indicators are.

An alternative to numerical models are analytical models. Such models analytically integrate in time equations governing the behaviors of compressors, TES units, caverns, and turbines, and thereby produce analytical expressions for key performance indicators. The main advantage of analytical models is that these analytical expressions can be manipulated to determine sensitivities and limiting values, thereby generating physical insight. Conversely, their main disadvantage is that including complexities such as those mentioned above can render the governing equations intractable and thereby prevent their analytical integration. It follows that analytical and numerical models are not competing with but complementing each other. These observations have prompted us to revisit analytical models of AA-CAES plants.

A literature search has found only a few relevant publications. The first analytical model of an AA-CAES plant appears to be due to Glendenning [39]. The plant consists of a single compressor, a single turbine, a cavern, and a TES. The model ignores the filling and emptying of the cavern, implying that the compressor and turbine operate at a constant pressure ratio. The TES, which is charged at the constant compressor outflow temperature, is assumed to deliver that same temperature to the turbine during discharging. The model predicts the plant efficiency, defined as the ratio of the work done by the turbine to the work consumed by the compressor, to be

$$\eta = \eta_{s,t} \left[1 - (1 - \eta_{s,c}) \left(\frac{p_{\text{atm}}}{p_{\text{cav}}} \right)^{\frac{\gamma-1}{\gamma}} \right], \quad (3.1)$$

where $\eta_{s,t}$ and $\eta_{s,c}$ are the isentropic efficiencies of the turbine and compressor, respectively; $p_{\text{cav}}/p_{\text{atm}}$ is the constant ratio of the cavern pressure to

the atmospheric pressure; and γ is the ratio of the specific heats. Treating $p_{\text{cav}}/p_{\text{atm}}$ as a constant introduces an ambiguity that Glendenning resolved in an ad-hoc manner by setting p_{cav} to the mean cavern pressure. The model of Glendenning [39] provides two insights. First, the plant efficiency increases as $p_{\text{cav}}/p_{\text{atm}}$ increases: Assuming that $\eta_{s,c} = \eta_{s,t} = 0.85$, we obtain $\eta = 0.796$ for $p_{\text{cav}}/p_{\text{atm}} = 20$ and $\eta = 0.816$ for $p_{\text{cav}}/p_{\text{atm}} = 100$. Second, the plant efficiency is more sensitive to changes in the turbine efficiency. The explanation is that losses in the compressor, which increase the turbine inflow temperature, can be partially converted into work by the turbine.

An extension of the model of Glendenning [39] to a plant with two-stage compression and expansion and with a TES between the low- and high-pressure stages was given by Glendenning et al. [69, p. 2-8]. The extended model also ignores the filling and emptying of the cavern. The plant efficiency can be written as

$$\eta = \frac{\frac{T_{\text{atm}}}{T_3} \left(\frac{p_{\text{int}}}{p_{\text{atm}}}\right)^{\frac{\gamma-1}{\gamma\eta_{p,c}}} \left[1 - \left(\frac{p_{\text{atm}}}{p_{\text{int}}}\right)^{\frac{\gamma-1}{\gamma}\eta_{p,t}}\right] + \left(\frac{p_{\text{cav}}}{p_{\text{int}}}\right)^{\frac{\gamma-1}{\gamma\eta_{p,c}}} \left[1 - \left(\frac{p_{\text{int}}}{p_{\text{cav}}}\right)^{\frac{\gamma-1}{\gamma}\eta_{p,t}}\right]}{\frac{T_{\text{atm}}}{T_3} \left[\left(\frac{p_{\text{int}}}{p_{\text{atm}}}\right)^{\frac{\gamma-1}{\gamma\eta_{p,c}}} - 1\right] + \left[\left(\frac{p_{\text{cav}}}{p_{\text{int}}}\right)^{\frac{\gamma-1}{\gamma\eta_{p,c}}} - 1\right]} \quad (3.2)$$

where T_{atm}/T_3 is the ratio of the ambient temperature to the temperature of the air flowing into the high-pressure compressor; p_{int} , p_{cav} , and p_{atm} are the constant intermediate pressure, cavern pressure, and atmospheric pressure, respectively; and $\eta_{p,c}$ and $\eta_{p,t}$ are the polytropic efficiencies of the compressors and turbines, respectively. The key insight of the model of Glendenning [39] is that for a given $p_{\text{cav}}/p_{\text{atm}}$, the plant efficiency is maximized when either $p_{\text{int}}/p_{\text{atm}} = 1$ or $p_{\text{cav}}/p_{\text{int}} = 1$.

Frutschi [40] presented what amounts to an extension of the model of Glendenning [39] by including a simple measure of the TES efficiency. Thermal losses from the TES are taken to decrease the turbine inflow temperature below the compressor outflow temperature. As a result, the

plant efficiency decreases also, but the insights gleaned from Glendenning’s model are otherwise unchanged.

Assuming the cavern pressure to be constant is the most significant deficiency of the models of Glendenning [39], Glendenning et al. [69], and Frutschi [40]. Because of this assumption, the models can only be used for rough estimates of the plant efficiency. Other performance indicators such as the volumetric storage density, from which the cavern volume required to generate a specified amount of electrical energy may be deduced, cannot be determined. To the best knowledge of the author, only Grazzini and Milazzo [70, 41] presented analytical models of AA-CAES plants in which the time-dependence of the pressure of the compressed air was taken into account. Because they focused on above-ground storage vessels such as steel tanks, they assumed the vessels to be isothermal. This assumption does not hold for caverns, as demonstrated by measurements from the Huntorf plant and from the Swiss pilot plant, see Crotogino and Quast [67] and Geissbühler et al. [19].

Therefore, the first objective of this work is to derive “simple” analytical models of AA-CAES plants in which the cavern dynamics are included. (The meaning of “simple” will be made clear below.) In deriving our models, we restrict attention to the quasi-steady state, in which the plant states at the beginning and end of charging and discharging are independent of the number of cycles, and build on the work of Zaugg [38, 71], who analyzed two-stage expansion trains supplied with compressed air from caverns for several types of D-CAES plants. Our models can thus be viewed as a generalization of the models of Glendenning [39] and Glendenning et al. [69] to include the cavern dynamics and also as a generalization of the model of Zaugg [38] to include the compression train and the TES, thereby extending it to AA-CAES plants.

The second objective of our work is to use the newly derived analytical models to gain insight into the performance of AA-CAES plants and to summarize the results in the form of charts that can be used for the initial design of such plants. The initial design constitutes a starting point

for simulations with a numerical plant model, such as sensitivity studies, optimizations, and investigations of the plant performance under operating conditions that do not permit a quasi-steady state to be reached. It is the second objective that motivates the derivation of “simple” analytical models, by which we mean models that are as complex as required to yield useful insights, yet sufficiently simple to permit the manual manipulation of mathematical expressions that is needed to extract these insights.

Beyond using our analytical models to gain insight, we see another use that has so far received little attention in the field of energy research: the verification of numerical models. Here, “verification” is used in the sense of “solving the equations right”, see Oberkampf and Roy [72, p. 14], with the goal of ensuring that a numerical model solves the governing equations, irrespective of their physical accuracy, with good numerical accuracy. In other words, the analytical plant models presented below can be used to check that a numerical plant model, executed subject to the simplifying assumptions used in deriving the analytical model, gives numerically accurate results. After passing this check, results produced by the numerical model without the simplifying assumptions can be regarded as more trustworthy.

This chapter is structured as follows. It begins in section 3.2 by focussing on the simplest type of AA-CAES plant, i.e., with one-stage turbomachinery. Although such plants are of limited practical interest for bulk storage, they are of considerable theoretical interest since they exhibit the essential physical phenomena without the complications caused by multi-stage turbomachinery.² The performance of one-stage plants therefore serves as a reference to which the performance of multi-stage plants can be compared. In addition, deriving the model for one-stage plants entails much less algebra than for two-stage plants, permitting us to emphasize the central ideas underpinning our model. Since these ideas are independent of the number

²Storing large amounts of energy requires high pressures in the cavern. Compared to multiple intercooled stages, reaching high pressures with a single stage requires more work and leads to higher temperatures that necessitate costlier materials, see, e.g., Saravanamuttoo et al. [73, p. 53].

of stages, we compress the derivation of the model for two-stage plants in section 3.3 and instead concentrate on the key results. (A detailed derivation of the model for the two-stage plant can be found in Haselbacher and Roos [74].) The chapter closes with conclusions and an outlook.

3.2 One-stage plant

3.2.1 Plant layout, assumptions, and implications

The layout of the plant and the state numbering are shown in fig. 3.1. We make the following fundamental assumptions: the air is a thermally and calorically perfect gas; the mass flows during charging and discharging are constant; the compressor, turbine, and cavern are adiabatic; the flows between the components are isentropic; and the flow velocities are small enough to allow static and total temperatures to be taken to be equal.

The TES is treated as a black box, i.e., we make no assumptions about the storage medium and how thermal energy is transferred between the storage medium and the air. The plant model is therefore applicable to all types of sensible, latent, and thermochemical TES. However, we do assume that the TES incurs negligible thermal and pressure losses and that it delivers a constant outflow temperature during charging.³

Given the assumption of an adiabatic cavern, the quasi-steady state can only be attained if the mass and energy flowing into and out of the cavern during charging and discharging are equal, i.e.,

$$\dot{m}_c \Delta t_c = \dot{m}_d \Delta t_d = m_{cd} \quad (3.3)$$

³The assumption of a constant outflow temperature during charging may appear unrealistic. Although sensible, latent, and thermochemical TES can be designed to deliver constant or nearly constant outflow temperatures during charging and/or discharging, see, e.g., Ströhle et al. [25], Geissbühler et al. [32, 33], Becattini and Haselbacher [26], and Roos and Haselbacher [75], there is another reason why the assumption can be justified: AA-CAES plants are likely to employ heat exchangers between the TES and the cavern as a safety measure to ensure that the temperature of the air flowing into the cavern, and therefore the temperature of the air in the cavern, remain below a specified bound.

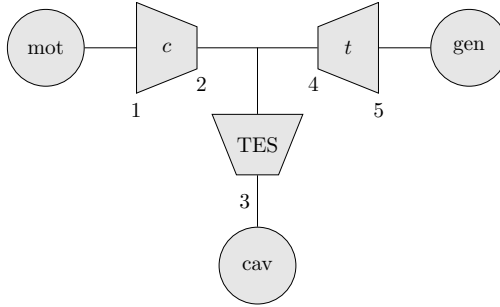


Figure 3.1: Layout of plant with one-stage turbomachinery and state numbering.

and

$$\dot{m}_c C_p T_{3,c} \Delta t_c = \dot{m}_d C_p \int_0^{\Delta t_d} T_{3,d}(t) dt, \quad (3.4)$$

where $T_{3,c}$ is the constant temperature of the air flowing into the cavern during charging and $T_{3,d}(t)$ is the time-dependent temperature of the air flowing out of the cavern during discharging. By defining the temporal averages

$$\bar{T}^c = \frac{1}{\Delta t_c} \int_0^{\Delta t_c} T(t) dt, \quad (3.5)$$

$$\bar{T}^d = \frac{1}{\Delta t_d} \int_0^{\Delta t_d} T(t) dt, \quad (3.6)$$

eqs. (3.3) and (3.4) imply that

$$T_{3,c} = \bar{T}_{3,d}^d = T_3. \quad (3.7)$$

As should be clear from the derivation of eq. (3.7), our model relies on defining averages of time-dependent quantities to fulfill the mass and energy balances over a charging-discharging cycle at the quasi-steady state.

Similarly, because the TES is assumed to be free of thermal losses, the quasi-steady state can only be attained if the thermal energy captured by

the TES during charging is released during discharging,

$$\dot{m}_c C_p \int_0^{\Delta t_c} (T_2(t) - T_{3,c}) dt = \dot{m}_d C_p \int_0^{\Delta t_d} (T_4(t) - T_{3,d}(t)) dt,$$

and using eqs. (3.3) and (3.5) to (3.7) implies that

$$\bar{T}_2^c = \bar{T}_4^d. \quad (3.8)$$

In the following, we assume that the compressor ingests air at atmospheric conditions, $p_1 = p_{\text{atm}}$ and $T_1 = T_{\text{atm}}$, and that the turbine exhaust is at atmospheric pressure, $p_5 = p_{\text{atm}}$. As the TES is assumed to be free of pressure losses, we have, during charging,

$$p_2(t) = p_3(t) = p_{\text{cav}}(t),$$

and during discharging,

$$p_3(t) = p_4(t) = p_{\text{cav}}(t).$$

3.2.2 Cavern and turbomachinery models

Because of the constant TES outflow temperature during charging and the lack of thermal losses between the TES and the cavern, the temperature of the air flowing into the cavern is constant, which means that we can use the cavern model of Zaugg [71]. For adiabatic conditions, the model predicts that during charging the pressure and temperature vary as

$$\frac{p_{\text{cav}}(t)}{p_{\text{cav},\text{min}}} = 1 + \gamma \frac{\dot{m}_c t}{m_{\text{cav},\text{min}}} \frac{T_3}{T_{\text{cav},\text{min}}}, \quad (3.9)$$

$$\frac{T_{\text{cav}}(t)}{T_{\text{cav},\text{min}}} = \frac{1 + \gamma \frac{\dot{m}_c t}{m_{\text{cav},\text{min}}} \frac{T_3}{T_{\text{cav},\text{min}}}}{1 + \frac{\dot{m}_c t}{m_{\text{cav},\text{min}}}}, \quad (3.10)$$

where $0 \leq t \leq \Delta t_c$ and $m_{\text{cav},\text{min}} = p_{\text{cav},\text{min}} V_{\text{cav}} / RT_{\text{cav},\text{min}}$. Conversely, following the same approach during discharging but assuming in addition

that the total temperature of the air flowing out of the cavern is equal to the (total) temperature of the air in the cavern gives

$$\frac{p_{\text{cav}}(t)}{p_{\text{cav,max}}} = \left(1 - \frac{\dot{m}_d t}{m_{\text{cav,max}}}\right)^\gamma, \quad (3.11)$$

$$\frac{T_{\text{cav}}(t)}{T_{\text{cav,max}}} = \left(1 - \frac{\dot{m}_d t}{m_{\text{cav,max}}}\right)^{\gamma-1}, \quad (3.12)$$

where $0 \leq t \leq \Delta t_d$ and $m_{\text{cav,max}} = p_{\text{cav,max}} V_{\text{cav}} / RT_{\text{cav,max}}$.⁴

Evaluating eqs. (3.11) and (3.12) at $t = \Delta t_d$ and putting $p_{\text{cav}}(\Delta t_d) = p_{\text{cav,min}}$ and $T_{\text{cav}}(\Delta t_d) = T_{\text{cav,min}}$ leads to the isentropic relation

$$\frac{T_{\text{cav,max}}}{T_{\text{cav,min}}} = \left(\frac{p_{\text{cav,max}}}{p_{\text{cav,min}}}\right)^{\frac{\gamma-1}{\gamma}}, \quad (3.13)$$

as previously pointed out by Osterle [78] and Kushnir et al. [77]. Because the cavern is assumed to be adiabatic, the final state of discharging equals the initial state of charging (and vice versa), so the charging must also obey eq. (3.13). However, due to mixing, the charging cannot be isentropic. This apparent contradiction is resolved by the interplay between the entropy flowing into the cavern and the entropy created by mixing, resulting in the non-monotonic behavior of the entropy in the cavern depicted in fig. 3.2.⁵ The figure also shows the difference between the behavior of the pressure during charging and discharging. This difference has a quantitatively small, but conceptually important impact on the plant efficiency that will be discussed in section 3.2.6.

Thanks to the assumption that the flow velocities are small enough to obviate the distinction between static and total temperatures, we set

⁴Assuming the total temperature of the air to be constant is not, strictly speaking, justified since the substantial derivative of the total temperature is proportional to the temporal derivative of the pressure, see, e.g., Owczarek [76, p. 76]. Haselbacher and Roos [74] show that the order of magnitude of the temporal derivative of the pressure can be estimated to be $(\gamma - 1)\dot{m}_d T_3 / \rho_{\text{cav,min}} V_{\text{cav}}$. Although eqs. (3.11) and (3.12) were not given by Zaugg [71], they were very likely known to him. In slightly different form, the equations appear to have been first published by Kushnir et al. [77].

⁵See Haselbacher and Roos [74] for a full analysis.

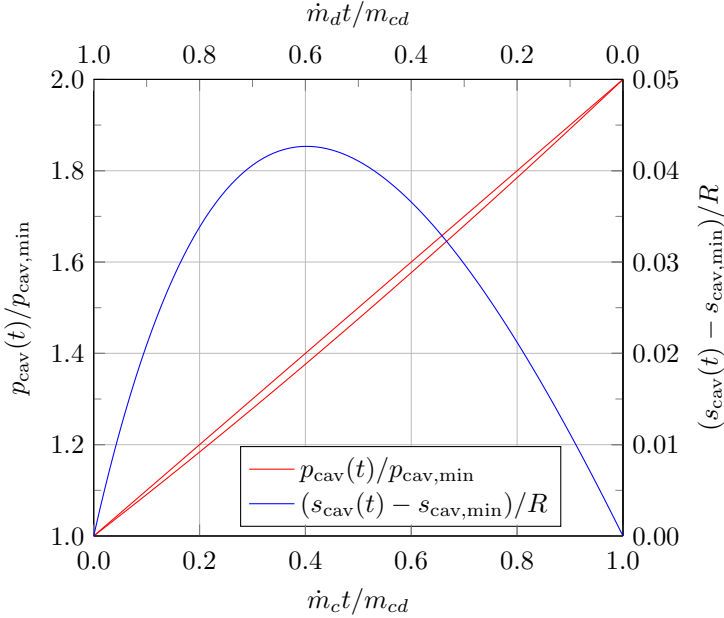


Figure 3.2: $p_{cav}(t)/p_{min}$ as a function of time during charging and discharging, determined from eqs. (3.9) and (3.11), respectively, and the entropy during charging as a function of time for $p_{cav,max}/p_{cav,min} = 2$ and $\gamma = 1.4$. During discharging, $s_{cav}(t) = s_{cav,min}$.

$T_{3,d}(t) = T_{cav}(t)$ and find from eqs. (3.6) and (3.7) that

$$\frac{T_3}{T_{cav,max}} = \frac{1 - \frac{p_{cav,min}}{p_{cav,max}}}{\gamma \left[1 - \left(\frac{p_{cav,min}}{p_{cav,max}} \right)^{\frac{1}{\gamma}} \right]} \quad (3.14)$$

and using eq. (3.13) gives

$$\frac{T_3}{T_{\text{cav,min}}} = \frac{T_3}{T_{\text{cav,max}}} \frac{T_{\text{cav,max}}}{T_{\text{cav,min}}} = \frac{\frac{p_{\text{cav,max}}}{p_{\text{cav,min}}} - 1}{\gamma \left[\left(\frac{p_{\text{cav,max}}}{p_{\text{cav,min}}} \right)^{\frac{1}{\gamma}} - 1 \right]}. \quad (3.15)$$

These equations should be interpreted as determining $T_{\text{cav,max}}$ and $T_{\text{cav,min}}$ given $p_{\text{cav,max}}/p_{\text{cav,min}}$, γ , and T_3 . Because we treat the TES as a black box, our model cannot determine T_3 . Instead, it must be supplied as an input parameter, chosen to satisfy $T_{\text{atm}} \leq T_3 \leq T_2(\Delta t_c)$.

The electrical energy consumed by the motor is

$$E_{\text{el,mot}} = \frac{1}{\eta_{\text{mot}}\eta_{m,c}} \int_0^{\Delta t_c} \dot{W}_c(t) dt, \quad (3.16)$$

where η_{mot} is the motor efficiency, $\eta_{m,c}$ is the mechanical efficiency of the compressor, and $\dot{W}_c(t)$ is the power consumed by the compressor,

$$\dot{W}_c(t) = \frac{\dot{m}_c C_p T_{\text{atm}}}{\eta_{s,c}} \left[\left(\frac{p_{\text{cav}}(t)}{p_{\text{atm}}} \right)^{\frac{\gamma-1}{\gamma}} - 1 \right].$$

Substituting from eqs. (3.9) and (3.15) and integrating results in

$$E_{\text{el,mot}} = \frac{\gamma}{\gamma-1} \frac{p_{\text{cav,min}} V_{\text{cav}}}{\eta_{\text{mot}}\eta_{m,c}\eta_{s,c}} \frac{T_{\text{atm}}}{T_3} f_c, \quad (3.17)$$

where

$$f_c = \frac{1}{2\gamma-1} \left(\frac{p_{\text{cav,min}}}{p_{\text{atm}}} \right)^{\frac{\gamma-1}{\gamma}} \left[\left(\frac{p_{\text{cav,max}}}{p_{\text{cav,min}}} \right)^{\frac{2\gamma-1}{\gamma}} - 1 \right] - \frac{1}{\gamma} \left(\frac{p_{\text{cav,max}}}{p_{\text{cav,min}}} - 1 \right). \quad (3.18)$$

The electrical energy produced by the generator is

$$E_{\text{el,gen}} = \eta_{\text{gen}}\eta_{m,t} \int_0^{\Delta t_d} \dot{W}_t(t) dt, \quad (3.19)$$

where η_{gen} is the generator efficiency, $\eta_{m,t}$ is the mechanical efficiency of the turbine, and $\dot{W}_t(t)$ is the power produced by the turbine,

$$\dot{W}_t(t) = \eta_{s,t} \dot{m}_d C_p T_4(t) \left[1 - \left(\frac{p_{\text{atm}}}{p_{\text{cav}}(t)} \right)^{\frac{\gamma-1}{\gamma}} \right]. \quad (3.20)$$

Evaluating the integral requires that the temporal dependence of $T_4(t)$ and $p_{\text{cav}}(t)$ be specified. For the latter, we use eq. (3.11). For the former, two obvious approaches exist. We could set

$$T_4(t) = T_2(\Delta t_c - rt), \quad (3.21)$$

where $r = \Delta t_c / \Delta t_d$, which ensures that $T_4(0) = T_2(\Delta t_c)$ and $T_4(\Delta t_d) = T_2(0)$ and which can be viewed as the result of a TES whose outflow temperature profile during discharging mirrors the inflow temperature profile during charging. Unfortunately, substituting eqs. (3.20) and (4.5) into eq. (3.19) and integrating leads to the hypergeometric function ${}_2F_1$, whose complexity makes extracting physical insights difficult. Alternatively, we can approximate the troublesome integral,

$$\int_0^{\Delta t_d} T_4(t) \left(\frac{p_{\text{atm}}}{p_{\text{cav}}(t)} \right)^{\frac{\gamma-1}{\gamma}} dt \approx \bar{T}_4^d \int_0^{\Delta t_d} \left(\frac{p_{\text{atm}}}{p_{\text{cav}}(t)} \right)^{\frac{\gamma-1}{\gamma}} dt, \quad (3.22)$$

and use eq. (3.8),

$$\bar{T}_4^d \int_0^{\Delta t_d} \left(\frac{p_{\text{atm}}}{p_{\text{cav}}(t)} \right)^{\frac{\gamma-1}{\gamma}} dt = \bar{T}_2^c \int_0^{\Delta t_d} \left(\frac{p_{\text{atm}}}{p_{\text{cav}}(t)} \right)^{\frac{\gamma-1}{\gamma}} dt,$$

which can be viewed as the result of a TES whose outflow temperature profile is constant during discharging. The second approach has the advantage that the integral in eq. (3.19) is easily evaluated, resulting in

$$E_{\text{el,gen}} = \frac{\gamma}{\gamma-1} \eta_{\text{gen}} \eta_{m,t} \eta_{s,t} p_{\text{cav,max}} V_{\text{cav}} \frac{T_{\text{atm}}}{T_{\text{cav,max}}} f_t, \quad (3.23)$$

where

$$f_t = \frac{\bar{T}_2^c}{T_{\text{atm}}} \left\{ 1 - \left(\frac{p_{\text{cav,min}}}{p_{\text{cav,max}}} \right)^{\frac{1}{\gamma}} - \frac{1}{2-\gamma} \left(\frac{p_{\text{atm}}}{p_{\text{cav,max}}} \right)^{\frac{\gamma-1}{\gamma}} \left[1 - \left(\frac{p_{\text{cav,min}}}{p_{\text{cav,max}}} \right)^{\frac{2-\gamma}{\gamma}} \right] \right\}, \quad (3.24)$$

with $\bar{T}_2^c / T_{\text{atm}}$ determined from

$$\frac{T_2(t)}{T_{\text{atm}}} = 1 + \frac{1}{\eta_{s,c}} \left[\left(\frac{p_{\text{cav}}(t)}{p_{\text{atm}}} \right)^{\frac{\gamma-1}{\gamma}} - 1 \right] \quad (3.25)$$

and eqs. (3.5), (3.9), and (3.15) as

$$\frac{\bar{T}_2^c}{T_{\text{atm}}} = 1 + \frac{1}{\eta_{s,c}} \left(\frac{\gamma}{2\gamma - 1} \left(\frac{p_{\text{cav,min}}}{p_{\text{atm}}} \right)^{\frac{\gamma-1}{\gamma}} \frac{\left(\frac{p_{\text{cav,max}}}{p_{\text{cav,min}}} \right)^{\frac{2\gamma-1}{\gamma}} - 1}{\frac{p_{\text{cav,max}}}{p_{\text{cav,min}}} - 1} - 1 \right). \quad (3.26)$$

We emphasize that deriving a simple analytical model requires an approximation to integrate eq. (3.20). The need for an approximation, coupled with the availability and flexibility of numerical models, may be why previous authors, such as Glendenning [39] and Glendenning et al. [69], did not develop analytical models that account for the time-dependent pressures and temperatures caused by the filling and emptying of an adiabatic cavern. The derivation of our analytical model hinges on approximation (3.22). This approximation will be shown in section 3.2.6 to underpredict the turbine work with a maximum relative error of less than 0.64%. The small errors are believed to be at least partly due to eq. (3.8), which ensures that the enthalpy flowing into the turbine equals the enthalpy flowing out of the compressor.

For the remainder of this section, whenever quantitative results are presented, we assume that $p_{\text{atm}} = 1 \text{ atm}$, $\eta_{\text{mot}} = \eta_{\text{gen}} = \eta_{m,c} = \eta_{m,t} = 0.98$ and $\gamma = 1.4$.

3.2.3 Plant efficiency

The plant efficiency follows from eqs. (3.17) and (3.23) as

$$\eta = \frac{E_{\text{el,gen}}}{E_{\text{el,mot}}} = \eta_{\text{mot}} \eta_{\text{gen}} \eta_{m,c} \eta_{m,t} f_{\eta}, \quad (3.27)$$

where

$$f_{\eta} = \eta_{s,c} \eta_{s,t} \frac{p_{\text{cav,max}}}{p_{\text{cav,min}}} \frac{T_3}{T_{\text{cav,max}}} \frac{f_t}{f_c}$$

can be viewed as the plant efficiency in the absence of mechanical losses and the losses incurred by the motor and generator. Substituting from eq. (3.14),

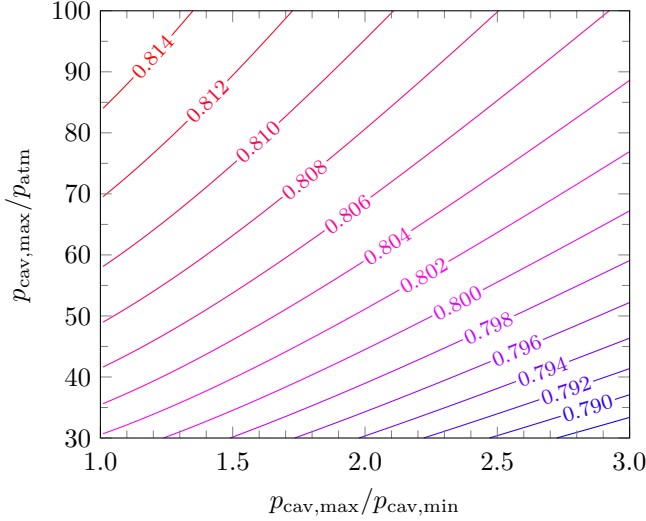


Figure 3.3: The function f_η given by eq. (3.28) as a function of $p_{\text{cav,max}}/p_{\text{cav,min}}$ and $p_{\text{cav,max}}/p_{\text{atm}}$ for $\eta_{s,c} = \eta_{s,t} = 0.85$ and $\gamma = 1.4$.

we can write

$$f_\eta = \eta_{s,c} \eta_{s,t} \frac{\frac{p_{\text{cav,max}}}{p_{\text{cav,min}}} \left(1 - \frac{p_{\text{cav,min}}}{p_{\text{cav,max}}} \right)}{\gamma \left[1 - \left(\frac{p_{\text{cav,min}}}{p_{\text{cav,max}}} \right)^{\frac{1}{\gamma}} \right]} \frac{f_t}{f_c}, \quad (3.28)$$

showing that f_η depends only on $\eta_{s,c}$, $\eta_{s,t}$, $p_{\text{cav,max}}/p_{\text{cav,min}}$, $p_{\text{cav,max}}/p_{\text{atm}}$, and γ and that it is independent of the input parameter T_3 because both the TES and the cavern were assumed to be free of thermal losses.

Figure 3.3 presents f_η as a function of $p_{\text{cav,max}}/p_{\text{cav,min}}$ and $p_{\text{cav,max}}/p_{\text{atm}}$ for $\eta_{s,c} = \eta_{s,t} = 0.85$. The figure shows that f_η increases with increasing $p_{\text{cav,max}}/p_{\text{atm}}$ and decreasing $p_{\text{cav,max}}/p_{\text{cav,min}}$. The former trend is consistent with that predicted by the model of Glendenning [39]. The latter cannot be predicted by Glendenning's model and appears to be a new result. Figure 3.3 also shows that f_η is quite insensitive to the pressure ratios. For

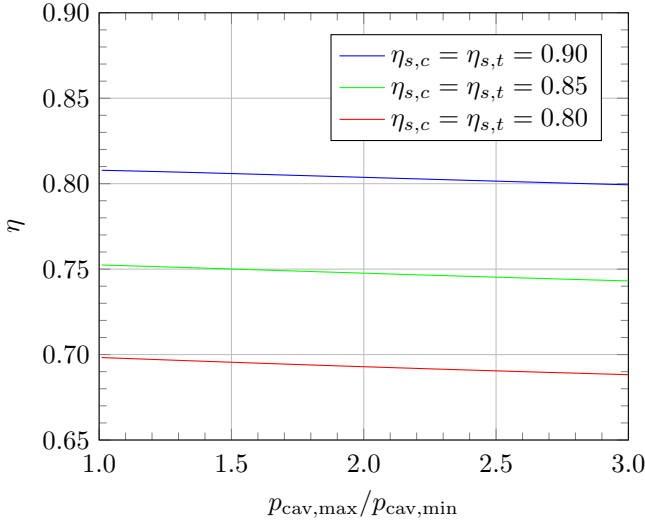


Figure 3.4: The plant efficiency given by eq. (3.27) as a function of $p_{cav,max}/p_{cav,min}$ and $\eta_{s,c}$ and $\eta_{s,t}$ for $p_{cav,max}/p_{atm} = 100$, $\eta_{mot} = \eta_{gen} = \eta_{m,c} = \eta_{m,t} = 0.98$, and $\gamma = 1.4$.

example, taking $p_{cav,max}/p_{atm} = 80$, doubling $p_{cav,max}/p_{cav,min}$ from 1.5 to 3.0 causes f_η to decrease from 0.811 to 0.803, corresponding to a change of less than 1%.

In contrast to the insensitivity to the pressure ratios, the plant efficiency is very sensitive to changes in the turbomachinery efficiencies. This is made clear by fig. 3.4, which presents η as a function of $p_{cav,max}/p_{cav,min}$, $\eta_{s,c}$, and $\eta_{s,t}$ for $p_{cav,max}/p_{atm} = 100$. Increasing both $\eta_{s,c}$ and $\eta_{s,t}$ by 0.05 is seen to increase η by about 0.05. Haselbacher and Roos [74] show that $\partial\eta/\partial\eta_{s,t}$ is about three to four times larger than $\partial\eta/\partial\eta_{s,c}$.

Equations (3.27) and (3.28) can be used to substantiate our claim that our model is a generalization of the model of Glendenning [39], who assumed the cavern pressure to be constant. This implies that $p_{cav,max}/p_{cav,min} = 1$ and therefore Glendenning's model effectively corresponds to the left boundary

of fig. 3.3. Indeed, by substituting $p_{\text{cav,max}}/p_{\text{cav,min}} = 1 + \varepsilon$ into eq. (3.28), it can be shown that

$$\lim_{\varepsilon \rightarrow 0} \eta = \eta_{\text{mot}} \eta_{\text{gen}} \eta_{m,c} \eta_{m,t} \eta_{s,t} \frac{\left[\eta_{s,c} + \left(\frac{p_{\text{cav}}}{p_{\text{atm}}} \right)^{\frac{\gamma-1}{\gamma}} - 1 \right] \left[1 - \left(\frac{p_{\text{atm}}}{p_{\text{cav}}} \right)^{\frac{\gamma-1}{\gamma}} \right]}{\left(\frac{p_{\text{cav}}}{p_{\text{atm}}} \right)^{\frac{\gamma-1}{\gamma}} - 1},$$

and simplifying and setting $\eta_{\text{mot}} = \eta_{\text{gen}} = \eta_{m,c} = \eta_{m,t} = 1$ leads to eq. (3.1). Since eq. (3.9) indicates that $p_{\text{cav,max}}/p_{\text{cav,min}} \rightarrow 1$ requires that $m_{\text{cd}}/V_{\text{cav}} \rightarrow 0$, our model can therefore be said to generalize Glendenning's model from vanishing to finite values of $m_{\text{cd}}/V_{\text{cav}}$. Whereas Glendenning's model is restricted to estimating the efficiency, our generalized model can also be used to estimate other performance indicators such as the storage capacity and density.

3.2.4 Storage capacity and density

If the storage capacity of the plant is defined in terms of the electrical energy generated during discharging, eq. (3.23) can be recast as an expression for a non-dimensional storage capacity,

$$\frac{E_{\text{el,gen}}}{p_{\text{cav,max}} V_{\text{cav}}} = \frac{\gamma}{\gamma - 1} \eta_{\text{gen}} \eta_{m,t} \eta_{s,t} \frac{T_{\text{atm}}}{T_3} \frac{T_3}{T_{\text{cav,max}}} f_t. \quad (3.29)$$

Figure 3.5 presents $E_{\text{el,gen}}/p_{\text{cav,max}} V_{\text{cav}}$ as a function of $p_{\text{cav,max}}/p_{\text{cav,min}}$ and $p_{\text{cav,max}}/p_{\text{atm}}$ for $\eta_{s,c} = \eta_{s,t} = 0.85$ and $T_3/T_{\text{atm}} = 1$. We observe that a large non-dimensional capacity requires both $p_{\text{cav,max}}/p_{\text{cav,min}}$ and $p_{\text{cav,max}}/p_{\text{atm}}$ to be large and that as $p_{\text{cav,max}}/p_{\text{cav,min}} \rightarrow 1$, the non-dimensional capacity becomes independent of $p_{\text{cav,max}}/p_{\text{atm}}$. In addition, we note that the non-dimensional capacity is generally very sensitive to changes in the pressure ratios. Given $p_{\text{cav,max}}/p_{\text{atm}} = 80$, for example, doubling $p_{\text{cav,max}}/p_{\text{cav,min}}$ from 1.5 to 3 causes the non-dimensional capacity to change from 1.77 to 3.15, representing an increase of about 78%.

These observations highlight two differences between the non-dimensional capacity and the efficiency: For a specified $p_{\text{cav,max}}/p_{\text{atm}}$, large values of the

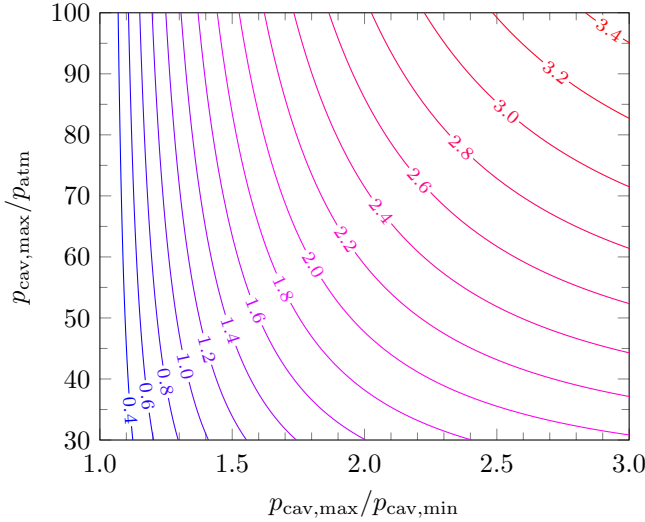


Figure 3.5: $E_{\text{el,gen}}/p_{\text{cav,max}}V_{\text{cav}}$ given by eq. (3.29) as a function of $p_{\text{cav,max}}/p_{\text{cav,min}}$ and $p_{\text{cav,max}}/p_{\text{atm}}$ for $\eta_{\text{gen}} = \eta_{m,t} = 0.98$, $\eta_{s,c} = \eta_{s,t} = 0.85$, $T_3/T_{\text{atm}} = 1$, and $\gamma = 1.4$.

former require large values of $p_{\text{cav,max}}/p_{\text{cav,min}}$, whereas high values of the latter require small values of $p_{\text{cav,max}}/p_{\text{cav,min}}$. Furthermore, while the non-dimensional capacity is very sensitive to the pressure ratios, the efficiency is not. These differences suggest that $p_{\text{cav,max}}/p_{\text{cav,min}}$ should be chosen to give a large non-dimensional capacity, which leads to at least two advantages. First, the cavern volume can be reduced for a given $p_{\text{cav,max}}$, simplifying the search for a suitable plant site and lowering the cost of leaching out or excavating the cavern. Conversely, $p_{\text{cav,max}}$ can be reduced for a given cavern volume, which reduces the maximum stresses in the salt deposits or rock surrounding the cavern and may therefore simplify the search for a suitable plant site. Second, a large non-dimensional capacity provides a plant with the flexibility to participate in multiple electricity markets and thereby increases the likelihood of the plant being profitable.

In choosing a plant site, another property of the non-dimensional capacity may be relevant. Figure 3.5 shows that a given non-dimensional capacity can be achieved by a range of values of $p_{\text{cav,max}}/p_{\text{cav,min}}$ and $p_{\text{cav,max}}/p_{\text{atm}}$. For example, $E_{\text{el,gen}}/p_{\text{cav,max}}V_{\text{cav}} = 2.6$ can be attained for $p_{\text{cav,max}}/p_{\text{cav,min}} = 1.87$ and $p_{\text{cav,max}}/p_{\text{atm}} = 100$, but also for $p_{\text{cav,max}}/p_{\text{cav,min}} = 3$ and $p_{\text{cav,max}}/p_{\text{atm}} = 52.35$. If the salt deposits or rock in which the cavern is to be constructed impose a limit on the maximum stress, a lower value of $p_{\text{cav,max}}/p_{\text{atm}}$ could be compensated by a larger value of $p_{\text{cav,max}}/p_{\text{cav,min}}$.

Equation (3.29) can be used to derive values for the volumetric storage density $E_{\text{el,gen}}/V_{\text{cav}}$, which is plotted in fig. 3.6 as a function of $p_{\text{cav,max}}$ and $p_{\text{cav,max}}/p_{\text{cav,min}}$ for $\eta_{s,c} = \eta_{s,t} = 0.85$ and $T_3/T_{\text{atm}} = 1$. The values shown in fig. 3.6 can be put into context by relating them to those of pumped hydropower storage (PHS), with which AA-CAES is often compared. For a closed-loop PHS plant without losses, the volumetric storage density is $\rho g \Delta h / 2$, where ρ is the water density, g is the gravitational acceleration, and Δh is the elevation difference. Taking $\rho = 1000 \text{ kg/m}^3$, $g = 9.81 \text{ m/s}^2$, and $\Delta h = 1000 \text{ m}$ results in 1.36 kWh/m^3 .⁶

3.2.5 Cavern volume

The cavern volume required for a specified amount of electrical energy produced by the generator can also be estimated from eq. (3.29). Since the cavern volume is directly proportional to the generated electrical energy, we can estimate the volume for a reference amount of electrical energy and then scale the volume accordingly. In fig. 3.7, the cavern volume required for $E_{\text{el,gen}} = 10 \text{ MWh}$ is plotted as a function of $p_{\text{cav,max}}/p_{\text{cav,min}}$ and $p_{\text{cav,max}}/p_{\text{atm}}$ for $T_3/T_{\text{atm}} = 1$. Assuming that $p_{\text{cav,max}}/p_{\text{atm}} = 100$ and $p_{\text{cav,max}}/p_{\text{cav,min}} = 1.4$, the figure indicates that $V_{\text{cav}} \approx 2110 \text{ m}^3$. If 500 MWh of electrical energy are to be provided by the plant, a cavern volume of $V_{\text{cav}} \approx 50 \cdot 2110 \text{ m}^3 \approx 105\,500 \text{ m}^3$ is thus required.

⁶The elevation difference of 1000 m was deliberately chosen to be optimistic. Although PHS plants with elevation differences of about 1000 m exist, typical elevation differences are 200–400 m, see, e.g., Giesecke et al. [79, p. 730].

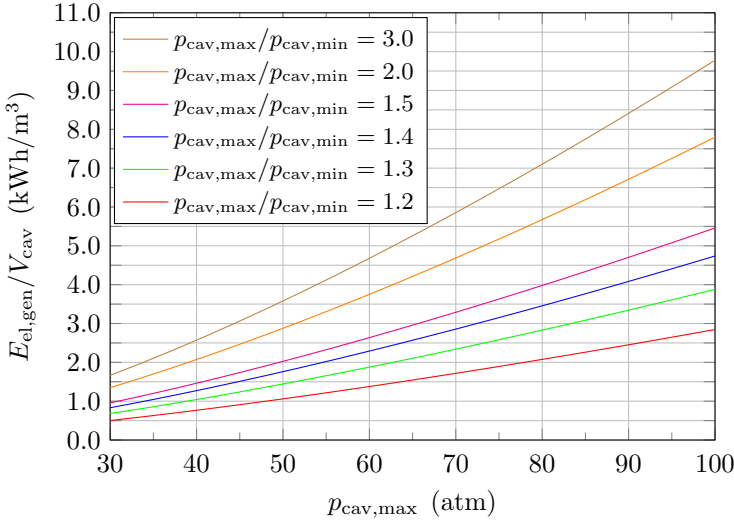


Figure 3.6: $E_{el,gen}/V_{cav}$ derived from eq. (3.29) as a function of $p_{cav,max}$ and $p_{cav,max}/p_{cav,min}$ for $p_{atm} = 1$ atm, $\eta_{gen} = \eta_{m,t} = 0.98$, $\eta_{s,c} = \eta_{s,t} = 0.85$, $T_3/T_{atm} = 1$, and $\gamma = 1.4$.

3.2.6 Discussion

Two points related to the foregoing analysis merit discussion. The first relates to approximation (3.22). To quantify its impact, we can compare the generated electrical energy derived from that approximation, i.e., eq. (3.23), to the energy obtained by replacing the approximation with eq. (4.5),

$$\int_0^{\Delta t_d} T_4(t) \left(\frac{p_{atm}}{p_{cav}(t)} \right)^{\frac{\gamma-1}{\gamma}} dt = \int_0^{\Delta t_d} T_2(\Delta t_c - rt) \left(\frac{p_{atm}}{p_{cav}(t)} \right)^{\frac{\gamma-1}{\gamma}} dt. \quad (3.30)$$

Substituting for $T_2(t)$ from eq. (4.6) (in which $p_{cav}(t)/p_{atm}$ is obtained from eq. (3.9)) and for $p_{cav}(t)/p_{atm}$ from eq. (3.11) results in eq. (3.23) with f_t replaced by

$$f_{t,e} = \frac{\bar{T}_2^c}{T_{atm}} \left[1 - \left(\frac{p_{cav,min}}{p_{cav,max}} \right)^{\frac{1}{\gamma}} \right] \left[1 - \frac{T_{atm}}{\bar{T}_2^c} \left(\frac{p_{atm}}{p_{cav,max}} \right)^{\frac{\gamma-1}{\gamma}} I \right], \quad (3.31)$$

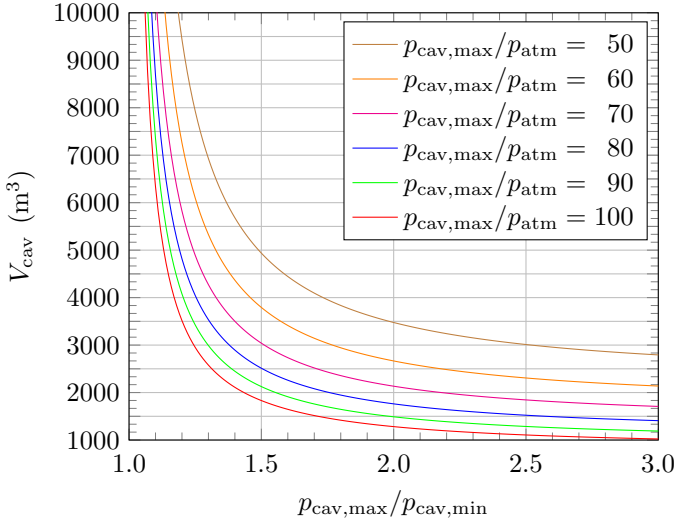


Figure 3.7: V_{cav} required for $E_{\text{el,gen}} = 10 \text{ MWh}$ derived from eq. (3.29) as a function of $p_{\text{cav,max}}/p_{\text{cav,min}}$ and $p_{\text{cav,max}}/p_{\text{atm}}$ for $\eta_{s,c} = \eta_{s,t} = 0.85$, $\eta_{\text{gen}} = \eta_{m,t} = 0.98$, $T_3/T_{\text{atm}} = 1$, $p_{\text{atm}} = 1 \text{ atm}$, and $\gamma = 1.4$.

where the subscript e indicates that we regard this as an exact rather than as an approximate result and where

$$I = \int_0^1 \left(1 + \frac{1}{\eta_{s,c}} \left\{ \left[\frac{p_{\text{cav,min}}}{p_{\text{atm}}} \left(1 + \gamma \frac{m_{cd}(1-\xi)}{m_{\text{cav,min}}} \frac{T_3}{T_{\text{cav,min}}} \right) \right]^{\frac{\gamma-1}{\gamma}} - 1 \right\} \left(1 - \frac{m_{cd}\xi}{m_{\text{cav,max}}} \right)^{-(\gamma-1)} d\xi, \quad (3.32) \right)$$

with $\xi = t/\Delta t_d$ is the integral that was stated in section 3.2.2 to lead to the hypergeometric function. The impact of the approximation on the generated electrical energy can therefore be quantified by the relative error

$$\varepsilon = \frac{f_t}{f_{t,e}} - 1, \quad (3.33)$$

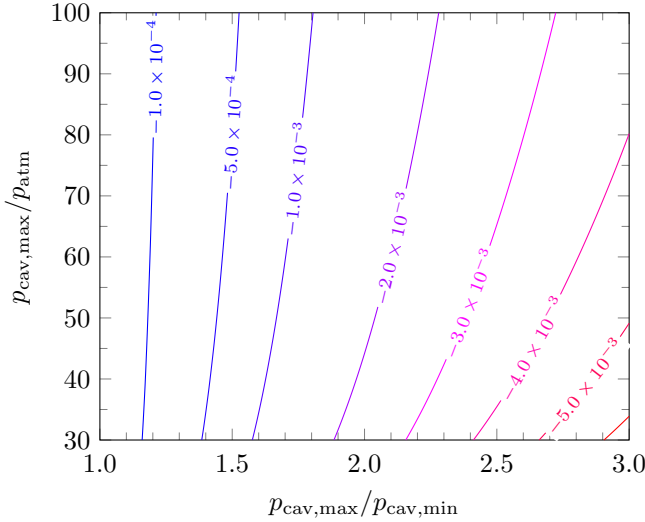


Figure 3.8: The relative error in the generated electrical energy defined by eq. (3.33) as a function of $p_{\text{cav,max}}/p_{\text{cav,min}}$ and $p_{\text{cav,max}}/p_{\text{atm}}$ for $\eta_{s,c} = 0.85$ and $\gamma = 1.4$. Note the unequal spacing of the isolines.

and evaluating I using numerical quadrature. (In the following, the midpoint rule with 800 steps was used, giving quadrature errors well below plotting accuracy.) The relative error is presented in fig. 3.8 for $\eta_{s,c} = 0.85$. The error is seen to be negative, so approximation (3.22) underestimates the generated electrical energy and thus also the plant efficiency. Moreover, the largest magnitude of the error is 0.64%. Given the purpose and simplicity of the model, this is an excellent result.

The second point concerns f_η , which, as stated above, can be regarded as the plant efficiency in the absence of mechanical losses and the losses incurred by the motor and generator. It might be expected, therefore, that setting $\eta_{s,c} = \eta_{s,t} = 1$ in eq. (3.28) gives $f_\eta = 1$. This expectation turns out to be wrong, as $f_\eta - 1$ is not zero; the largest deviation of about -0.012 occurs at $p_{\text{cav,max}}/p_{\text{atm}} = 30$ and $p_{\text{cav,max}}/p_{\text{cav,min}} = 3$. Suspecting

approximation (3.22) as the cause for the deviations happens to be only partially correct, as evaluating f_η with $f_{t,e}$ instead of f_t merely cuts the largest deviation by about half. The remaining deviations are explained by the different behavior of the cavern pressure during charging and discharging. This can be shown by substituting for $p_{cav}(t)/p_{atm}$ in eq. (3.30) not from eq. (3.11) but from eq. (3.9), giving

$$\frac{p_{atm}}{p_{cav}(t)} = \frac{p_{atm}}{p_{cav,min}} \left(1 + \gamma \frac{\dot{m}_c(\Delta t_c - rt)}{m_{cav,min}} \frac{T_3}{T_{cav,min}} \right)^{-1}, \quad (3.34)$$

which forces the variation of the cavern pressure during discharging to be equal to that during charging. The resulting integral differs from eq. (3.32) only through the second factor in the integrand, is easily evaluated for $\eta_{s,c} = 1$, and with $\eta_{s,t} = 1$ can be shown to lead to $f_\eta = 1$.

Since the different behavior of the cavern pressure during charging and discharging is an unavoidable consequence of the charging process being non-isentropic, we conclude that even if the TES and the turbomachinery are free of losses, AA-CAES plants cannot attain 100% efficiency. This conclusion, which is consistent with the analysis of Osterle [78], is of limited practical relevance because the efficiency penalty is very small, but it illustrates how physical insights can be extracted from our model.

3.3 Two-stage plant

The analysis of the one-stage plant showed that high values of $p_{cav,max}/p_{atm}$ may be required to reach high efficiencies and volumetric energy densities. Reaching high values of $p_{cav,max}/p_{atm}$ in a single-stage compressor leads to high compressor outflow temperatures, see fig. 3.9, which assumes an inflow temperature of 15 °C. Higher temperatures complicate the construction of the compressor and the TES. Splitting the compression into two stages can lead to a considerable reduction in the outflow temperature. For example, fig. 3.9 shows that compressing atmospheric air to 100 bar in one stage leads to 940 °C. By contrast, using two stages, each with a pressure ratio of 10, and using a TES between the two stages to cool the air flowing into the

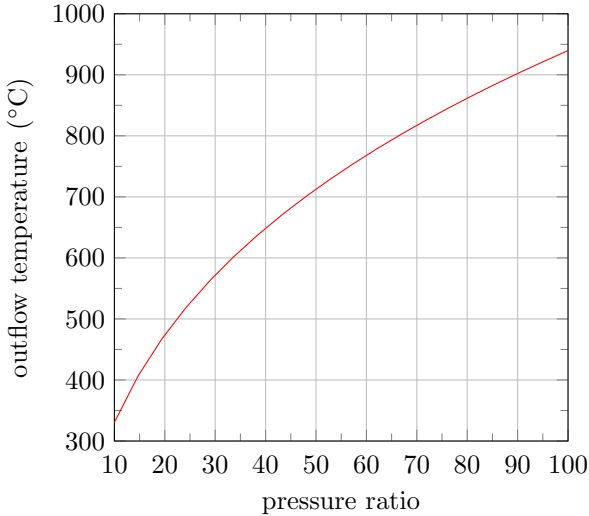


Figure 3.9: The compressor outflow temperature as a function of the pressure ratio for an inflow temperature of $15\text{ }^{\circ}\text{C}$, $\eta_{s,c} = 0.85$, and $\gamma = 1.4$.

second stage to $15\text{ }^{\circ}\text{C}$, leads only to $331\text{ }^{\circ}\text{C}$. The motivation for deriving a model of a two-stage plant is therefore clear.

The model derived below rests on the same fundamental assumptions as the model for the one-stage plant. To simplify the derivation, additional assumptions are made that will be stated below.

3.3.1 Plant layout, assumptions, and implications

The layout of the two-stage plant and the state numbering are presented in fig. 3.10. It should be noted that in contrast to two-stage plants investigated by other authors, see, e.g., Barbour et al. [35] and Sciacovelli et al. [17], our plant contains two TES units and two caverns. The purpose of the low-pressure cavern in a real two-stage plant is to house the TES that cools the air exiting the low-pressure compressor and subsequently heats the air entering the low-pressure turbine. For TES with direct contact between the

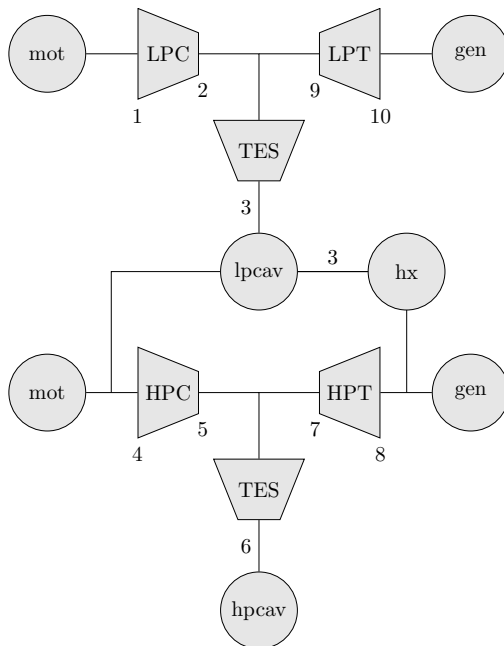


Figure 3.10: Layout of plant with two-stage turbomachinery and state numbering.

air and the storage material, such as packed beds, the benefit of placing the storage in a cavern is that the storage structure does not have to withstand large pressure loads, simplifying the construction and lowering costs. (In the Swiss pilot plant, the TES was placed in the cavern, see Geissbühler et al. [19].)

The pressure in the low-pressure cavern, denoted by p_{lpcav} , is assumed to remain constant to enable the low-pressure compressor and turbine to operate at constant pressure ratios. Therefore,

$$\frac{T_2}{T_{\text{atm}}} = 1 + \frac{1}{\eta_{s,\text{lpc}}} \left[\left(\frac{p_{\text{lpcav}}}{p_{\text{atm}}} \right)^{\frac{\gamma-1}{\gamma}} - 1 \right] = \text{constant}. \quad (3.35)$$

In section 3.3.6, a condition will be derived that ensures constant pressure

in the low-pressure cavern. It is important to note that the existence of the low-pressure cavern is not required for the derivation of the model; the constant pressure in the cavern can simply be thought of as a constant intermediate pressure. Similarly, because the TES units are assumed to be adiabatic, whether they are placed inside or outside the caverns is immaterial for the derivation of the model.

The heat exchanger that is placed between the high-pressure turbine and the low-pressure cavern is assumed to deliver an outflow temperature equal to the constant outflow temperature of the low-pressure TES. As a result, we put

$$T_{1\text{pcav}} = T_3, \quad (3.36)$$

$$T_4 = T_3. \quad (3.37)$$

and the energy balance of the low-pressure TES reduces to

$$T_9 = T_2. \quad (3.38)$$

To attain a quasi-steady state, the mass and energy flowing into and out of the high-pressure cavern must be equal. Therefore, eq. (3.3) holds for the two-stage plant also, eq. (3.7) becomes

$$T_{6,c} = \bar{T}_{6,d}^d = T_6, \quad (3.39)$$

and the energy balance for the high-pressure TES simplifies to

$$\bar{T}_7^d = \bar{T}_5^c. \quad (3.40)$$

Because the low-pressure compressor ingests air at atmospheric conditions, $p_1 = p_{\text{atm}}$ and $T_1 = T_{\text{atm}}$, and since the low-pressure turbine exhaust is at atmospheric pressure, $p_{10} = p_{\text{atm}}$. As the low- and high-pressure TES are assumed to be free of pressure losses, we have during charging

$$\begin{aligned} p_2 &= p_3 = p_4 = p_{1\text{pcav}}, \\ p_5(t) &= p_6(t) = p_{\text{hpcav}}(t), \end{aligned}$$

and during discharging,

$$p_4 = p_{\text{lp cav}},$$

$$p_6(t) = p_7(t) = p_{\text{hpcav}}(t),$$

and assuming the heat exchanger to be free of pressure losses also gives

$$p_8 = p_9 = p_{\text{lp cav}}.$$

3.3.2 Cavern and turbomachinery models

Since the formulation of the cavern and turbomachinery models for the two-stage plant closely follows that for the one-stage plant, the following merely states the relations that are important for subsequent derivations and the use of the plant model.

The evolutions of the pressure and temperature in the high-pressure cavern during charging follow from eqs. (3.9) and (3.10) as

$$\frac{p_{\text{hpcav}}(t)}{p_{\text{hpcav},\text{min}}} = 1 + \gamma \frac{\dot{m}_c t}{m_{\text{hpcav},\text{min}}} \frac{T_6}{T_{\text{hpcav},\text{min}}}, \quad (3.41)$$

$$\frac{T_{\text{hpcav}}(t)}{T_{\text{hpcav},\text{min}}} = \frac{1 + \gamma \frac{\dot{m}_c t}{m_{\text{hpcav},\text{min}}} \frac{T_3}{T_{\text{hpcav},\text{min}}}}{1 + \frac{\dot{m}_c t}{m_{\text{hpcav},\text{min}}}}, \quad (3.42)$$

where $m_{\text{hpcav},\text{min}} = p_{\text{hpcav},\text{min}} V_{\text{hpcav}} / RT_{\text{hpcav},\text{min}}$. Similarly, during discharging, we obtain from eqs. (3.11) and (3.12)

$$\frac{p_{\text{hpcav}}(t)}{p_{\text{hpcav},\text{max}}} = \left(1 - \frac{\dot{m}_d t}{m_{\text{hpcav},\text{max}}}\right)^\gamma, \quad (3.43)$$

$$\frac{T_{\text{hpcav}}(t)}{T_{\text{hpcav},\text{max}}} = \left(1 - \frac{\dot{m}_d t}{m_{\text{hpcav},\text{max}}}\right)^{\gamma-1}, \quad (3.44)$$

where $m_{\text{hpcav},\text{max}} = p_{\text{hpcav},\text{max}} V_{\text{hpcav}} / RT_{\text{hpcav},\text{max}}$. The relationships between T_6 and the temperature extrema can be deduced from eqs. (3.14)

and (3.15) to be

$$\frac{T_6}{T_{\text{hpcav,max}}} = \frac{1 - \frac{p_{\text{hpcav,min}}}{p_{\text{hpcav,max}}}}{\gamma \left[1 - \left(\frac{p_{\text{hpcav,min}}}{p_{\text{hpcav,max}}} \right)^{\frac{1}{\gamma}} \right]}, \quad (3.45)$$

$$\frac{T_6}{T_{\text{hpcav,min}}} = \frac{T_6}{T_{\text{cav,max}}} \frac{T_{\text{hpcav,max}}}{T_{\text{hpcav,min}}} = \frac{\frac{p_{\text{hpcav,max}}}{p_{\text{hpcav,min}}} - 1}{\gamma \left[\left(\frac{p_{\text{hpcav,max}}}{p_{\text{hpcav,min}}} \right)^{\frac{1}{\gamma}} - 1 \right]}. \quad (3.46)$$

As for the one-stage model, these equations should be interpreted as determining $T_{\text{hpcav,max}}$ and $T_{\text{hpcav,min}}$ given $p_{\text{hpcav,max}}/p_{\text{hpcav,min}}$, γ , and T_6 . The latter must be supplied as an input parameter, chosen to satisfy $T_{\text{atm}} \leq T_6 \leq T_5(\Delta t_c)$.

Thanks to the constant pressure in the low-pressure cavern, the power consumed by the low-pressure compressor is

$$\dot{W}_{\text{lpc}} = \frac{\dot{m}_c C_p T_{\text{atm}}}{\eta_{s,\text{lpc}}} \left[\left(\frac{p_{\text{lpcav}}}{p_{\text{atm}}} \right)^{\frac{\gamma-1}{\gamma}} - 1 \right],$$

and hence the electrical energy consumed by the motor is

$$E_{\text{el,mot,lpc}} = \frac{\gamma}{\gamma-1} \frac{p_{\text{hpcav,max}} V_{\text{hpcav}}}{\eta_{\text{mot}} \eta_{m,\text{lpc}} \eta_{s,\text{lpc}}} \frac{T_{\text{atm}}}{T_{\text{hpcav,max}}} f_{\text{lpc}}, \quad (3.47)$$

where

$$f_{\text{lpc}} = \left[\left(\frac{p_{\text{lpcav}}}{p_{\text{atm}}} \right)^{\frac{\gamma-1}{\gamma}} - 1 \right] \left[1 - \left(\frac{p_{\text{hpcav,min}}}{p_{\text{hpcav,max}}} \right)^{\frac{1}{\gamma}} \right]. \quad (3.48)$$

Similarly, the power generated by the low-pressure turbine is

$$\dot{W}_{\text{lpt}} = \eta_{s,\text{lpt}} \dot{m}_d C_p T_9 \left[1 - \left(\frac{p_{\text{atm}}}{p_{\text{lpcav}}} \right)^{\frac{\gamma-1}{\gamma}} \right],$$

so the electrical energy produced by the generator is

$$E_{\text{el,gen,lpt}} = \frac{\gamma}{\gamma-1} \eta_{\text{gen}} \eta_{m,\text{lpt}} \eta_{s,\text{lpt}} p_{\text{hpcav,max}} V_{\text{hpcav}} \frac{T_9}{T_{\text{hpcav,max}}} f_{\text{lpt}}, \quad (3.49)$$

where

$$f_{\text{lpt}} = \left[1 - \left(\frac{p_{\text{atm}}}{p_{\text{lpcav}}} \right)^{\frac{\gamma-1}{\gamma}} \right] \left[1 - \left(\frac{p_{\text{hpcav,min}}}{p_{\text{hpcav,max}}} \right)^{\frac{1}{\gamma}} \right]. \quad (3.50)$$

The power consumed by the high-pressure compressor is

$$\dot{W}_{\text{hpc}}(t) = \frac{\dot{m}_c C_p T_3}{\eta_{s,\text{hpc}}} \left[\left(\frac{p_{\text{hpcav}}(t)}{p_{\text{lpcav}}} \right)^{\frac{\gamma-1}{\gamma}} - 1 \right]$$

and with eq. (3.41) and integrating in time, we obtain

$$E_{\text{el,mot,hpc}} = \frac{\gamma}{\gamma-1} \frac{p_{\text{hpcav,min}} V_{\text{hpcav}}}{\eta_{\text{mot}} \eta_{m,\text{hpc}} \eta_{s,\text{hpc}}} \frac{T_3}{T_6} f_{\text{hpc}}, \quad (3.51)$$

where

$$f_{\text{hpc}} = \frac{1}{2\gamma-1} \left(\frac{p_{\text{hpcav,min}}}{p_{\text{lpcav}}} \right)^{\frac{\gamma-1}{\gamma}} \left[\left(\frac{p_{\text{hpcav,max}}}{p_{\text{hpcav,min}}} \right)^{\frac{2\gamma-1}{\gamma}} - 1 \right] - \frac{1}{\gamma} \left(\frac{p_{\text{hpcav,max}}}{p_{\text{hpcav,min}}} - 1 \right), \quad (3.52)$$

which is seen to reduce to eq. (3.18) if $p_{\text{lpcav}}/p_{\text{atm}} = 1$ and the appropriate changes in notation are made.

The power produced by the high-pressure turbine is

$$\dot{W}_{\text{hpt}} = \eta_{s,\text{hpt}} \dot{m}_d C_p T_7(t) \left[1 - \left(\frac{p_{\text{lpcav}}}{p_{\text{hpcav}}(t)} \right)^{\frac{\gamma-1}{\gamma}} \right],$$

where $p_{\text{hpcav}}(t)$ is obtained from eq. (3.44). Following the reasoning outlined for the one-stage plant, we use eq. (3.40) to write

$$\int_0^{\Delta t_d} T_7(t) \left(\frac{p_{\text{lpcav}}}{p_{\text{hpcav}}(t)} \right)^{\frac{\gamma-1}{\gamma}} dt \approx \bar{T}_5^c \int_0^{\Delta t_d} \left(\frac{p_{\text{lpcav}}}{p_{\text{hpcav}}(t)} \right)^{\frac{\gamma-1}{\gamma}} dt. \quad (3.53)$$

With this approximation, we obtain

$$E_{\text{el,gen,hpt}} = \frac{\gamma}{\gamma-1} \eta_{\text{gen}} \eta_{m,\text{hpt}} \eta_{s,\text{hpt}} p_{\text{hpcav,max}} V_{\text{hpcav}} \frac{T_3}{T_{\text{hpcav,max}}} f_{\text{hpt}}, \quad (3.54)$$

where

$$f_{\text{hpt}} = \frac{\bar{T}_5^c}{T_3} \left\{ 1 - \left(\frac{p_{\text{hpcav,min}}}{p_{\text{hpcav,max}}} \right)^{\frac{1}{\gamma}} - \frac{1}{2-\gamma} \left(\frac{p_{\text{lpcav}}}{p_{\text{hpcav,max}}} \right)^{\frac{\gamma-1}{\gamma}} \left[1 - \left(\frac{p_{\text{hpcav,min}}}{p_{\text{hpcav,max}}} \right)^{\frac{2-\gamma}{\gamma}} \right] \right\}, \quad (3.55)$$

with \bar{T}_5^c/T_3 derived from

$$\frac{T_5(t)}{T_4} = 1 + \frac{1}{\eta_{s,\text{hpc}}} \left[\left(\frac{p_{\text{hpcav}}(t)}{p_{\text{lpcav}}} \right)^{\frac{\gamma-1}{\gamma}} - 1 \right] \quad (3.56)$$

and eqs. (3.6), (3.37), (3.41), and (3.46) as

$$\frac{\bar{T}_5^c}{T_3} = 1 + \frac{1}{\eta_{s,\text{hpc}}} \left(\frac{\gamma}{2\gamma-1} \left(\frac{p_{\text{hpcav},\text{min}}}{p_{\text{lpcav}}} \right)^{\frac{\gamma-1}{\gamma}} \frac{\left(\frac{p_{\text{hpcav},\text{max}}}{p_{\text{hpcav},\text{min}}} \right)^{\frac{2\gamma-1}{\gamma}} - 1}{\frac{p_{\text{hpcav},\text{max}}}{p_{\text{hpcav},\text{min}}} - 1} - 1 \right). \quad (3.57)$$

If $p_{\text{lpcav}}/p_{\text{atm}} = 1$, eq. (3.55) reduces to eq. (3.24) with the appropriate changes in notation. In section 3.3.8, the error induced by approximation (3.53) is analyzed. For values of $p_{\text{lpcav}}/p_{\text{atm}}$ between 5 and 20, the turbine work is underpredicted with a maximum relative error of 0.84%.

In the remainder of this section, quantitative results are presented for $p_{\text{atm}} = 1$ atm, $\eta_{\text{mot}} = \eta_{\text{gen}} = \eta_{m,\text{lpc}} = \eta_{m,\text{hpc}} = \eta_{m,\text{lpt}} = \eta_{m,\text{hpt}} = 0.98$ and $\gamma = 1.4$.

3.3.3 Plant efficiency

The plant efficiency is

$$\eta = \frac{E_{\text{el,gen}}}{E_{\text{el,mot}}} = \frac{E_{\text{el,gen,lpt}} + E_{\text{el,gen,hpt}}}{E_{\text{el,mot,lpc}} + E_{\text{el,mot,hpc}}}$$

and substituting from eqs. (3.47), (3.49), (3.51), and (3.54) gives

$$\eta = \eta_{\text{mot}}\eta_{\text{gen}} \frac{\frac{T_9}{T_{\text{hpcav,max}}} \eta_{m,\text{lpt}} \eta_{s,\text{lpt}} f_{\text{lpt}} + \frac{T_3}{T_{\text{hpcav,max}}} \eta_{m,\text{hpt}} \eta_{s,\text{hpt}} f_{\text{hpt}}}{\frac{T_{\text{atm}}}{T_{\text{hpcav,max}}} \frac{f_{\text{lpc}}}{\eta_{m,\text{lpc}} \eta_{s,\text{lpc}}} + \frac{T_3}{T_6} \frac{p_{\text{hpcav,min}}}{p_{\text{hpcav,max}}} \frac{f_{\text{hpc}}}{\eta_{m,\text{hpc}} \eta_{s,\text{hpc}}}}.$$

To simplify this expression, we write

$$\frac{T_9}{T_{\text{hpcav,max}}} = \frac{T_2}{T_{\text{atm}}} \frac{T_{\text{atm}}}{T_3} \frac{T_3}{T_6} \frac{T_6}{T_{\text{hpcav,max}}}, \quad (3.58)$$

$$\frac{T_3}{T_{\text{hpcav,max}}} = \frac{T_3}{T_6} \frac{T_6}{T_{\text{hpcav,max}}},$$

$$\frac{T_{\text{atm}}}{T_{\text{hpcav,max}}} = \frac{T_{\text{atm}}}{T_3} \frac{T_3}{T_6} \frac{T_6}{T_{\text{hpcav,max}}}, \quad (3.59)$$

where T_2/T_{atm} is given by eq. (3.35), T_3/T_{atm} and T_3/T_6 are regarded as parameters, $T_6/T_{\text{hpcav,max}}$ follows from eq. (3.45), and we assume

$$\eta_{m,\text{lpc}} = \eta_{m,\text{hpc}} = \eta_{m,\text{hpt}} = \eta_{m,\text{lpt}} = \eta_m,$$

resulting in

$$\eta = \eta_{\text{mot}} \eta_{\text{gen}} \eta_m^2 f_\eta, \quad (3.60)$$

where

$$f_\eta = \frac{\frac{T_2}{T_{\text{atm}}} \frac{T_{\text{atm}}}{T_3} \eta_{s,\text{lpt}} f_{\text{lpt}} + \eta_{s,\text{hpt}} f_{\text{hpt}}}{\frac{T_{\text{atm}}}{T_3} \frac{f_{\text{lpc}}}{\eta_{s,\text{lpc}}} + \frac{T_{\text{hpcav,max}}}{T_6} \frac{p_{\text{hpcav,min}}}{p_{\text{hpcav,max}}} \frac{f_{\text{hpc}}}{\eta_{s,\text{hpc}}}}. \quad (3.61)$$

Because $f_{\text{lpc}} = f_{\text{lpt}} = 0$ if $p_{\text{lpcav}}/p_{\text{atm}} = 1$, eq. (3.61) reduces to eq. (3.28) when the appropriate changes in notation are made.

Figure 3.11 presents f_η as a function of $p_{\text{hpcav,max}}/p_{\text{hpcav,min}}$ and $p_{\text{hpcav,max}}/p_{\text{atm}}$ for selected values of $p_{\text{lpcav}}/p_{\text{atm}}$ and for $\eta_{s,\text{lpc}} = \eta_{s,\text{hpc}} = \eta_{s,\text{hpt}} = \eta_{s,\text{lpt}} = 0.85$. In this and subsequent figures, the gray shading indicates the areas where the high-pressure compressor cannot operate because $p_{\text{hpcav,min}}/p_{\text{lpcav}} < 1$. The figure shows that $p_{\text{hpcav,max}}/p_{\text{hpcav,min}}$ and $p_{\text{hpcav,max}}/p_{\text{atm}}$ do not have a strong impact on f_η , which is consistent with $p_{\text{cav,max}}/p_{\text{cav,min}}$ and $p_{\text{cav,max}}/p_{\text{atm}}$ not having a strong impact for the one-stage plant.

By contrast, $p_{\text{lpcav}}/p_{\text{atm}}$ has a strong impact. For $p_{\text{lpcav}}/p_{\text{atm}} = 5$, the behavior of f_η is similar to that shown in fig. 3.3 for the one-stage plant, except that the maximum and minimum of f_η for the two-stage plant

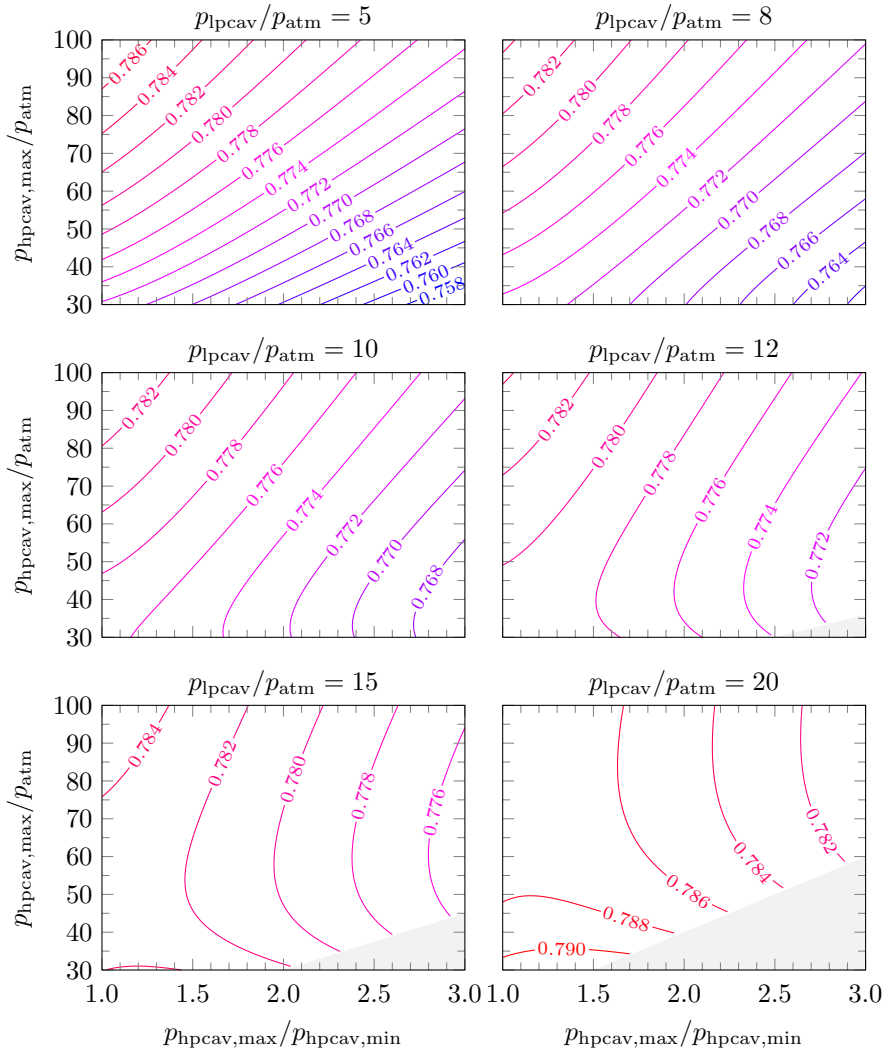


Figure 3.11: f_η given by eq. (3.61) as a function of $p_{\text{hpcav,max}}/p_{\text{hpcav,min}}$ and $p_{\text{hpcav,max}}/p_{\text{atm}}$ for selected values of $p_{\text{lpcav}}/p_{\text{atm}}$ and for $\eta_{s,\text{lpc}} = \eta_{s,\text{hpc}} = \eta_{s,\text{hpt}} = \eta_{s,\text{lpt}} = 0.85$, $T_3/T_{\text{atm}} = 1$, and $\gamma = 1.4$. Gray shading indicates areas where $p_{\text{hpcav,min}}/p_{\text{lpcav}} < 1$.

are lower by 0.028 and 0.031, respectively.⁷ As $p_{\text{lpcav}}/p_{\text{atm}}$ increases, two trends can be observed. The first is that f_η increases for large values of $p_{\text{hpcav,max}}/p_{\text{hpcav,min}}$ much more than for small values and that the influence of $p_{\text{hpcav,max}}/p_{\text{atm}}$ weakens. Therefore, the range of f_η diminishes from 0.755–0.788 for $p_{\text{lpcav}}/p_{\text{atm}} = 5$ to 0.780–0.792 for $p_{\text{lpcav}}/p_{\text{atm}} = 20$. The second trend concerns the behavior of the maximum of f_η . Its increase from 0.788 to 0.792 is seen to be non-monotonic: For the values of $p_{\text{lpcav}}/p_{\text{atm}}$ shown in fig. 3.11, the maximum of f_η has a minimum of 0.784 for $p_{\text{lpcav}}/p_{\text{atm}} = 10$.

The non-monotonic behavior of f_η can be shown more clearly by plotting it as a function of $p_{\text{lpcav}}/p_{\text{atm}}$ and $p_{\text{hpcav,max}}/p_{\text{atm}}$ for selected values of $p_{\text{hpcav,max}}/p_{\text{hpcav,min}}$, see fig. 3.12. The minimum exhibited by f_η occurs for values of $p_{\text{lpcav}}/p_{\text{atm}}$ between about 5–10 as $p_{\text{hpcav,max}}/p_{\text{atm}}$ grows from 30–100. Since f_η is nothing but the ratio of the turbine work to the compressor work, understanding the cause of the minimum requires investigating the extrema of the compressor and turbine work, which will be done in section 3.3.4.

By substituting $p_{\text{hpcav,max}}/p_{\text{hpcav,min}} = 1 + \varepsilon$ into eq. (3.61), taking the limit as $\varepsilon \rightarrow 0$, converting from isentropic to polytropic efficiencies, and setting $\eta_{\text{mot}} = \eta_{\text{gen}} = \eta_m = 1$, eq. (3.60) transforms to eq. (3.2). Our model therefore generalizes the two-stage plant model of Glendenning et al. [69]. As explained for the one-stage model, our model can be thought of as extending Glendenning et al.’s model from vanishing to finite values of $m_{\text{cd}}/V_{\text{hpcav}}$, and in the process allowing it to be used for more than simply estimating the plant efficiency.

⁷This does not mean that two-stage plants are inherently less efficient than one-stage plants. We assumed the isentropic turbomachinery efficiencies to be equal for both plants for simplicity. For the same maximum cavern pressure, the turbomachinery in an actual two-stage plant may attain higher efficiencies because it needs to deal with smaller pressure ranges in each stage.

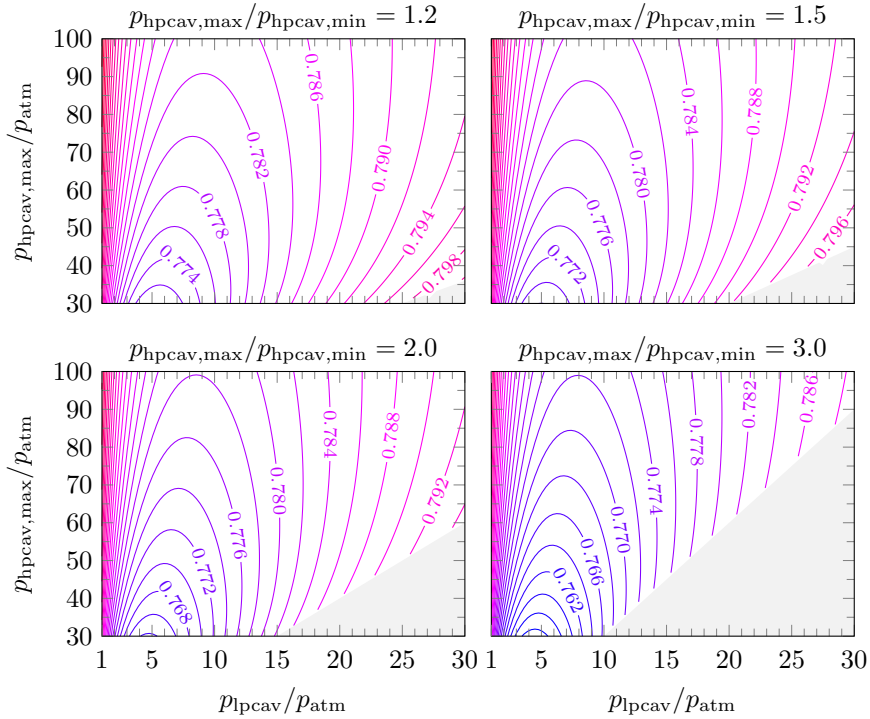


Figure 3.12: f_η given by eq. (3.61) as a function of p_{lpcav}/p_{atm} and $p_{hpcav,max}/p_{atm}$ for selected values of $p_{hpcav,max}/p_{hpcav,min}$ and for $\eta_{s,lpc} = \eta_{s,hpc} = \eta_{s,hpt} = \eta_{s,lpt} = 0.85$, $T_3/T_{atm} = 1$, and $\gamma = 1.4$. Gray shading indicates areas where $p_{hpcav,min}/p_{lpcav} < 1$.

3.3.4 Compressor and turbine work

The compressor work, determined from eqs. (3.47) and (3.51), is minimized for

$$\left(\frac{p_{\text{lpcav}}}{p_{\text{atm}}}\right)^{\frac{2(\gamma-1)}{\gamma}} = \frac{\frac{\gamma}{2\gamma-1} \frac{\eta_{s,\text{lpc}}}{\eta_{s,\text{hpc}}} \frac{T_3}{T_{\text{atm}}} \left(\frac{p_{\text{hpcav,max}}}{p_{\text{hpcav,min}}}\right)^{\frac{2\gamma-1}{\gamma}} - 1}{\left(\frac{p_{\text{hpcav,min}}}{p_{\text{atm}}}\right)^{-\frac{\gamma-1}{\gamma}} \frac{p_{\text{hpcav,max}}}{p_{\text{hpcav,min}}} - 1}. \quad (3.62)$$

In the limit of $p_{\text{hpcav,max}}/p_{\text{hpcav,min}} \rightarrow 1$, this simplifies to

$$\frac{p_{\text{lpcav}}}{p_{\text{atm}}} \approx \left(\frac{\eta_{s,\text{lpc}}}{\eta_{s,\text{hpc}}} \frac{T_3}{T_{\text{atm}}}\right)^{\frac{\gamma}{2(\gamma-1)}} \sqrt{\frac{p_{\text{hpcav}}}{p_{\text{atm}}}}, \quad (3.63)$$

whereas in the limit of $p_{\text{hpcav,max}}/p_{\text{hpcav,min}} \gg 1$, we obtain

$$\frac{p_{\text{lpcav}}}{p_{\text{atm}}} \approx \left(\frac{\gamma}{2\gamma-1} \frac{\eta_{s,\text{lpc}}}{\eta_{s,\text{hpc}}} \frac{T_3}{T_{\text{atm}}}\right)^{\frac{\gamma}{2(\gamma-1)}} \sqrt{\frac{p_{\text{hpcav,max}}}{p_{\text{atm}}}}. \quad (3.64)$$

These expressions are similar to the expression for the intermediate pressure ratio that minimizes the work of two-stage compression with a constant overall pressure ratio and intercooling. The similarity is not surprising since the low-pressure TES can be viewed as an intercooler at the intermediate pressure p_{lpcav} .

Alternatively, the low-pressure TES can be viewed as a reheater at the intermediate pressure. For two-stage expansion with reheat, constant inflow temperatures for both stages, and a constant overall pressure ratio, the turbine work exhibits a maximum at a specific intermediate pressure ratio. However, the turbine work derived from eqs. (3.49) and (3.54), instead of a

maximum, has a minimum for

$$\left(\frac{p_{\text{pcav}}}{p_{\text{atm}}}\right)^{\frac{2(\gamma-1)}{\gamma}} = \frac{\eta_{s,\text{lpt}} \left(\frac{1}{\eta_{s,\text{lpc}}} - 1 \right) + \frac{\frac{\gamma}{2\gamma-1} \frac{\eta_{s,\text{hpt}}}{\eta_{s,\text{hpc}}} \frac{T_3}{T_{\text{atm}}} \left(\frac{p_{\text{hpcav,max}}}{p_{\text{hpcav,min}}} \right)^{\frac{2\gamma-1}{\gamma}} - 1}{\left(\frac{p_{\text{hpcav,min}}}{p_{\text{atm}}} \right)^{-\frac{\gamma-1}{\gamma}} \frac{p_{\text{hpcav,max}}}{p_{\text{hpcav,min}}} - 1} \cdot \frac{\eta_{s,\text{lpt}} + \frac{\frac{\eta_{s,\text{hpt}}}{2-\gamma} \left(\frac{1}{\eta_{s,\text{hpc}}} - 1 \right) \frac{T_3}{T_{\text{atm}}} \left(\frac{p_{\text{hpcav,max}}}{p_{\text{hpcav,min}}} \right)^{\frac{2-\gamma}{\gamma}} - 1}{\left(\frac{p_{\text{hpcav,min}}}{p_{\text{atm}}} \right)^{\frac{\gamma-1}{\gamma}} \left(\frac{p_{\text{hpcav,max}}}{p_{\text{hpcav,min}}} \right)^{\frac{1}{\gamma}} - 1} \quad (3.65)$$

Since typical turbomachinery efficiencies are $O(1)$ and usually $p_{\text{hpcav,min}}/p_{\text{atm}} \gg 1$, the first term in the numerator of eq. (3.65) is negligible compared to the second term and the second term in the denominator is negligible compared to the first term, giving

$$\left(\frac{p_{\text{pcav}}}{p_{\text{atm}}}\right)^{\frac{2(\gamma-1)}{\gamma}} \approx \frac{\frac{\gamma}{2\gamma-1} \frac{\eta_{s,\text{lpc}}}{\eta_{s,\text{hpc}}} \frac{\eta_{s,\text{hpt}}}{\eta_{s,\text{lpt}}} \frac{T_3}{T_{\text{atm}}} \left(\frac{p_{\text{hpcav,max}}}{p_{\text{hpcav,min}}} \right)^{\frac{2\gamma-1}{\gamma}} - 1}{\left(\frac{p_{\text{hpcav,min}}}{p_{\text{atm}}} \right)^{-\frac{\gamma-1}{\gamma}} \frac{p_{\text{hpcav,max}}}{p_{\text{hpcav,min}}} - 1},$$

whose right-hand side differs from that of eq. (3.62) only through $\eta_{s,\text{hpt}}/\eta_{s,\text{lpt}}$. If $\eta_{s,\text{lpt}}/\eta_{s,\text{hpt}} = 1$ (as in figs. 3.11 and 3.12), it follows that the minima in the compressor and turbine work occur for nearly equal values of $p_{\text{pcav}}/p_{\text{atm}}$. That these nearly coincident minima cause a minimum in f_η indicates that the turbine work is more sensitive to $p_{\text{pcav}}/p_{\text{atm}}$.

Two points are worth noting. First, some authors tacitly assume that the optimal pressure for intercooling in a two-stage compression supplying an isochoric cavern, and therefore with a variable overall pressure ratio, is equal to the optimal pressure for intercooling in a two-stage compression

with a constant overall pressure ratio. For example, Osterle [78] assumed, in our notation,

$$\frac{p_{\text{lpcav}}}{p_{\text{atm}}} = \sqrt{\frac{p_{\text{hpcav,max}}}{p_{\text{atm}}}}. \quad (3.66)$$

Equation (3.62) shows that this assumption is in general incorrect. Comparison with approximation (3.63) indicates that the assumption is justified in the limit of $p_{\text{hpcav,max}}/p_{\text{hpcav,min}} \rightarrow 1$ if $\eta_{s,\text{lpc}}/\eta_{s,\text{hpc}} = T_3/T_{\text{atm}} = 1$. Conversely, comparison with approximation (3.64) reveals that in the limit of $p_{\text{hpcav,max}}/p_{\text{hpcav,min}} \gg 1$, even if $\eta_{s,\text{lpc}}/\eta_{s,\text{hpc}} = T_3/T_{\text{atm}} = 1$, the assumption leads to relative errors of

$$\left(\frac{\gamma}{2\gamma-1}\right)^{-\frac{\gamma}{2(\gamma-1)}} - 1 \approx 0.55 \quad \text{for } \gamma = 1.4.$$

Second, to the best of our knowledge, the existence of a minimum in the turbine work of a two-stage AA-CAES plant has not been reported in the literature. Haselbacher and Roos [74] show that if the turbine inflow temperatures T_7 and T_9 are constants, the turbine work has a maximum despite the falling pressure in the high-pressure cavern. The implication is that the minimum in the turbine work is caused by the turbine inflow temperatures depending on p_{lpcav} through the compressor outflow temperatures $T_2(t)$ and $T_5(t)$, see eqs. (3.35) and (3.56).

It seems unfortunate that choosing $p_{\text{lpcav}}/p_{\text{atm}}$ according to eq. (3.66) implies nearly minimal values of the plant efficiency because this choice has practical advantages: By equalizing the maximum pressure ratio of the high-pressure compressor and the pressure ratio of the low-pressure compressor, the maximum temperature of the air flowing into the high-pressure TES is equal to the temperature of the air flowing into the low-pressure TES, which simplifies the plant construction and thereby reduces its cost. The choice of $p_{\text{lpcav}}/p_{\text{atm}}$ must therefore balance the competing requirements of low cost and high efficiency.

3.3.5 Storage capacity and density

Assuming that $\eta_{m,\text{hpt}} = \eta_{m,\text{lpt}} = \eta_m$ and using eqs. (3.58) and (3.59), we obtain from eqs. (3.49) and (3.54) an expression for the non-dimensional storage capacity,

$$\frac{E_{\text{el,gen}}}{p_{\text{hpcav,max}} V_{\text{hpcav}}} = \frac{\gamma}{\gamma - 1} \eta_{\text{gen}} \eta_m \frac{T_3}{T_6} \frac{T_6}{T_{\text{hpcav,max}}} \left(\frac{T_2}{T_{\text{atm}}} \frac{T_{\text{atm}}}{T_3} \eta_{s,\text{lpt}} f_{\text{lpt}} + \eta_{s,\text{hpt}} f_{\text{hpt}} \right), \quad (3.67)$$

where $T_6/T_{\text{hpcav,max}}$ is given by eq. (3.45) and T_2/T_{atm} follows from eq. (3.35).

In fig. 3.13, the non-dimensional storage capacity is presented as a function of $p_{\text{hpcav,max}}/p_{\text{hpcav,min}}$ and $p_{\text{hpcav,max}}/p_{\text{atm}}$ for selected values of $p_{\text{lpcav}}/p_{\text{atm}}$. For these values, the maxima of the non-dimensional storage capacity are seen to range from about 2.37 to 2.57 compared to the maximum of 3.47 for the one-stage plant.

3.3.6 Cavern volumes

We can follow the approach presented for the one-stage plant to estimate the volume of the high-pressure cavern from eq. (3.67). For $E_{\text{el,gen}} = 10$ MWh, the resulting volumes are shown in fig. 3.14 as a function of $p_{\text{hpcav,max}}/p_{\text{hpcav,min}}$ for selected values of $p_{\text{hpcav,max}}/p_{\text{atm}}$ and $p_{\text{lpcav}}/p_{\text{atm}}$ for $T_3/T_6 = T_3/T_{\text{atm}} = 1$. The figure indicates that the volume of the high-pressure cavern does not depend strongly on $p_{\text{lpcav}}/p_{\text{atm}}$. Furthermore, comparison with fig. 3.7 shows that the two-stage plant requires larger caverns than the one-stage plant. Taking a specific example, for $p_{\text{lpcav}}/p_{\text{atm}} = 10$, $p_{\text{hpcav,max}}/p_{\text{atm}} = 100$, and $p_{\text{hpcav,max}}/p_{\text{hpcav,min}} = 1.4$, fig. 3.14 indicates that $V_{\text{hpcav}} \approx 3170 \text{ m}^3$. If 500 MWh of electrical energy are to be provided by the two-stage plant, a high-pressure cavern with a volume of $V_{\text{hpcav}} \approx 50 \cdot 3170 \text{ m}^3 \approx 158\,500 \text{ m}^3$ is thus required.

The volume of the low-pressure cavern can be estimated in the following manner. Since the pressure in the low-pressure cavern is constant and the

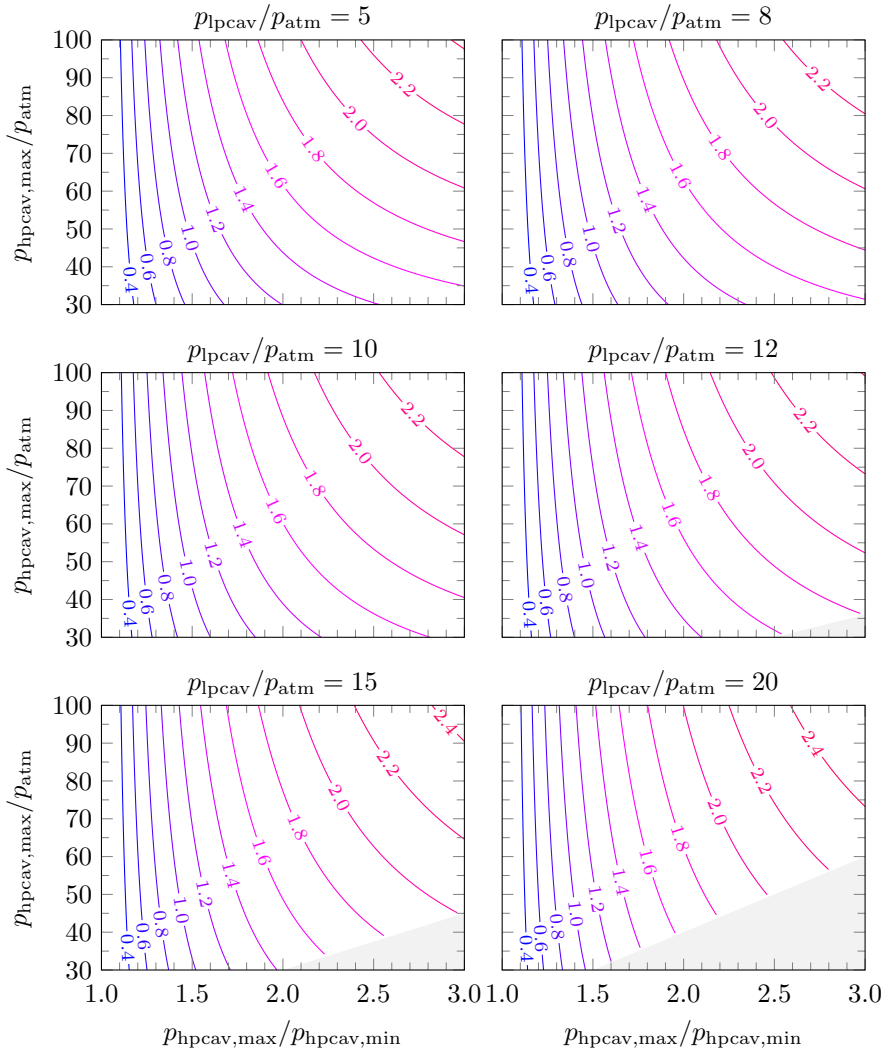


Figure 3.13: $E_{el,gen}/p_{hp,cav,max}V_{hp,cav}$ given by eq. (3.67) as a function of $p_{hp,cav,max}/p_{hp,cav,min}$ and $p_{hp,cav,max}/p_{atm}$ for selected values of $p_{lp,cav}/p_{atm}$ for $\eta_{s,lpc} = \eta_{s,hpc} = \eta_{s,hpt} = \eta_{s,lpt} = 0.85$, $\eta_{gen} = \eta_m = 0.98$, $T_3/T_6 = T_3/T_{atm} = 1$, and $\gamma = 1.4$. Gray shading indicates areas where $p_{hp,cav,min}/p_{lp,cav} < 1$.

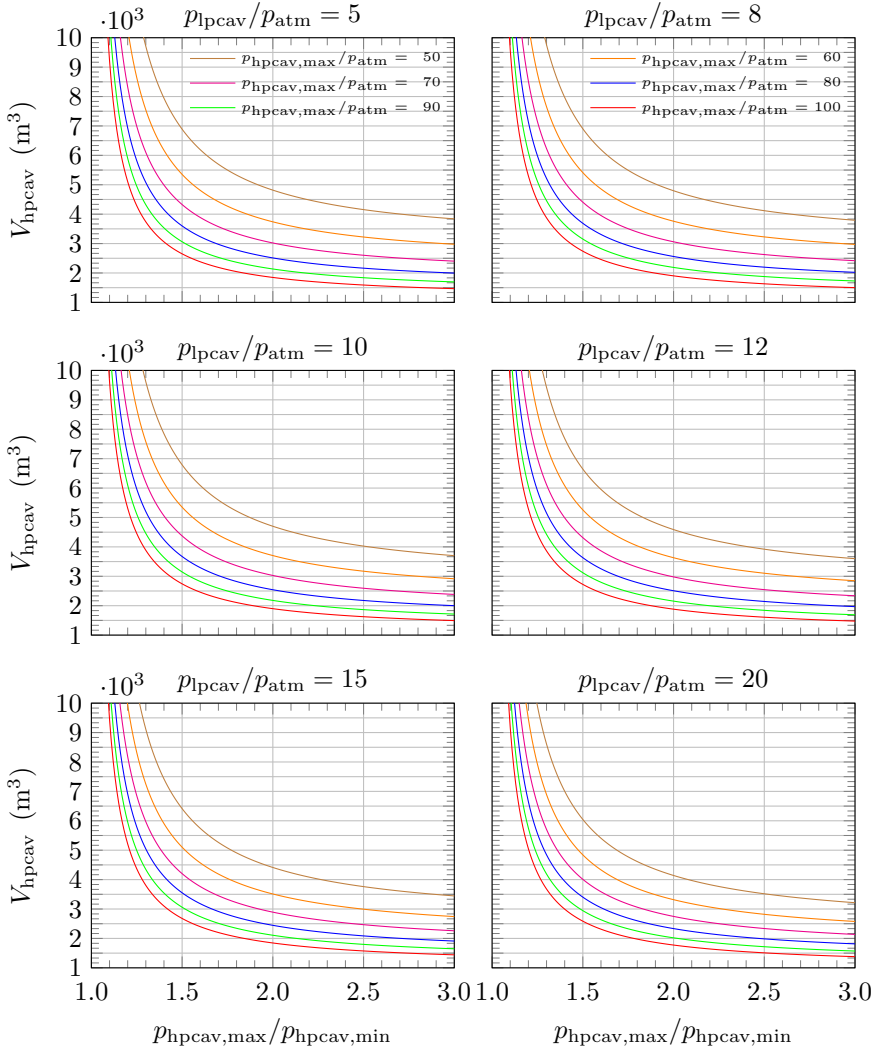


Figure 3.14: $V_{\text{hp cav}}$ required for $E_{\text{el,gen}} = 10$ MWh derived from eq. (3.67) as a function of $p_{\text{hp cav,max}}/p_{\text{hp cav,min}}$ and $p_{\text{hp cav,max}}/p_{\text{atm}}$ for $\eta_{s,\text{lpc}} = \eta_{s,\text{hpc}} = \eta_{s,\text{hpt}} = \eta_{s,\text{lpt}} = 0.85$, $\eta_{\text{gen}} = \eta_{\text{m}} = 0.98$, $T_3/T_6 = T_3/T_{\text{atm}} = 1$, and $\gamma = 1.4$.

mass flows in the low-pressure and high-pressure turbomachinery are equal, which implies that

$$\rho_{\text{Ipcav}} = \text{constant}, \quad (3.68)$$

it follows that the temperature in the low-pressure cavern must be constant, too. However, the temperature must also satisfy the energy equation, which during charging can be written as

$$\rho_{\text{Ipcav}} \frac{dT_{\text{Ipcav}}}{dt} = \frac{\gamma \dot{m}_c}{V_{\text{Ipcav}}} (T_3 - T_{\text{Ipcav}}(t)). \quad (3.69)$$

(During discharging, the heat exchanger ensures that the inflow temperature is also equal to T_3 , so the energy equation takes the same form except that \dot{m}_c is replaced by \dot{m}_d .) The energy equation integrates to

$$\frac{T_3 - T_{\text{Ipcav}}(t)}{T_3 - T_{\text{Ipcav,min}}} = \exp\left(-\frac{\gamma \dot{m}_c t}{\rho_{\text{Ipcav}} V_{\text{Ipcav}}}\right)$$

and therefore

$$\frac{T_{\text{Ipcav,max}}}{T_{\text{Ipcav,min}}} = \exp\left(-\frac{\gamma m_{cd}}{\rho_{\text{Ipcav}} V_{\text{Ipcav}}}\right) + \left[1 - \exp\left(-\frac{\gamma m_{cd}}{\rho_{\text{Ipcav}} V_{\text{Ipcav}}}\right)\right] \frac{T_3}{T_{\text{Ipcav,min}}}.$$

In other words, if

$$\exp\left(-\frac{\gamma m_{cd}}{\rho_{\text{Ipcav}} V_{\text{Ipcav}}}\right) \approx 0, \quad (3.70)$$

the temperature in the low-pressure cavern is constant and equal to T_3 , which justifies eqs. (3.36) and (3.37) and shows that

$$p_{\text{Ipcav}} = \rho_{\text{Ipcav}} R T_3.$$

Note that eq. (3.70) implies that the mass flowing through the cavern during charging and discharging is much greater than the mass in the cavern, indicating that the low-pressure cavern should be small. An upper limit on the volume of the low-pressure cavern can be determined from eq. (3.70). If we require that

$$\exp\left(-\frac{\gamma m_{cd}}{\rho_{\text{Ipcav}} V_{\text{Ipcav}}}\right) \leq 10^{-6}, \quad (3.71)$$

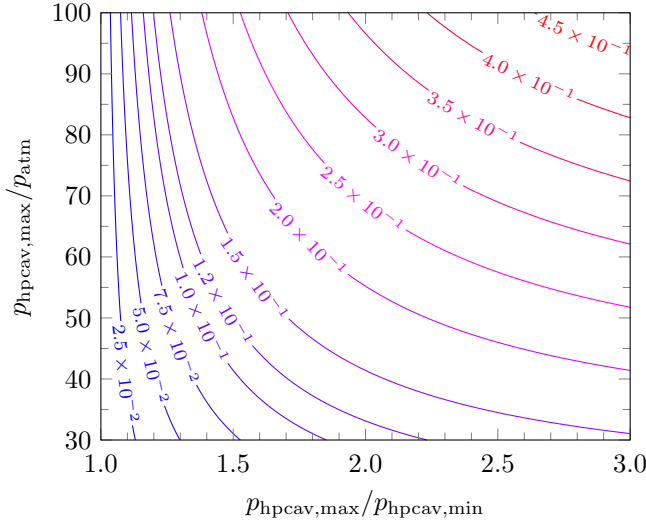


Figure 3.15: Upper limit on V_{1pcav}/V_{hpcav} given by eq. (3.74) that ensures inequality (3.71) as a function of $p_{hpcav,max}/p_{hpcav,min}$ and $p_{hpcav,max}/p_{atm}$ for $p_{1pcav}/p_{atm} = 10$ and $T_6/T_3 = 1$.

then

$$V_{1pcav} \leq \frac{\gamma m_{cd}}{13.8 \rho_{1pcav}}. \quad (3.72)$$

Since $m_{cd} = m_{hpcav,max} - m_{hpcav,min}$, the ideal-gas law and eq. (3.45) give

$$m_{cd} = \frac{p_{hpcav,max} V_{hpcav}}{(\gamma - 1) C_p T_6} \left(1 - \frac{p_{hpcav,min}}{p_{hpcav,max}} \right), \quad (3.73)$$

which, on substituting into inequality (3.72) and using the ideal-gas law once more with eq. (3.36), results in

$$\frac{V_{1pcav}}{V_{hpcav}} \leq \frac{1}{13.8} \frac{p_{hpcav,max}}{p_{atm}} \frac{p_{atm}}{p_{1pcav}} \frac{T_3}{T_6} \left(1 - \frac{p_{hpcav,min}}{p_{hpcav,max}} \right). \quad (3.74)$$

Figure 3.15 presents this upper limit on V_{1pcav}/V_{hpcav} as a function of $p_{cav,max}/p_{cav,min}$ and $p_{cav,max}/p_{atm}$ for $p_{1pcav}/p_{atm} = 10$ and $T_3/T_6 = 1$.

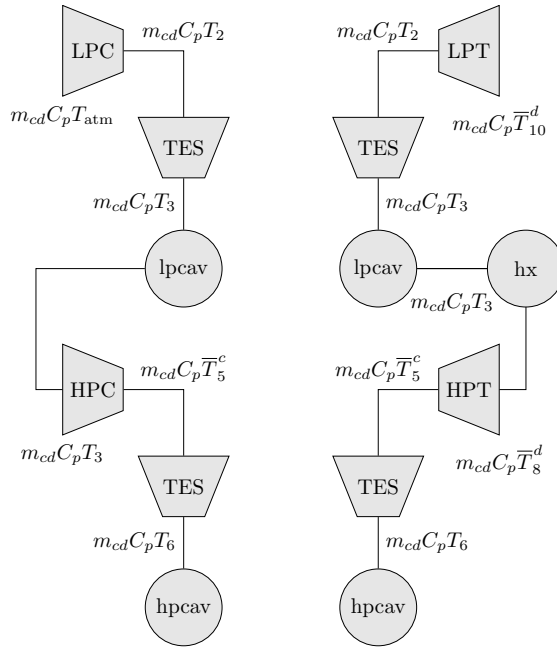


Figure 3.16: Enthalpy flows during the charging phase (left) and discharging phase (right).

3.3.7 Energy breakdown

With the previously defined temperatures, we can determine the energy flows in the plant during the charging and discharging phases, see fig. 3.16, and thus break down how much energy is stored in the two TES and the high-pressure cavern.

During the charging phase, the enthalpy that flows into the low-pressure cavern, plus the work done by the low- and high-pressure compressors must equal the thermal energies extracted by the low- and high-pressure

TES plus the enthalpy flowing into the high-pressure cavern,

$$\begin{aligned} & m_{cd}H_{\text{lpc},\text{in}} + m_{cd}(H_{\text{lpc},\text{out}} - H_{\text{lpc},\text{in}}) + m_{cd}(H_{\text{hpc},\text{out}} - H_{\text{hpc},\text{in}}) \\ &= m_{cd}(H_{\text{lptes},\text{in}} - H_{\text{lptes},\text{out}}) + m_{cd}(H_{\text{hptes},\text{in}} - H_{\text{hptes},\text{out}}) + m_{cd}H_{\text{hpcav},\text{in}}, \end{aligned}$$

where it should be noted that the low-pressure cavern does not appear because we assume the inflow and outflow temperatures to be equal, see eq. (3.36). Thus we can write

$$g_{\text{hpcav}} + g_{\text{hptes}} + g_{\text{lptes}} = 1,$$

where

$$g_{\text{hpcav}} = \frac{H_{\text{hpcav},\text{in}}}{H_{\text{lpc},\text{out}} + (H_{\text{hpc},\text{out}} - H_{\text{hpc},\text{in}})} = \frac{\frac{T_6}{T_3}}{\frac{T_2}{T_{\text{atm}}} \frac{T_{\text{atm}}}{T_3} + \frac{\bar{T}_5^c}{T_3} - 1}, \quad (3.75)$$

$$g_{\text{hptes}} = \frac{H_{\text{hptes},\text{in}} - H_{\text{hptes},\text{out}}}{H_{\text{lpc},\text{out}} + (H_{\text{hpc},\text{out}} - H_{\text{hpc},\text{in}})} = \frac{\frac{\bar{T}_5^c}{T_3} - \frac{T_6}{T_3}}{\frac{T_2}{T_{\text{atm}}} \frac{T_{\text{atm}}}{T_3} + \frac{\bar{T}_5^c}{T_3} - 1}, \quad (3.76)$$

and

$$g_{\text{lptes}} = \frac{H_{\text{lptes},\text{in}} - H_{\text{lptes},\text{out}}}{H_{\text{lpc},\text{out}} + (H_{\text{hpc},\text{out}} - H_{\text{hpc},\text{in}})} = \frac{\frac{T_2}{T_{\text{atm}}} \frac{T_{\text{atm}}}{T_3} - 1}{\frac{T_2}{T_{\text{atm}}} \frac{T_{\text{atm}}}{T_3} + \frac{\bar{T}_5^c}{T_3} - 1}. \quad (3.77)$$

Figure 3.17 presents g_{hpcav} , g_{hptes} , and g_{lptes} as a function of $p_{\text{hpcav},\text{max}}/p_{\text{hpcav},\text{min}}$ and $p_{\text{hpcav},\text{max}}/p_{\text{atm}}$ for $p_{\text{lpcav}}/p_{\text{atm}} = 10$ and $T_3/T_{\text{atm}} = T_3/T_6 = 1$. We observe that for $p_{\text{hpcav},\text{max}}/p_{\text{hpcav},\text{min}} = 1.4$ and $p_{\text{hpcav},\text{max}}/p_{\text{atm}} = 100$, the high-pressure cavern and the two TES each store about one-third of the supplied energy.

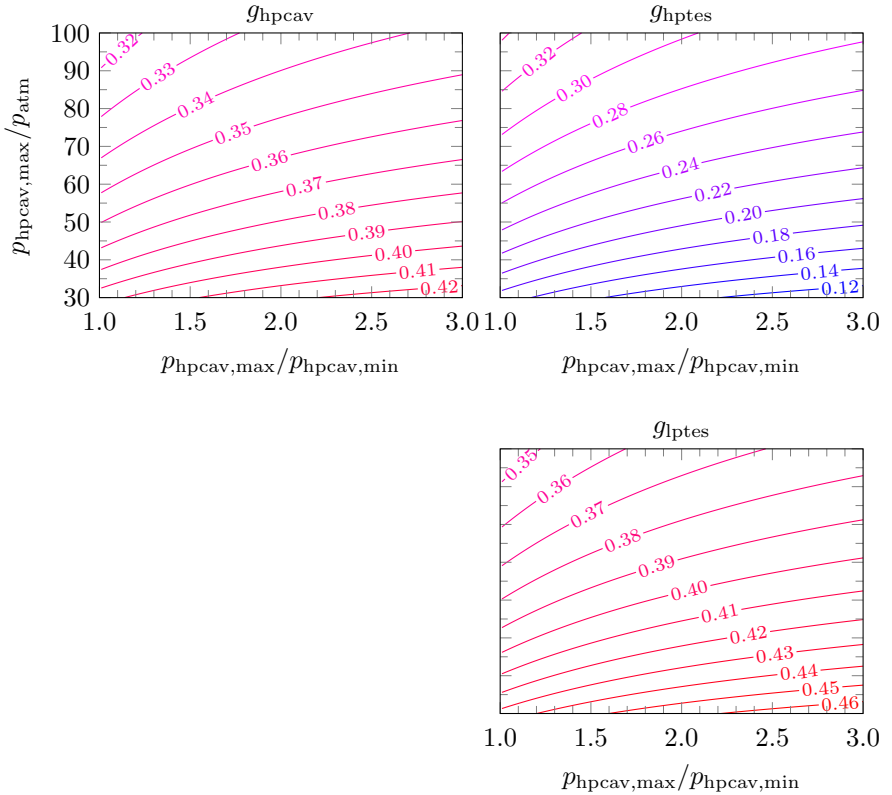


Figure 3.17: The fractions of energy stored in the high-pressure cavern, the high-pressure TES, and the low-pressure TES, given by eqs. (3.75) to (3.77), as a function of $p_{\text{hpcav,max}}/p_{\text{atm}}$ and $p_{\text{hpcav,max}}/p_{\text{hpcav,min}}$ for $\eta_{s,\text{lpc}} = \eta_{s,\text{hpc}} = 0.85$, $p_{\text{lpcav}}/p_{\text{atm}} = 10$, $T_3/T_{\text{atm}} = T_6/T_3 = 1$, and $\gamma = 1.4$.

Conversely, during discharging, we have

$$\begin{aligned}
 m_{cd}(H_{\text{hpt},\text{in}} - H_{\text{hpt},\text{out}}) + m_{cd}(H_{\text{lpt},\text{in}} - H_{\text{lpt},\text{out}}) \\
 + m_{cd}H_{\text{lpt},\text{out}} + m_{cd}(H_{\text{hx},\text{in}} - H_{\text{hx},\text{out}}) \\
 = m_{cd}H_{\text{hpcav},\text{out}} + m_{cd}(H_{\text{hptes},\text{out}} - H_{\text{hptes},\text{in}}) \\
 + m_{cd}(H_{\text{lptes},\text{out}} - H_{\text{lptes},\text{in}}),
 \end{aligned}$$

where it should be noted that the low-pressure cavern does not appear because the heat exchanger ensures that the inflow and outflow temperatures are equal. Thus we can write

$$g_{\text{lptes}} + g_{\text{hptes}} + g_{\text{hpcav}} - g_{\text{hx}} = 1,$$

where

$$g_{\text{lptes}} = \frac{H_{\text{lptes},\text{out}} - H_{\text{lptes},\text{in}}}{(H_{\text{hpt},\text{in}} - H_{\text{hpt},\text{out}}) + H_{\text{lpt},\text{in}}} = \frac{\frac{T_2}{T_{\text{atm}}} \frac{T_{\text{atm}}}{T_3} - 1}{\frac{\bar{T}_5^c}{T_3} \left(1 - \frac{\bar{T}_8^d}{\bar{T}_5^c}\right) + \frac{T_2}{T_{\text{atm}}} \frac{T_{\text{atm}}}{T_3}}, \quad (3.78)$$

$$g_{\text{hptes}} = \frac{H_{\text{hptes},\text{out}} - H_{\text{hptes},\text{in}}}{(H_{\text{hpt},\text{in}} - H_{\text{hpt},\text{out}}) + H_{\text{lpt},\text{in}}} = \frac{\frac{\bar{T}_5^c}{T_3} - \frac{T_6}{T_3}}{\frac{\bar{T}_5^c}{T_3} \left(1 - \frac{\bar{T}_8^d}{\bar{T}_5^c}\right) + \frac{T_2}{T_{\text{atm}}} \frac{T_{\text{atm}}}{T_3}}, \quad (3.79)$$

$$g_{\text{hpcav}} = \frac{H_{\text{hpcav},\text{out}}}{(H_{\text{hpt},\text{in}} - H_{\text{hpt},\text{out}}) + H_{\text{lpt},\text{in}}} = \frac{\frac{T_6}{T_3}}{\frac{\bar{T}_5^c}{T_3} \left(1 - \frac{\bar{T}_8^d}{\bar{T}_5^c}\right) + \frac{T_2}{T_{\text{atm}}} \frac{T_{\text{atm}}}{T_3}}, \quad (3.80)$$

and

$$g_{\text{hx}} = \frac{H_{\text{hx},\text{in}} - H_{\text{hx},\text{out}}}{(H_{\text{hpt},\text{in}} - H_{\text{hpt},\text{out}}) + H_{\text{lpt},\text{in}}} = \frac{\frac{\bar{T}_8^d}{\bar{T}_5^c} \frac{T_5^c}{T_3}}{\frac{\bar{T}_5^c}{T_3} \left(1 - \frac{\bar{T}_8^d}{\bar{T}_5^c}\right) + \frac{T_2}{T_{\text{atm}}} \frac{T_{\text{atm}}}{T_3}}. \quad (3.81)$$

An equation for $\overline{T}_8^d/\overline{T}_5^c$ can be derived by noting that the left-hand side of approximation (3.53) is nothing but \overline{T}_{8s}^d . Therefore,

$$\frac{\overline{T}_{8s}^d}{\overline{T}_5^c} = 1 - \frac{W_{\text{hpt}}}{\eta_{s,\text{hpt}} m_{cd} C_p \overline{T}_5^c} = 1 - \frac{E_{\text{el,gen,hpt}}}{\eta_{\text{gen}} \eta_{m,\text{hpt}} \eta_{s,\text{hpt}} m_{cd} C_p \overline{T}_5^c},$$

and substituting for $E_{\text{el,gen,hpt}}$ from eq. (3.54), writing $m_{cd} = m_{\text{hpcav,max}} - m_{\text{hpcav,min}}$, and using the ideal-gas law gives

$$\frac{\overline{T}_{8s}^d}{\overline{T}_5^c} = 1 - \frac{T_3}{\overline{T}_5^c} \left[1 - \left(\frac{p_{\text{hpcav,min}}}{p_{\text{hpcav,max}}} \right)^{\frac{1}{\gamma}} \right]^{-1} f_{\text{hpt}}.$$

Now the definition of the isentropic efficiency of the high-pressure turbine, becomes, by integrating in time and putting $\overline{T}_7^d = \overline{T}_5^c$ thanks to eq. (3.40),

$$\frac{\overline{T}_{8s}^d}{\overline{T}_5^c} = 1 - \frac{1}{\eta_{s,\text{hpt}}} \left(1 - \frac{\overline{T}_8^d}{\overline{T}_5^c} \right),$$

and combining with two expressions and substituting for f_{hpt} from eq. (3.55) gives

$$\frac{\overline{T}_8^d}{\overline{T}_5^c} = (1 - \eta_{s,\text{hpt}}) + \frac{\eta_{s,\text{hpt}}}{2 - \gamma} \left(\frac{p_{\text{lpcav}}}{p_{\text{hpcav,max}}} \right)^{\frac{\gamma-1}{\gamma}} \frac{1 - \left(\frac{p_{\text{hpcav,min}}}{p_{\text{hpcav,max}}} \right)^{\frac{2-\gamma}{\gamma}}}{1 - \left(\frac{p_{\text{hpcav,min}}}{p_{\text{hpcav,max}}} \right)^{\frac{1}{\gamma}}}.$$

Figure 3.18 presents g_{hpcav} , g_{hptes} , g_{lptes} , and g_{hx} as a function of $p_{\text{hpcav,max}}/p_{\text{hpcav,min}}$ and $p_{\text{hpcav,max}}/p_{\text{atm}}$ for $p_{\text{lpcav}}/p_{\text{atm}} = 10$ and $T_3/T_{\text{atm}} = T_3/T_6 = 1$. We observe that for $p_{\text{hpcav,max}}/p_{\text{hpcav,min}} = 1.4$ and $p_{\text{hpcav,max}}/p_{\text{atm}} = 100$, the high-pressure cavern and the two TES each supply a little more than about one-third and that the heat exchanger rejects approximately 8% of the extracted energy.

3.3.8 Discussion

To quantify the impact of the approximation (3.53), we compare the turbine work obtained with it to that obtained with

$$T_7(t) = T_5(\Delta t_c - rt), \quad (3.82)$$

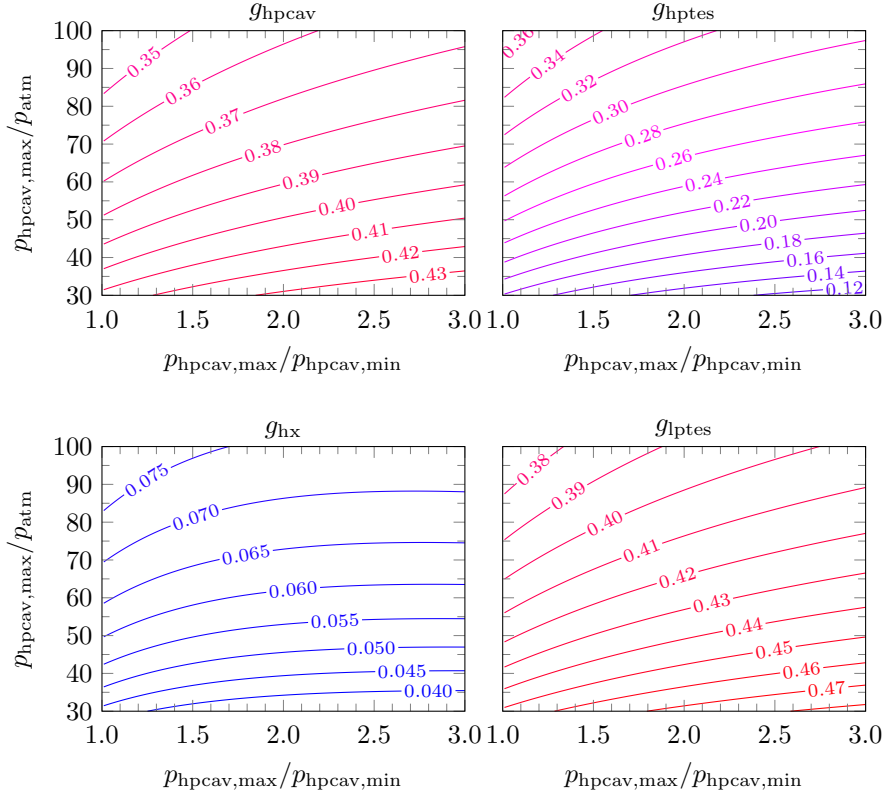


Figure 3.18: The fractions of energy stored in the high-pressure cavern, the high-pressure TES, and the low-pressure TES and the fraction of energy rejected by the heat exchanger, given by eqs. (3.78) to (3.81), as a function of $p_{\text{hpcav,max}}/p_{\text{atm}}$ and $p_{\text{hpcav,max}}/p_{\text{hpcav,min}}$ for $\eta_{s,\text{lpc}} = \eta_{s,\text{hpc}} = \eta_{s,\text{hpt}} = 0.85$, $p_{\text{lpcav}}/p_{\text{atm}} = 10$, $T_3/T_{\text{atm}} = T_6/T_3 = 1$, and $\gamma = 1.4$.

which can be viewed as the result of a high-pressure TES whose outflow temperature during discharging mirrors the inflow temperature during charging. Substituting for $T_5(t)/T_4$ from eq. (3.56), using eq. (3.37), and substituting for $p_{\text{hpcav}}(t)/p_{\text{lpcav}}$ from eq. (3.43) results in eq. (3.54) except that f_{hpt} is replaced by

$$f_{\text{hpt},e} = \frac{\bar{T}_5^c}{T_3} \left[1 - \left(\frac{p_{\text{hpcav},\text{min}}}{p_{\text{hpcav},\text{max}}} \right)^{\frac{1}{\gamma}} \right] \left[1 - \frac{T_3}{\bar{T}_5^c} \left(\frac{p_{\text{lpcav}}}{p_{\text{hpcav},\text{max}}} \right)^{\frac{\gamma-1}{\gamma}} I \right],$$

where the subscript e once again indicates that we regard this as an exact result and where

$$I = \int_0^1 \left(1 + \frac{1}{\eta_{s,\text{hpc}}} \left\{ \left[\frac{p_{\text{hpcav},\text{min}}}{p_{\text{lpcav}}} \left(1 + \gamma \frac{m_{cd}(1-\xi)}{m_{\text{hpcav},\text{min}}} \frac{T_6}{T_{\text{hpcav},\text{min}}} \right) \right]^{\frac{\gamma-1}{\gamma}} - 1 \right\} \right) \left(1 - \frac{m_{cd}\xi}{m_{\text{hpcav},\text{max}}} \right)^{-(\gamma-1)} d\xi. \quad (3.83)$$

The error in the turbine work incurred by the approximation is

$$\varepsilon = \frac{W_{\text{lpt}} + W_{\text{hpt}}}{W_{\text{lpt}} + W_{\text{hpt},e}} - 1 = \frac{1 + \frac{T_3}{T_{\text{atm}}} \frac{T_{\text{atm}}}{T_2} \frac{\eta_{s,\text{hpt}}}{\eta_{s,\text{lpt}}} \frac{f_{\text{hpt}}}{f_{\text{lpt}}}}{1 + \frac{T_3}{T_{\text{atm}}} \frac{T_{\text{atm}}}{T_2} \frac{\eta_{s,\text{hpt}}}{\eta_{s,\text{lpt}}} \frac{f_{\text{hpt},e}}{f_{\text{lpt}}}} - 1, \quad (3.84)$$

which is plotted in fig. 3.19 for $\eta_{s,\text{hpt}} = \eta_{s,\text{lpt}}$ and $T_3/T_{\text{atm}} = 1$. The maximum absolute value of the relative errors is 0.84%.

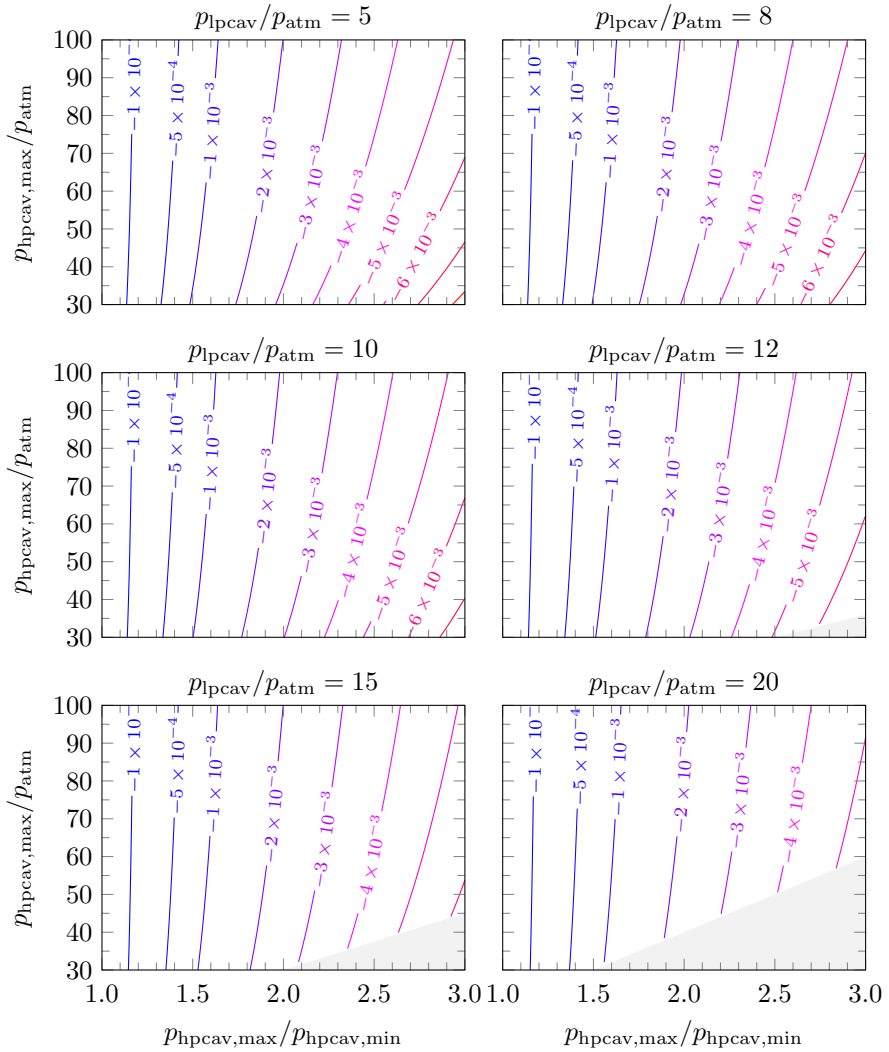


Figure 3.19: The relative error in the total turbine work defined by eq. (3.84) as a function of $p_{\text{hpcav,max}}/p_{\text{hpcav,min}}$, $p_{\text{hpcav,max}}/p_{\text{atm}}$, and $p_{\text{lpcav}}/p_{\text{atm}}$ for $\eta_{s,\text{hpc}} = \eta_{s,\text{lpc}} = 0.85$, $\eta_{s,\text{hpt}} = \eta_{s,\text{lpt}}$, $T_3/T_{\text{atm}} = 1$, and $\gamma = 1.4$. Note the unequal spacing of the isolines below $1 \cdot 10^{-3}$.

3.4 Summary, conclusions, and future work

We have presented simple analytical models of one- and two-stage AA-CAES plants with isochoric caverns that provide closed-form expressions for key performance indicators such as the efficiency and volumetric energy density in terms of component efficiencies and pressure ratios. The models can be used for the initial design of such plants by determining the pressure ratios and cavern volume(s) required to attain a given plant efficiency and storage capacity.

The models were derived subject to a number of simplifying assumptions, chief among which are that the air can be treated as an ideal gas, that caverns are adiabatic, and that TES units are free of thermal and pressure losses. In addition, to arrive at a simple model, it was necessary to approximate integrals involving simultaneous temporal variations of temperature and pressure. The magnitude of the relative error incurred by the approximation was shown to be smaller than 1%, making the models more than accurate enough for the initial design of AA-CAES plants. The approximation is critical for the derivation of a plant model and may explain why previous authors, such as Glendenning [39] and Glendenning et al. [69], elected to assume constant pressures in the caverns, which precludes their models from being used to estimate cavern volume(s). Our model avoids such drastic simplifications and was shown to reduce to the models of Glendenning and Glendenning et al. in the limit of vanishing pressure variations in the cavern(s).

By virtue of being analytical rather than numerical, our models cannot only be used for the initial design of AA-CAES plants, but also generate physical insights. For example, the model for the one-stage plant showed that the ratio of maximum to minimum pressures in the cavern has a small effect on the plant efficiency, but a large effect on the volumetric energy density. The model also showed that because the charging of the cavern is non-isentropic, AA-CAES plants cannot attain 100% efficiency. The impact of the non-isentropic charging of the cavern is much smaller than

the impact of inefficiencies in the turbomachinery, however. Similar insights were extracted from the model for two-stage plants, the most important of which is that the plant efficiency exhibits a minimum for specific values of the ratio of the pressure in the low-pressure cavern to the atmospheric pressure. The minimum was shown to be caused by a minimum in the turbine work, in contrast to two-stage expansion with constant inflow temperature and overall pressure ratio, for which the turbine work exhibits a maximum. The minimum in the plant efficiency occurs for values of the ratio of the pressure in the low-pressure cavern to the atmospheric pressure that, under certain limiting assumptions, are proportional to the square root of the ratio of the maximum pressure in the high-pressure cavern to the atmospheric pressure. This result seems unfortunate because the plant efficiency exhibits a minimum for those values of the pressure in the low-pressure cavern that equalizes the work of the low-pressure compressor and the maximum work of the high-pressure compressor, which simplifies the plant construction and therefore reduces the plant cost. The design of two-stage plants must therefore weigh the competing requirements of low cost and high efficiency.

Our models could be extended in several ways. Real-gas effects, which were shown by Kushnir et al. [77] to have non-negligible impacts on the pressure and temperature extrema in a cavern, could be included through appropriately chosen equations of state. The inclusion of thermal losses from TES units is more challenging. The simple treatment of Frutschi [40] is hardly satisfactory, but a more faithful representation of the thermal losses would introduce a significant number of additional parameters, such as the diameter and height of the TES units as well as the thicknesses and thermophysical properties of the structural and insulation layers. Modeling the caverns as diabatic would allow our models to take into account the cavern geometry as well as the duration of idle phases. Simple models of the heat-transfer between the air and the cavern wall, such as that proposed by Zaugg [71], could be based on a constant heat-transfer coefficient and constant temperatures of the cavern wall. More comprehensive models that take into account the heat-transfer in the material surrounding the cavern,

like that presented by Kushnir et al. [80], are already too complex for the purpose of our model and are best included in numerical plant models.

NUMERICAL INVESTIGATION OF AA-CAES PLANT DESIGN ^{1,2}

4.1 Introduction

Large-scale electricity storage enables high shares of renewable electricity generation through its ability to balance the supply of intermittent renewable energy sources with electricity demand [7]. Worldwide, pumped hydro electricity storage (PHS) is by far the most mature and most widely used large-scale storage technology, amounting to over 98% of storage systems with power ratings over 10 MW [9]. At the same time, further expansion of PHS is often limited due to the high capital costs, and environmental concerns. A potential alternative to PHS is advanced adiabatic compressed

¹Material in this chapter is taken from P. Roos, P. Gassmann, A. Haselbacher, “Numerical investigation of AA-CAES plant design”, to be submitted for publication, 2021.

²Material in this chapter has been extracted from P. Gassmann, “Development of an automated AA-CAES plant design tool based on numerical optimization”, Master Thesis, ETH Zurich, 2020, performed under the supervision of the author.

air energy storage (AA-CAES), offering similar power and capacity ratings, and storage efficiencies that are projected to reach 60 – 75%, see Budt et al. [16], and Sciacovelli et al. [17].

The working principle of compressed air energy storage (CAES) is based on a separated gas turbine cycle. By disconnecting the compression and expansion stages, electricity can be stored by compressing air into a storage volume, and electricity can be generated by emptying the storage volume at a later point in time and expanding the compressed air in the turbine. CAES can be classified by the idealized thermodynamic paths that are followed during the compression and expansion into diabatic (D-CAES), adiabatic (AA-CAES), and isothermal (I-CAES). In D-CAES, the compression heat is rejected to the ambient during the charging process, leaving ambient temperature air flowing into the storage volume. During discharging, the air from the storage volume is re-heated by burning fossil fuels before entering the turbine. AA-CAES captures the compression heat in a thermal-energy storage (TES) during charging, and the air is re-heated by the TES during discharging before expansion, eliminating the need to burn fossil fuels. I-CAES is based on isothermal compression and expansion, which requires heat removal during the compression. An extensive review of the three concepts is given by Budt et al. [16], where not just the theoretical background, but also current and past projects are presented. We refrain from giving a detailed review of D-CAES and I-CAES, as our focus lies on AA-CAES.

The first noteworthy research projects on CAES were conducted in the '70s and '80s, culminating in the realization of the only two commercial CAES plant projects to date, namely Huntorf, a D-CAES plant located in Germany and commissioned in 1978, and McIntosh, a D-CAES plant located in Alabama (USA) and commissioned in 1991, see Crotogino et al. [15] and Budt et al. [16], both using salt caverns as air storage volumes.

Renewed interest in CAES technology appeared in the early 2000's, when electricity storage technologies became more relevant due to increased renewable, intermittent electricity generation and the question of how to integrate these intermittent sources into the existing energy infrastructure.

For AA-CAES, so far only pilot-scale projects have been realized. Wang et al. [36] presented experiments with an AA-CAES pilot plant using steel tanks to store the compressed air and using water as heat-transfer fluid (HTF) and storage material for the TES, resulting in round-trip efficiencies of 22.6%. Geissbühler et al. [19] and Becattini et al. [20] presented experimental results from a pilot plant with a hard-rock cavern that included sensible and latent TES units placed inside the cavern. In their experiments, pressurized air of up to 550 °C entered the TES and was cooled down before flowing into the cavern for charging. During discharging, the air from the cavern was reheated in the TES before flowing out of the cavern. Using the energy balance from the experiments and estimated compressor and turbine performance, plant efficiencies were estimated to be 63 – 74%.

The limited number of pilot-plant projects, most likely due to their already considerable scale and associated costs, forces most studies to rely on numerical plant models. Such models are based on numerical integration of the governing equations for the various components, for example the energy and mass balance equations for the cavern, or the energy equations for adiabatic compression and expansion for the turbomachinery. The main advantage of the numerical modeling approach is that it can easily be modified to include more complexity, such as real-gas models, variable operating conditions, and efficiency maps, making the results more realistic and comparable to real-world applications.

Using these varying degrees of complexity, research projects about AA-CAES using numerical models can be categorized by identifying their scope. With varying complexity and extent, there are (1) plant models, concentrating technical aspects such as layout and performance analyses, and (2) plant-integration models, where techno-economic assessments of AA-CAES plants integrated into electricity grids dominate.

Numerical plant models falling into category (1) have been presented by several authors. Hartmann et al. [34] calculated the efficiencies of several AA-CAES plant layouts using the polytropic efficiency of the turbomachines and concluded that a realistic estimation for the efficiency of a two-stage

compression and one stage expansion AA-CAES plant lies between 49% to 61%. Barbour et al. [35] presented a numerical model for AA-CAES including direct heat-exchange packed bed TES. Their analysis considered steady cycling with constant mass flow rates and they concluded that efficiencies above 70% are achievable with the main losses occurring in the compressors and turbines. Sciacovelli et al. [17] included off-design turbine and compressor efficiencies and showed that the plant efficiency dropped from more than 70% to 64% when considering irregular operating conditions. Tola et al. [18] included off-design compressor efficiencies for variable pressure ratios and predicted quasi-steady-state (QSS) plant efficiencies of 71 – 77%. Zhang et al. [81] showed that by including part-load characteristics of heat exchangers, they could reduce their modeling error compared to experimental results, obtained with the pilot plant first described by Wang et al. [36], from above 20% to about 6%. In summary, the majority of the studies predict plant efficiencies in the range of 65% – 70% for QSS operation, and most authors conclude that unsteady operation and off-design performance of components have a negative impact on the efficiency, which indicates that more detailed studies aiming at category (2) are necessary.

Techno-economic analyses, such as the one presented by Abdon et al. [82], show that AA-CAES is an economically competitive, in terms of levelized cost of electricity storage, technology for daily, large scale electricity storage above 100 MW. What is missing in many techno-economic studies is a more detailed investigation of the grid integration of the storage technology and specifically what impact this has on the operation and design of AA-CAES plants. This requires connecting the categories (1) and (2), where questions about the electricity market participation, start-up times of the plant, or power in- and output ranges become important. To our knowledge, the studies by Rouindej et al. [23, 37] are the first to do research in this direction by statistically analyzing grid data to extract design, performance, and operational requirements for an AA-CAES plant. Because the focus of their study lies on the analysis of grid data, their AA-CAES model is simplified to a point where it is not possible to accurately predict whether a plant

would be capable to operate in the proposed way, because they assume that the plants can operate at any power level between 0% and 100% of their rated power. This is generally not possible for gas turbines, which usually have minimum loads in the range of 20% – 50% of the nominal power, see Hentschel et al. [83]. Additionally, for AA-CAES plants using caverns with varying pressures, so-called sliding pressure caverns, constant input and output power can only be achieved through active measures described below. For charging, we assume that the compressors are equipped with variable inlet guide vanes (VIGV), used to control the mass flow and therefore the power consumption. For discharging, considering that the turbine work is defined by the mass flow rate, inlet pressure, and the inlet temperature, three strategies can be defined as proposed by Jiang et al. [84]:

- Turbine inlet mass flow control (TIM): This would require VIGV, as assumed for the compressors. The complexity of such a mechanism increases considerably because of the high pressures present on the turbine inlet side.
- Turbine inlet pressure control (TIP): The implementation of a throttling valve enables controlling the inlet pressure to the turbine.
- Turbine inlet temperature control (TIT): By controlling the inlet temperature of the turbines, the power output can be controlled as long as the turbine outlet temperature is high enough to prevent freezing (condensation can also lead to damage in the turbines, see Caldwell [85], but this is neglected in this study).

TIP is not considered because this has already been investigated by several authors, see Sciacovelli et al. [17], Tola et al. [18]. TIM is not considered here because it seems to be the most unfeasible solution for large turbines. TIT, enabled with MTTES and mixing TCC as presented in chapter 2, will be assessed in this work. The second contribution of this work is the assessment of the plant performance under realistic, variable operating profiles.

4.2 Model description

The compressed air storage simulation (CASSI) model, available as open source code [43], can be used to model various types of CAES plants. In the following, models of the components relevant to AA-CAES plants are described. Air is treated as an ideal gas with the specific gas constant $R = 287.04 \text{ J/kgK}$, heat capacity ratio $\gamma = 1.4$, and temperature-dependent dynamic viscosity and thermal conductivity, extracted from Incropera [65]. The motor and generator dynamics are not modeled but represented by constant efficiencies η_{mot} and η_{gen} .

4.2.1 Compressor

The compressor is modeled as an adiabatic compression process of air with isentropic or polytropic efficiencies

$$\begin{aligned} \dot{W}_c &= \frac{\dot{m}_c(t)C_p(T)T_{c,\text{in}}(t)}{\eta_{s,c}} \left[\left(\frac{p_{c,\text{out}}(t)}{p_{c,\text{in}}(t)} \right)^{\frac{\gamma-1}{\gamma}} - 1 \right] \\ &= \dot{m}_c(t)C_p(T)T_{c,\text{in}}(t) \left[\left(\frac{p_{c,\text{out}}(t)}{p_{c,\text{in}}(t)} \right)^{\frac{\gamma-1}{\gamma} \frac{1}{\eta_{p,c}}} - 1 \right], \end{aligned} \quad (4.1)$$

where \dot{m}_c is the mass flow rate of air through the compressor, C_p is the specific heat capacity of the air at constant pressure, $T_{c,\text{in}}$ is the temperature of the air flowing into the compressor, $\eta_{s,c}$ and $\eta_{p,c}$ are the isentropic and polytropic efficiencies of the compressor, respectively, and $p_{c,\text{in}}$ and $p_{c,\text{out}}$ are the pressures of the air flowing into and out of the compressor, respectively. Integrating eq. (4.1) over the charging duration and taking into account the motor and mechanical efficiency results in the electrical energy consumed by the compressor,

$$E_{\text{el,mot}} = \frac{1}{\eta_{\text{mot}}\eta_{m,c}} \int_0^{\Delta t_c} \dot{m}_c(t) C_p(T) T_{c,\text{in}}(t) \left[\left(\frac{p_{c,\text{out}}(t)}{p_{c,\text{in}}(t)} \right)^{\frac{\gamma-1}{\gamma} \frac{1}{\eta_{p,c}}} - 1 \right] dt, \quad (4.2)$$

using the polytropic efficiency (the expression with the isentropic efficiency follows analogously), where η_{mech} and $\eta_{m,c}$ stand for the efficiency of the motor driving the compressor and the mechanical efficiency of the compressor, respectively.

4.2.2 Turbine

The turbine is modeled as an adiabatic expansion process of air with isentropic or polytropic efficiencies

$$\begin{aligned} \dot{W}_t &= \eta_{s,t} \dot{m}_d(t) C_p(T) T_{t,\text{in}}(t) \left[1 - \left(\frac{p_{t,\text{out}}(t)}{p_{t,\text{in}}(t)} \right)^{\frac{\gamma-1}{\gamma}} \right] \\ &= \dot{m}_d(t) C_p(T) T_{t,\text{in}}(t) \left[1 - \left(\frac{p_{t,\text{out}}(t)}{p_{t,\text{in}}(t)} \right)^{\frac{\gamma-1}{\gamma} \eta_{p,t}} \right], \end{aligned} \quad (4.3)$$

where \dot{m}_d is the mass flow rate of air through the turbine, $T_{t,\text{in}}$ is the temperature of the air flowing into the turbine, $\eta_{s,t}$ and $\eta_{p,t}$ are the isentropic and polytropic efficiencies of the turbine, respectively, and $p_{t,\text{in}}$ and $p_{t,\text{out}}$ are the pressures of the air flowing into and out of the turbine, respectively. Integrating eq. (4.3) over the discharging duration taking into account the generator and mechanical efficiency results in the electrical energy generated by the turbine,

$$E_{\text{el,gen}} = \eta_{\text{gen}} \eta_{m,t} \int_0^{\Delta t_d} \dot{m}_d(t) C_p(T) T_{t,\text{in}}(t) \left[1 - \left(\frac{p_{t,\text{out}}(t)}{p_{t,\text{in}}(t)} \right)^{\frac{\gamma-1}{\gamma} \eta_{p,t}} \right] dt, \quad (4.4)$$

for the polytropic efficiency (the expression with the isentropic efficiency follows analogously), where η_{gen} and $\eta_{m,t}$ stand for the efficiency of the generator connected to the turbine and the mechanical efficiency of the turbine, respectively.

4.2.3 TES

The TES is modeled in three ways of increasing complexity.

The first two methods are idealized TES models, with TES-A being an idealized zero-dimensional representation that was presented in chapter 3, and can be used to verify the numerical model against the thermodynamic AA-CAES theory. During charging, the TES-A model stores the thermal energy without losses and has a user-defined constant outflow temperature. During discharging, the outflow temperature corresponds to the time-averaged thermal input energy over the charging phase. The energy balance is checked and if TES-A is fully discharged, it returns the discharging inlet temperature as the outflow temperature. This model must only be used for constant mass flow simulations.

The second model is named TES-M and works similarly to TES-A, except that the charging temperature is mirrored in time, defined by,

$$T_{t,\text{in}}(t) = T_{c,\text{out}}(\Delta t_c - rt), \quad (4.5)$$

such that $T_{t,\text{in}}(0) = T_{c,\text{out}}(\Delta t_c)$ and $T_{t,\text{in}}(\Delta t_d) = T_{c,\text{out}}(0)$, where $r = \Delta t_c / \Delta t_d$, and $T_{c,\text{out}}$ is defined by,

$$\frac{T_{c,\text{out}}(t)}{T_{\text{atm}}} = 1 + \left[\left(\frac{p_{c,\text{out}}(t)}{p_{c,\text{in}}(t)} \right)^{\frac{\gamma-1}{\gamma} \frac{1}{\eta_{p,c}}} - 1 \right]. \quad (4.6)$$

The energy balance is checked as well, and once TES-M is empty, the discharging inlet temperature is returned as the outflow temperature. Again, this model must only be used for constant mass-flow simulations.

The third and most complex model, called TES-Q1d, was developed by Geissbühler et al. [29]. The TES-Q1d model can be accessed by the plant model through a dedicated interface. The plant model also includes an

MTTES routine, enabling mixing TCC as presented in chapter 2, used for TIT control.

4.2.4 Cavern

The evolution of the air in the cavern is modeled by solving the equations for conservation of mass and energy,

$$V_{\text{cav}} \frac{d\rho_{\text{cav}}}{dt} + \dot{m} = 0, \quad (4.7)$$

$$C_v V_{\text{cav}} \frac{d\rho_{\text{cav}} T_{\text{cav}}}{dt} + \dot{m} C_p T_t = Q_{l,\text{TES}} - Q'' S_{\text{cav}}, \quad (4.8)$$

where V_{cav} and S_{cav} are the volume and surface area of the cavern, ρ_{cav} is the air density in the cavern, \dot{m} is the air mass flow rate (positive during charging, negative during discharging), C_v is the specific heat capacity of the air at constant volume, T_{cav} is the air temperature in the cavern, T_t is the total temperature of the air flowing into/out of the cavern, $Q_{l,\text{TES}}$ is the heat loss of the TES, and Q'' is the cavern wall heat flux. The wall heat flux is modeled as,

$$Q'' = h(T_{\text{cav}} - T_{\text{wall}}), \quad (4.9)$$

where h is a user-defined convective heat-transfer coefficient, and T_{wall} is the constant wall temperature of the cavern. Equations (4.7) and (4.8) are integrated in time with the forward Euler method.

4.2.5 Heat exchanger and re-heater

Heat exchangers (HX) can be placed after TES units and after turbines, to prevent excess heat from entering the cavern during charging and discharging (which can happen due to high turbine exit temperatures), respectively. The HX model neglects pressure losses, and the outflow temperature is user-defined. The heat flux removed by the HX is,

$$Q_{\text{HX}} = \dot{m} C_p (T_{\text{HX,out}} - T_{\text{HX,in}}). \quad (4.10)$$

Re-heaters can be placed in front of every turbine, either in combination with a TES or used to model a diabatic CAES plant. Either way, they are modeled identical to the HX, delivering the required (for a defined power output) or user-defined (for constant mass flow) outflow temperature. The equation for the re-heaters follows analogously from eq. (4.10).

4.2.6 Throttling valve

A throttling valve can theoretically be placed in front of every turbine, but makes the most sense in front of the high-pressure turbine (HPT). The throttling is modeled as isenthalpic expansion, such that

$$\delta H = 0 \Rightarrow T = \text{const.} \quad (4.11)$$

4.3 Plant layout

The AA-CAES plant that is simulated and assessed is based on the concept of two-stage compression and expansion, using two hard-rock caverns as storage volumes with TES units placed inside the caverns. This concept was used in the pilot-scale experiments presented by Geissbühler et al. [19] and Becattini et al. [20]. By placing the TES inside the pressurized caverns, there is no need to build a pressure-resistant shell for the TES, as the pressure difference is caused only by the pressure loss across the packed bed. The packed bed consists of fluvial rocks as storage material.

The general plant layout is shown in fig. 4.1, with different states indicated by the numbers 1 – 10. During charging, ambient air (1) enters the low-pressure compressor (LPC), driven by an electric motor (M). The hot, compressed air (2) exiting the LPC then enters the TES situated in the low-pressure cavern and is cooled down, optionally an additional heat-exchanger (HX) removes any residual heat flowing out of the TES, before the compressed air enters the cavern (3). An equal amount of mass exits the low-pressure cavern, resulting in a constant pressure in the cavern in the ideal case when no thermal losses and leakage are present, and flows into the high-pressure

compressor (HPC), see (4). Its outflow (5) is cooled down in the TES situated in the high-pressure cavern, flows through an optional cooling HX afterwards, and enters the high-pressure cavern (6) that acts as the main pressure storage volume in the plant.

During discharging, air from the high-pressure cavern flows through the TES, where it is heated, can optionally be re-heated (similar to the HX, this is a user-defined component), and enters the HPT (7) and expands to the pressure in the low-pressure cavern (8). Before the air enters the low-pressure cavern (3-d), it is cooled down in a HX, to avoid large pressure variations in the low-pressure cavern. From there it is heated again in the TES, re-heated optionally, enters the LPT (9), where it expands to ambient pressure and the exhaust is rejected to the ambient (10). The generator (G) converts the mechanical energy of the LPT and HPT into electrical energy.

4.4 Operation modes

Two operation modes of achieving QSS for an AA-CAES plant can be thought of. One is based on defining the mass flows during charging and discharging, and the other is based on defining the power in- and output during charging and discharging.

The first mode allows for an estimation of the maximum plant performance, because mass conservation and therefore QSS is achieved by design (energy conservation is forced by the HX), but it does not allow to assess the plant performance for more realistic operation, where constant power in- and outputs are demanded.

As explained in the introduction, due to the variable pressure in the HP cavern, constant mass flow does not result in constant power for charging and discharging, see eqs. (4.1) and (4.3). Furthermore, the variable pressure ratio results in an increasing temperature at the HPC outlet during charging, which leads to a non-constant inlet temperature to the HPT during discharging if no additional measures are taken, and further increases the drop in output power during discharging.

The second operation mode is defined by adjusting the mass flow rate of the compressors during charging, and adjusting the inlet temperature of the turbine through MTTES using mixing TCC during discharging to compensate for the variable pressure ratios across the high-pressure compressor and turbine, respectively.

4.5 Plant sizing

Table 4.1 shows the target design parameters, boundary conditions, and turbomachine efficiencies of the plant shown in fig. 4.1. These parameters include the target power and capacity rating of the plant, the maximum pressure ratio over the compressors and turbines, the pressure in the low-pressure cavern, and the minimum and maximum pressures in the high-pressure cavern. What is missing for a complete plant design are cavern and

TES volumes, and a nominal mass flow rate to approximate the requested power output. Finding these missing parameters using an iterative approach with simulations is unsatisfactory, because it requires assumptions that require experience and makes the process slow. Much faster and more convenient is using the analytical plant model developed in chapter 3 and the ideal TES volume approach, assuming perfectly steep thermoclines, presented in chapter 2 to calculate a first set of design parameters for the plant.

Table 4.1: Design parameters of the proposed AA-CAES plant, see fig. 4.1, used in the assessment.

Quantity	Symbol	Value
Nominal discharge power	$P_{d,el}$	100 MW
Nominal discharge capacity	$E_{el,gen}$	500 MWh
Max. pressure ratio	π_{max}	10
Max. pressure HP-cavern	$p_{hp,cav,max}$	100 atm
Min. pressure HP-cavern	$p_{hp,cav,min}$	70 atm
Pressure LP-cavern	$p_{lp,cav}$	10 atm
Ambient pressure	p_{amb}	1 atm
Ambient temperature	T_{amb}	20 °C
HX target temperatures	T_3, T_6, T_{3-d}	20 °C
Polytropic compressor efficiencies	$\eta_{p,ipc}, \eta_{p,hpc}$	0.85
Polytropic turbine efficiencies	$\eta_{p,hpt}, \eta_{p,lpt}$	0.85
Motor & generator efficiency	η_{mot}, η_{gen}	0.98
Mechanical efficiency	η_m	0.98

The HP cavern volume is estimated with the analytical form of the volumetric energy density, see eq. (3.67). By rearranging this equation, we can easily calculate $V_{hp,cav} = 140\,347\text{ m}^3$, which was rounded to $140\,000\text{ m}^3$ and used in the simulations. According to chapter 3, the LP cavern volume should be sized such that the mass flowing through the cavern during charging is much greater than the mass inside the cavern and such that the TES

volume fits inside. Within this study, $V_{\text{pcav}} = 20\,000\text{ m}^3$ is chosen. The caverns are defined as cylindrical tunnels with $D = 10\text{ m}$.

A correlation for the ideal TES volume was shown by Haselbacher and Roos [74], and in combination with the MTTES non-dimensional volume approach presented in chapter 2, we calculate the required TES volumes for the low- and high-pressure caverns as,

$$\begin{aligned} V_{\text{hptes}} &= V_{\text{lptes}} = \tilde{V} V_{\text{hptes,ideal}} \\ &= \tilde{V} V_{\text{hpcav}} \frac{1}{(1-\phi)(\gamma-1)} \frac{p_{\text{atm}}}{\rho_s C_s T_{\text{atm}}} \frac{T_{\text{atm}}}{T_3} \\ &\quad \frac{T_3}{T_6} \frac{p_{\text{hpcav,max}}}{p_{\text{atm}}} \left(1 - \frac{p_{\text{hpcav,min}}}{p_{\text{hpcav,max}}}\right), \end{aligned} \quad (4.12)$$

with V_{hptes} , V_{lptes} , \tilde{V} , and $V_{\text{hptes,ideal}}$ defining the HP and LP TES volumes respectively, the non-dimensional storage volume, and the ideal HP TES volume. ϕ , ρ_s , and C_s define the void fraction of the packed bed, the density of the solid TES material, and the specific heat capacity of the solid, respectively. The non-dimensional storage volume \tilde{V} is used to find V_{hptes} which is larger than the ideal volume due to the thermocline degradation and thermal losses. For simplicity, \tilde{V} is chosen equal for LP- and HP TES in this study, whereas in reality slightly different values would be ideal due to the different temperature profiles in the TES. It was shown in chapter 2 that the non-dimensional storage volume is a function of the maximum temperature drop during discharging, which is dependent on the number of TES units and application of TCC. Table 4.2 shows the used TES volumes and geometries for the three TES systems that were assessed in this study.

The nominal mass flow rate can be found by dividing the mass change in the cavern between charging and discharging m_{cd} , defined as

$$\frac{m_{cd}}{m_{\text{hpcav,max}}} = 1 - \left(\frac{p_{\text{hpcav,min}}}{p_{\text{hpcav,max}}}\right)^{\frac{1}{\gamma}}, \quad (4.13)$$

with $m_{\text{hpcav,max}}$ denoting the mass in the HP cavern at $p_{\text{hpcav,max}}$. Using five hours as the desired time for charging and discharging, the mass flow rate

Table 4.2: TES geometry and TCC method for three TES systems with N TES units, top and bottom radii and heights were rounded to single digits.

N	TCC	\tilde{V}	V_i	R	r	H
[-]		[-]	[m ³]	[m]	[m]	[m]
1	-	3.0	5968.1	13.7	10.5	12.9
2	mixing	2.0	1984.1	9.5	7.3	8.9
3	mixing	2.0	1331.2	8.3	6.4	7.8

results in approximately $\dot{m}_c = \dot{m}_d = 200.7 \text{ kg/s}$ for the conditions shown table 4.1.

4.6 Performance assessment

An AA-CAES plant is an electricity storage device, therefore the most important performance indicators are the round-trip efficiency, called plant efficiency going forward, the volumetric energy density, and the power and capacity specific costs. The plant efficiency is defined by the ratio of electrical energy out- and input,

$$\eta = \frac{E_{\text{el,gen}}}{E_{\text{el,mot}}}, \quad (4.14)$$

with $E_{\text{el,gen}}$, and $E_{\text{el,mot}}$ defined by eqs. (4.2) and (4.4) and taking the sum of all compressor and turbine stages. The volumetric energy density is defined as $E_{\text{el,gen}}/V_{\text{hpcav}}$.

Both of these key performance indicators (KPI) are useful for QSS analyses. But for irregular operating conditions, which is the reality of electricity storage devices connected to an electricity grid, these KPIs are not sufficient. In this work, four new KPIs are introduced, namely the load-following quality, the power quality, and the periodic plant efficiency. The load-following quality Γ during discharging is defined by

$$\Gamma_{\text{gen}} = \frac{E_{\text{el,gen}}}{E_{\text{el,gen,req}}}, \quad (4.15)$$

where $E_{\text{el,gen}}$ and $E_{\text{el,gen,req}}$ define the actual, and the requested (by the grid profile) energy generated. For charging, the load following quality is defined analogously to eq. (4.15) by,

$$\Gamma_{\text{mot}} = \frac{E_{\text{el,mot}}}{E_{\text{el,mot,req}}}. \quad (4.16)$$

The power quality is defined by $1 - L^2$, where the L^2 norm is calculated using the difference between the actual and the requested charging or discharging

power, defined as

$$L_{\text{gen}}^2 = \sqrt{\frac{1}{N} \sum_{i=1}^N \left(\frac{\dot{W}_{\text{el,gen}} - \dot{W}_{\text{el,gen,req}}}{\dot{W}_{\text{el,gen,req}}} \right)^2} \quad \forall |\dot{W}_{\text{el,gen}}| > 0 \quad (4.17)$$

$$L_{\text{mot}}^2 = \sqrt{\frac{1}{N} \sum_{i=1}^N \left(\frac{\dot{W}_{\text{el,mot}} - \dot{W}_{\text{el,mot,req}}}{\dot{W}_{\text{el,mot,req}}} \right)^2} \quad \forall |\dot{W}_{\text{el,mot}}| > 0, \quad (4.18)$$

with N denoting one time step.

The periodic plant efficiency η_p , is defined analogously to eq. (4.14), but the ratio of energy discharged and energy charged is calculated over a user defined period of time rather than one charging and discharging cycle, because variable operating conditions make the definition of a cycle impossible.

4.7 Results

4.7.1 Verification

An order-verification study was performed to assess whether the errors of the numerical model scale with the order of accuracy $O(h^1)$ of the backward Euler method. The error of the simulation in comparison to the theory was defined with the plant efficiency, which in its analytical form, here labeled η_{th} , is defined by eqs. (3.60) and (3.61). The parameters listed in table 4.3 were used for the verification.

Figure 4.2 shows the results of the order verification study with the relative error of the plant efficiency as a function of the time-step that was gradually decreased by a factor of 10. The relative error is defined as

$$E = \frac{\eta - \eta_{\text{th}}}{\eta}, \quad (4.19)$$

with η being calculated by the numerical model, see eq. (4.14), and η_{th} defined by eq. (3.60). Overall, the error is seen to decrease by an order of

Table 4.3: Parameters used for the model verification.

Parameter	Value
$p_{\text{hpcav,max}}/p_{\text{hpcav,min}}$	1.05, 1.40, 3.00
$p_{\text{hpcav,max}}/p_{\text{atm}}$	32, 100, 100
$p_{\text{lpcav}}/p_{\text{atm}}$	10
$\eta_{s,\text{lpc}}, \eta_{s,\text{hpc}}, \eta_{s,\text{hpt}}, \eta_{s,\text{lpt}}$	0.85
$\eta_{\text{mot}}, \eta_{\text{gen}}, \eta_{m,\text{lpc}}, \eta_{m,\text{hpc}}, \eta_{m,\text{lpt}}, \eta_{m,\text{hpt}}$	0.98
\dot{m}_c, \dot{m}_d	200 kg/s

magnitude for each 10-fold reduction in the time step, indicating that the numerical plant model is indeed first-order accurate in time, as expected.

4.7.2 Quasi-steady operating conditions

Single-tank TES

A QSS simulation of the plant described and shown in section 4.3 and fig. 4.1 respectively, was performed with constant mass flow rates to assess the maximum performance of this plant concept. The chosen parameters are described in section 4.5 and the two caverns are equipped with single TES units as described in table 4.2, using identical insulation layers and aspect ratios presented in chapter 2. The TES-Q1d model is used for the simulations, and thermal losses of the TES and caverns with constant heat-transfer coefficients of $h = 10 \text{ W/m}^2\text{K}$ and constant wall temperatures of $T_{\text{lpcav,wall}} = T_{\text{hpcav,wall}} = 20^\circ\text{C}$ are considered, based on the study presented by Geissbühler et al. [19]. As reference, an additional simulation is performed for adiabatic caverns and TES. The simulations are run for a 24-hour period, where within the first 12 hours the plant is charged until full capacity is reached (defined by the maximum cavern pressure, see table 4.1), after which it idles for the remainder of the 12 hours, and in the second 12 hours it discharges until the plant is fully discharged, after which it idles for the remaining time. The resulting schedule is charging/idling/discharging/idling

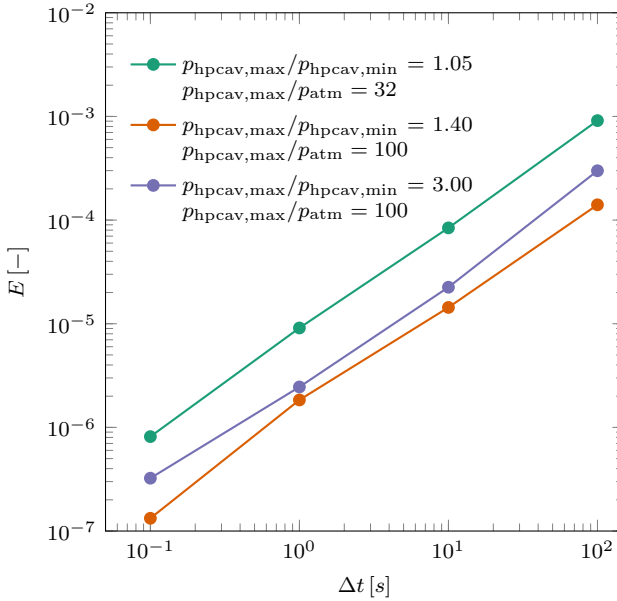


Figure 4.2: Order-verification study of the numerical model showing the relative error E defined by eq. (4.19) as a function of the time step for several values of $p_{\text{hpcav,max}}/p_{\text{hpcav,min}}$ and $p_{\text{hpcav,max}}/p_{\text{atm}}$ and for $p_{\text{lpcav}}/p_{\text{atm}} = 10$.

(C/I/D/I), which is repeated until the QSS is reached, defined by a relative change in the cavern pressures and temperatures smaller than $1 \cdot 10^{-7}$, evaluated at the end of two consecutive cycles using the pressures and temperatures at the end of charging.

Figure 4.3 shows the diabatic simulation results for the charging and discharging phases in terms of the in- and outflow temperatures, cavern pressures, and electric power for low- and high-pressure stages. The constant mass flow operation leads to unsteady power in- and outputs. The compressor outflow temperatures T_2 and T_5 are higher than the turbine inflow temperatures T_7 and T_9 , reflecting the thermal losses and thermocline degradation in the high- and low-pressure TES. The LPC power is constant,

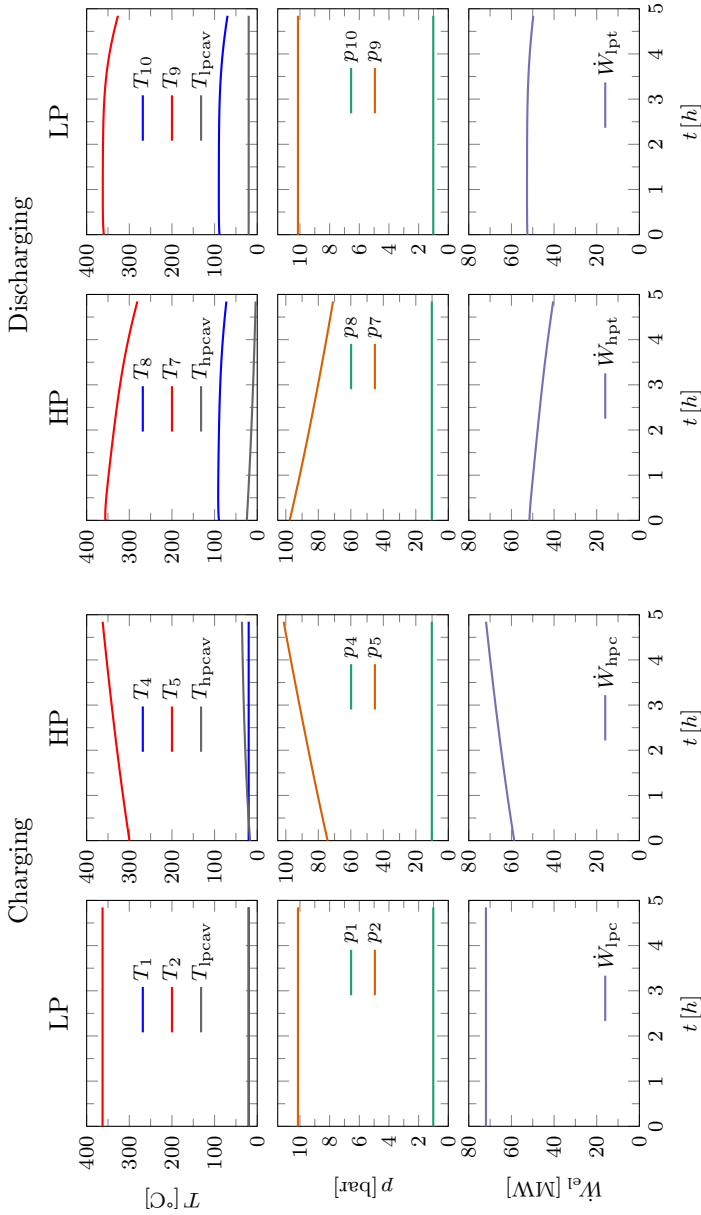


Figure 4.3: Results for QSS plant operation, indicating turbomachinery in- and outflow temperatures, in- and outflow pressures, and power in- and output shown for charging and discharging.

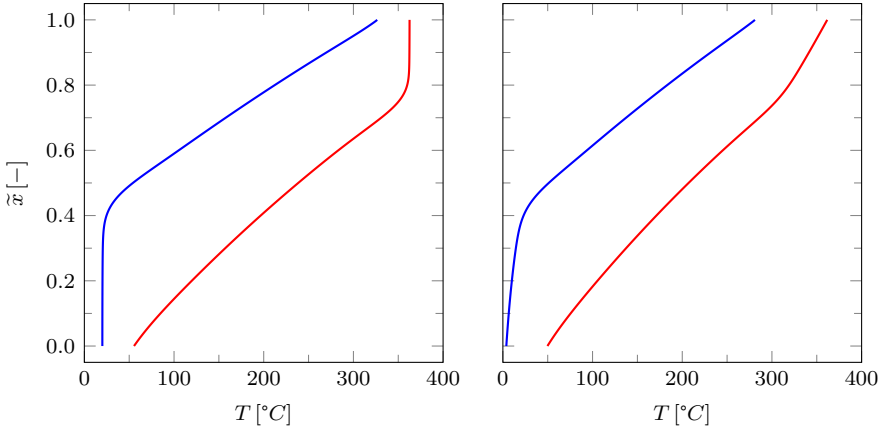


Figure 4.4: Thermoclines as a function of the non-dimensional TES height in the low- and high-pressure caverns at the QSS, left and right, at the end of charging (red) and discharging (blue), respectively.

while the HPC power increases as the HP cavern is filled. The HPT power decreases with the decreasing inflow pressure and temperature, and the LPT power decreases due to the decreasing inflow temperature.

Figure 4.4 shows the thermoclines at the QSS. The increasing inflow temperature into the HP TES creates an unfavorable situation, because the charging profile can already be viewed as a thermocline, which further decreases the utilization factor of the TES. Additionally, a considerable increase and decrease in the respective outflow temperatures is visible at the ends of charging and discharging.

Figure 4.5 shows the pressures p_3 and p_6 , and temperatures $T_{\text{lp cav}}$ and $T_{\text{hp cav}}$ of the LP, and HP caverns, respectively for the diabatic simulation. The LP cavern pressure p_3 is shown to be constant over the whole C/I/D/I cycle, which is achieved through the two HXs placed after the LP TES and after the HPT which keep the LP cavern temperature $T_{\text{lp cav}}$ constant. The HP cavern pressure p_6 and temperature $T_{\text{hp cav}}$ are increasing during charging, and decreasing during discharging, respectively. In the first idle

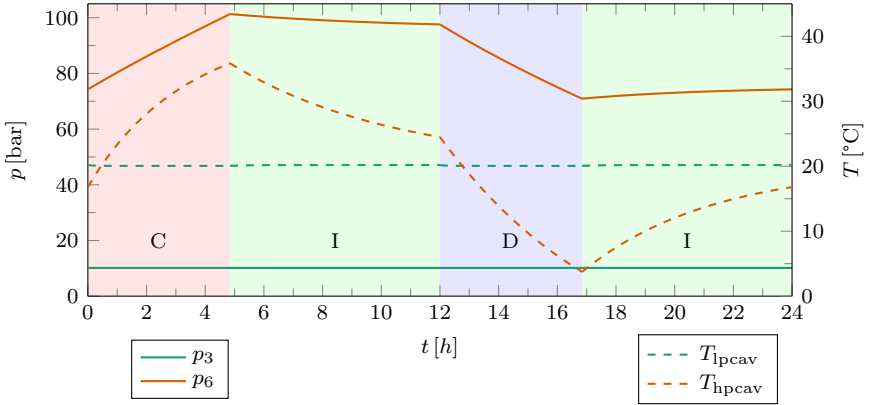


Figure 4.5: Pressure and temperature evolution in the low- and high-pressure caverns over the 24 hour C/I/D/I cycle.

phase after charging, T_{hpcav} is decreasing which leads to a decreasing cavern pressure p_6 and similarly in the second idle phase after discharging, T_{hpcav} is increasing which leads to an increasing cavern pressure p_6 . This decreases the actual ratio of $p_{\text{hpcav,max}}/p_{\text{hpcav,min}}$ from a target value of about 1.43 to about 1.38 during discharging, which decreases the energy storage capacity of the plant.

The KPIs of the diabatic and adiabatic simulations are summarized in table 4.4. The diabatic plant efficiency is below the predicted theoretical efficiency of 73% (calculated using eq. (3.60)), but still relatively high considering the simulation included thermal losses and idle periods which are not considered in the analytical model. A similar conclusion can be drawn for the volumetric energy density, which lies slightly below the value of 3.56 kWh/m^3 that is predicted by the theory. Comparing the results with the design parameters and sizing calculations in table 4.1 and section 4.5, we can assess the accuracy of the proposed sizing method.

The target of 500 MWh is not quite reached for $E_{\text{el,gen}}$, but still within 5% which is considered acceptable given the simplicity of the analytical

Table 4.4: KPIs and additional results from the QSS single TES simulation for diabatic and adiabatic conditions.

Parameter	Diabatic	Adiabatic
η	71.7%	72.5%
$E_{\text{el,gen}}/V_{\text{hpcav}}$	3.42 kWh/m ³	3.54 kWh/m ³
$E_{\text{el,gen}}$	478.22 MWh	495.07 MWh
$E_{\text{el,mot}}$	666.98 MWh	683.00 MWh
$\eta_{\text{ex,tes,lp}}$	98.9%	99.1%
$\eta_{\text{ex,tes,hp}}$	99.0%	99.3%
$E_{\text{hx,d}}$	64.97 MWh _{th}	62.73 MWh _{th}
$E_{\text{hx,c,lp}}$	6.19 MWh _{th}	5.13 MWh _{th}
$E_{\text{hx,c,hp}}$	6.09 MWh _{th}	4.08 MWh _{th}

model. The main reason for the lower generated energy lies in the thermal losses of the HP cavern and the idle periods, leading to a decreasing and increasing cavern pressure after charging and discharging, respectively, as shown in fig. 4.5. This is not the case for the adiabatic simulation where the target pressure ratio is reached. The exergy efficiencies of the TES units are very high for adiabatic and diabatic surroundings, having little impact on the overall efficiency. The energies removed by the HX's shown in table 4.4 show the considerable cooling requirement of the plant, especially after the HP turbine. The average thermal power during discharging is approximately 13.4 MW_{th}, while that during charging is below 2.2 MW_{th}, which are reported as references for HX design calculations.

To further assess the impact of the thermal losses of the caverns and TES units on plant performance, two additional simulations were performed for 48 h, and 96 h C/I/D/I cycles, representing multi-day storage periods. The resulting KPIs are shown in table 4.5 and indicate that for long storage periods, when T_{hpcav} approaches $T_{\text{hpcav,wall}}$ the plant efficiency stays above 70%. The TES exergy efficiencies also decrease only marginally, indicating that there is room to reduce the insulation thicknesses.

Table 4.5: KPI's and additional results from additional 48 h, and 96 h QSS single TES simulation for diabatic conditions.

Parameter	48 h	96 h
η	71.0%	70.8%
$E_{\text{el,gen}}/V_{\text{hpcav}}$	3.31 kWh/m ³	3.28 kWh/m ³
$E_{\text{el,gen}}$	463.37 MWh	460.23 MWh
$E_{\text{el,mot}}$	651.99 MWh	650.27 MWh
$\eta_{\text{ex,tes,lp}}$	98.2%	97.8%
$\eta_{\text{ex,tes,hp}}$	98.3%	98.0%
$E_{\text{hx,d}}$	62.37 MWh _{th}	61.05 MWh _{th}
$E_{\text{hx,c,lp}}$	3.52 MWh _{th}	3.29 MWh _{th}
$E_{\text{hx,c,hp}}$	7.50 MWh _{th}	7.68 MWh _{th}
$T_{\text{hpcav}}(t_{i1,\text{end}})$	20.56 °C	20.03 °C

Power control with MTTES

QSS simulations of the plant described in section 4.3 and shown in fig. 4.1 were performed in the constant power mode with TIT control and mass flow control for the compressors. The performance is assessed using the parameters given in section 4.5 and the two caverns equipped with two and three TES units for the LP and HP cavern respectively, as described in table 4.2, using identical insulation layers and aspect ratios presented in chapter 2.

Again, the TES-Q1d model was used for the simulations, including thermal losses of the TES and caverns with constant heat-transfer coefficients of $h = 10 \text{ W/m}^2\text{K}$ and cavern wall temperatures of $20 \text{ }^\circ\text{C}$. For comparison, an adiabatic simulation was performed as well. The operating schedule for this simulation is defined as charging with $\dot{W}_{\text{el,mot}} = \dot{W}_{\text{Ipc}} + \dot{W}_{\text{hpc}} = 135 \text{ MW}$ and discharging with $\dot{W}_{\text{el,gen}} = \dot{W}_{\text{Ipt}} + \dot{W}_{\text{hpt}} = 95.5 \text{ MW}$ (the power distribution between HPT and LPT is fixed at $\dot{W}_{\text{hpt}}/\dot{W}_{\text{Ipt}} = 0.876$) with the same C/I/D/I schedule using 24-hour cycles and simulation time steps of 10 s, repeated until a QSS is reached, defined by a relative change in the cavern

pressures and temperatures smaller than $1 \cdot 10^{-7}$, evaluated at the end of two consecutive cycles using the pressures and temperatures at the end of charging.

Figure 4.6 shows the results for the charging and discharging phases at the QSS simulation with constant power for diabatic conditions, with the in- and outflow temperatures, cavern pressures, and electric power for low- and high-pressure stages. During charging, as p_5 increases, the VIGVs of the LPC and HPC regulate the mass flow to achieve constant power consumption equal to $\dot{W}_{\text{el,mot}} = 135 \text{ MW}$. During discharging, the mass flow rate is constant and identical to the single-tank TES simulation from section 4.7.2 with the power control achieved through TIT control, using the MTTES systems to adjust the outflow temperature through mixing TCC, resulting in generated power equal to $\dot{W}_{\text{el,gen}} = 95.5 \text{ MW}$. For the HP turbine, the inflow temperature needs to increase as the cavern pressure decreases while for the LP turbine a constant inflow temperature is sufficient to reach constant power. It is important that while adjusting the HP and LP turbine inflow temperatures T_8 and T_{10} stay above 0°C to prevent freezing of the turbine blades, which is the case as shown in fig. 4.6.

Figures 4.7 and 4.8 show the mass flow and outflow temperature evolutions for charging (bottom) and discharging (top) for the MTTES system in the LP and HP cavern respectively, with the thermoclines at the ends of charging and discharging (middle) for each TES in the MTTES. Compared to the thermoclines of the single-tank TES in fig. 4.4, the MTTES thermoclines are much steeper, which is attributed to the mixing TCC method and also enabled the total TES volumes to be chosen with $\tilde{V} = 2$ instead of 3 for the single TES. During charging, the effect of the mixing method is visible by the constant outflow temperature phases in the bottom plot of figs. 4.7 and 4.8 whenever the mass flow rate of two TES is non-zero. The decreasing system mass flow rate \dot{m}_c indicates the power control mechanism during charging. During discharging, the mixing TCC method provides a constant MTTES outflow temperature $T_{d,\text{out}}$ for the LP turbine, shown in the top plot of fig. 4.7, which also includes mixing of the TES outflow temperature with

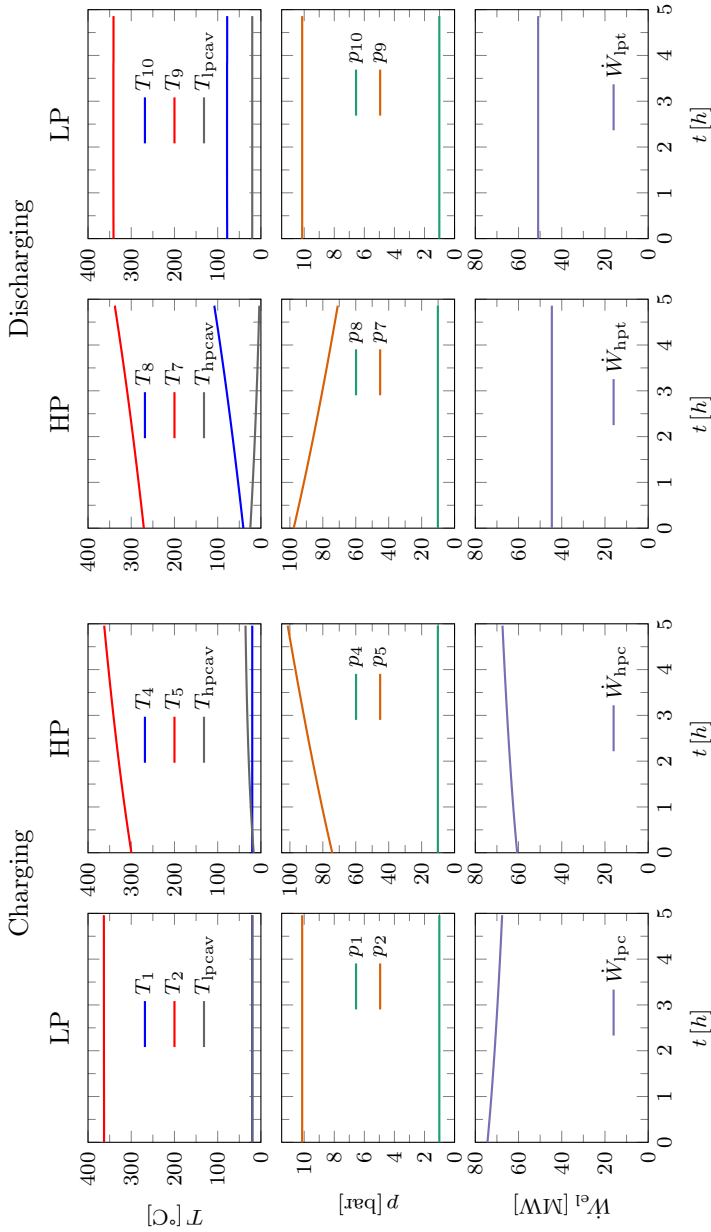


Figure 4.6: Results for QSS constant power plant operation, indicating turbomachinery in- and outflow temperatures, in- and outflow pressures, and power in- and output shown for charging and discharging.

air from the cavern at the beginning and end of the discharging phase when \dot{m}_1 and \dot{m}_2 are lower than \dot{m}_d . For the HP turbine, the inflow temperature must increase to counteract the decreasing pressure, shown in the top plot of fig. 4.8, where also some mixing with cavern air is necessary at the end of discharging. The number of TES units in the HP cavern prove to be especially important, because the highest outflow temperature is needed at the end of discharging, which is only possible if one TES still offers an outflow temperature that is sufficient.

Table 4.6: KPIs and additional results from the QSS constant power simulation.

Parameter	Diabatic	Adiabatic
η	69.3%	69.9%
$E_{\text{el,gen}}/V_{\text{hpcav}}$	3.31 kWh/m ³	3.41 kWh/m ³
$E_{\text{el,gen}}$	464.04 MWh	477.51 MWh
$E_{\text{el,mot}}$	669.51 MWh	683.45 MWh
$\eta_{\text{ex,tes,lp}}$	96.6%	96.6%
$\eta_{\text{ex,tes,hp}}$	94.9%	94.9%
$E_{\text{hx,d}}$	51.33 MWh _{th}	47.72 MWh _{th}
$E_{\text{hx,c,lp}}$	20.05 MWh _{th}	21.93 MWh _{th}
$E_{\text{hx,c,hp}}$	21.66 MWh _{th}	36.67 MWh _{th}

The KPIs are summarized in table 4.6. For diabatic and adiabatic conditions the plant efficiencies are below that obtained for constant mass flow, single TES plant, which is attributed to the TIT control applied at the HP and LP turbines through the MTES systems with mixing TCC. The same applies for the volumetric energy densities. The TES exergy efficiencies are almost identical for the diabatic and adiabatic case, indicating that the main exergy loss is attributed to the mixing TCC method, rather than the heat losses. Compared to the sizing targets, the generated electrical energy is approximately 7% below the target due to the thermal losses in the cavern during idling and the thermal throttling of the turbines. The HX thermal

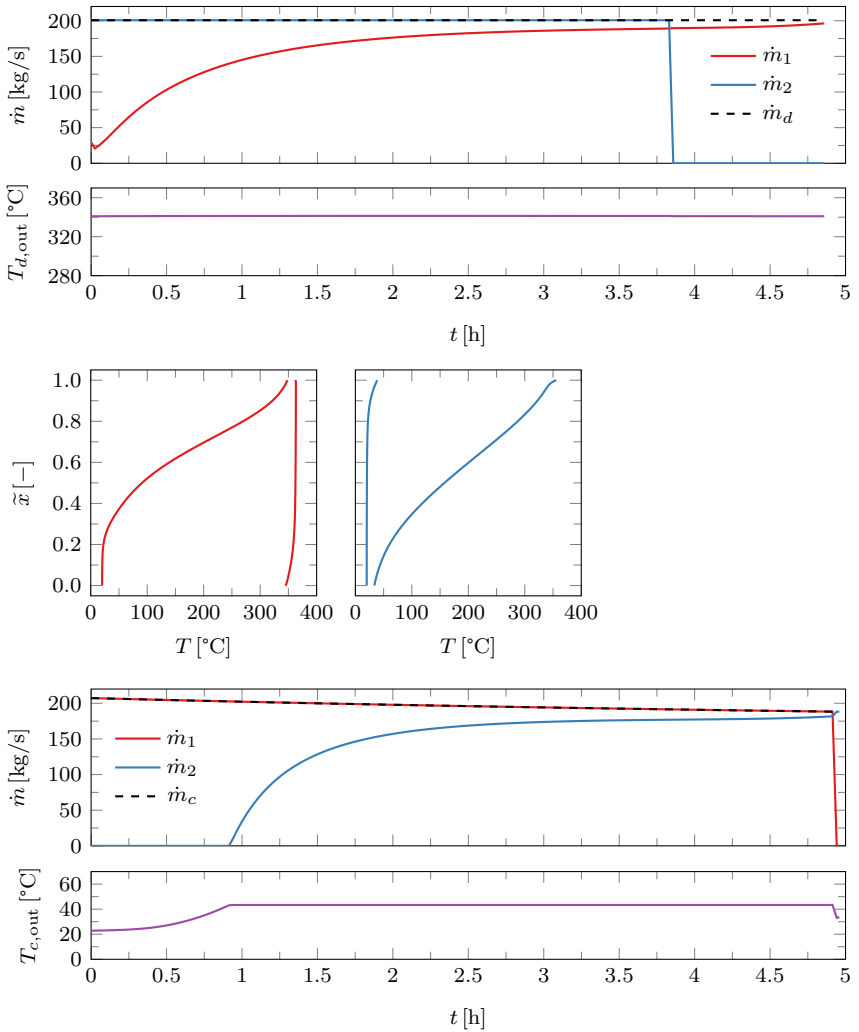


Figure 4.7: Mass flow and outflow temperature evolutions for charging (bottom) and discharging (top) for the MTTES system in the LP cavern, with the thermoclines of the two TES tanks at the end of charging and discharging (middle). The colors of the thermoclines match the colors of the corresponding mass flow rates and the black dashed line indicates the overall mass flow rate of the system.

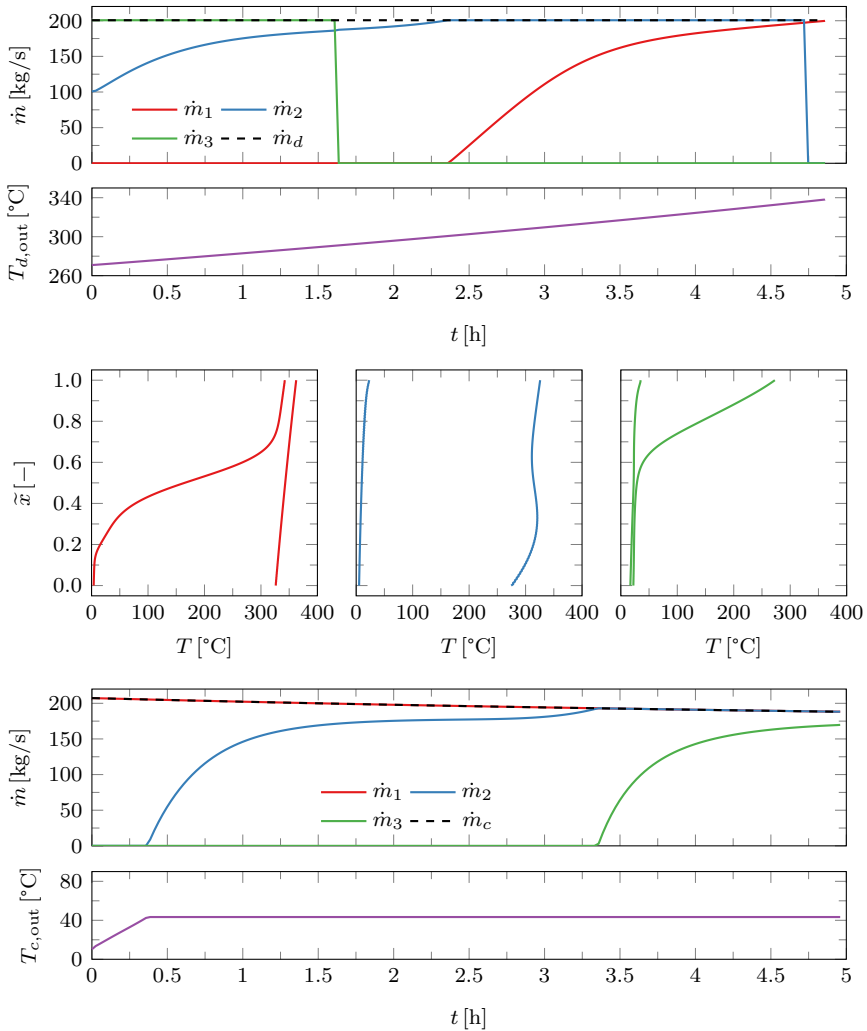


Figure 4.8: Mass flow and outflow temperature evolutions for charging (bottom) and discharging (top) for the MTTES system in the HP cavern, with the thermoclines of the three TES tanks at the end of charging and discharging (middle). The colors of the thermoclines match the colors of the corresponding mass flow rates and the black dashed line indicates the overall mass flow rate of the system.

energies shown in table 4.6 show the cooling requirement of the plant. The thermal energies during charging increased compared to the single TES simulations due to the higher outflow temperatures created by the mixing TCC method, while the thermal energies during discharging decreased due to the increasing inflow temperature of the turbine. The average thermal cooling power during discharging is approximately $10.9 \text{ MW}_{\text{th}}$, while the average cooling power during charging is $3.5 \text{ MW}_{\text{th}}$ and $4.3 \text{ MW}_{\text{th}}$ for the LP and HP heat exchangers, respectively.

Exergy efficiency breakdown

The comparison of the diabatic simulations of the plants with single-tank and MTTES requires a more detailed exergy analysis, which is presented here in the form of Sankey diagrams. The exergy flows were calculated with

$$e_i = \dot{m}_i C_p T_i + \dot{m}_i T_0 (R_{\text{air}} \log(p_i/p_0) - C_p \log(T_i/T_0)), \quad (4.20)$$

where R_{air} denotes the specific gas constant for air, $T_0 = 293.15 \text{ K}$ is the reference temperature where the air is considered to have zero exergetic value (analogously $p_0 = 1 \text{ atm}$). The index i corresponds to the numbers shown in the plant schematic in fig. 4.1. The exergy flows e_i were integrated in time to get the total exergy values that are presented in figs. 4.9 to 4.12 and normalized using the total electrical input exergies to the LPC and HPC

$$\Xi_i = \frac{\int_0^{\Delta t} e_i dt}{E_{\text{el,mot}}}. \quad (4.21)$$

Figures 4.9 and 4.10 present the charging exergy flows for the single-tank and MTTES QSS, respectively, while figs. 4.11 and 4.12 present the discharging exergy flows for the two simulations.

A closer investigation of fig. 4.9 shows that the main exergy losses of the plant come from the LPC and HPC and that the share of thermal exergy and exergy in the form of compressed air in the HP-Cavern is about 36% for the LP- and HP-TES combined and 64% of the exergy is stored in the HP-Cavern. The HP-TES stores less exergy than the LP-TES because of

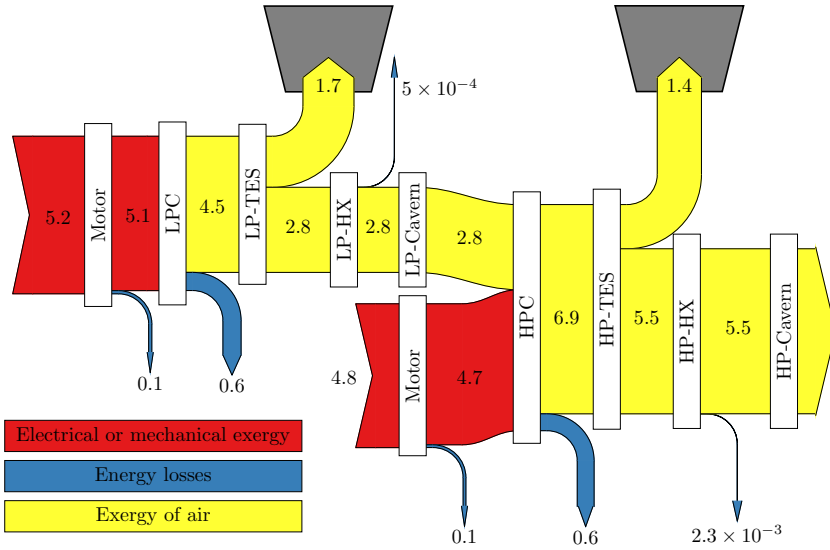


Figure 4.9: Sankey diagram showing the charging exergy flows of the diabolic, single-tank QSS simulation with KPIs presented in table 4.4. The total exergy values calculated with eq. (4.21) were multiplied by a factor of 10 to make the diagram more readable. This means that the sum of the electrical exergy flowing into the motors of LPC and HPC correspond to $E_{el,mot}$ from table 4.4.

the sliding pressure in the HP-Cavern, creating a lower average charging temperature. The HXs only create minimal exergy losses because the outlet temperatures of the TES are not exceedingly high.

Figure 4.10 shows a similar picture as fig. 4.9, but the required LPC and HPC works are higher due to the increased pressure losses due to the MTTES systems, and together with the higher temperatures flowing into the HP-Cavern because of the mixing TCC, resulting in a slightly higher total exergy stored in the HP-Cavern. Also the exergy stored in the HP-TES is slightly increased compared to the single-tank system. The main losses again are attributed to the LPC and HPC inefficiencies. The HXs still do not

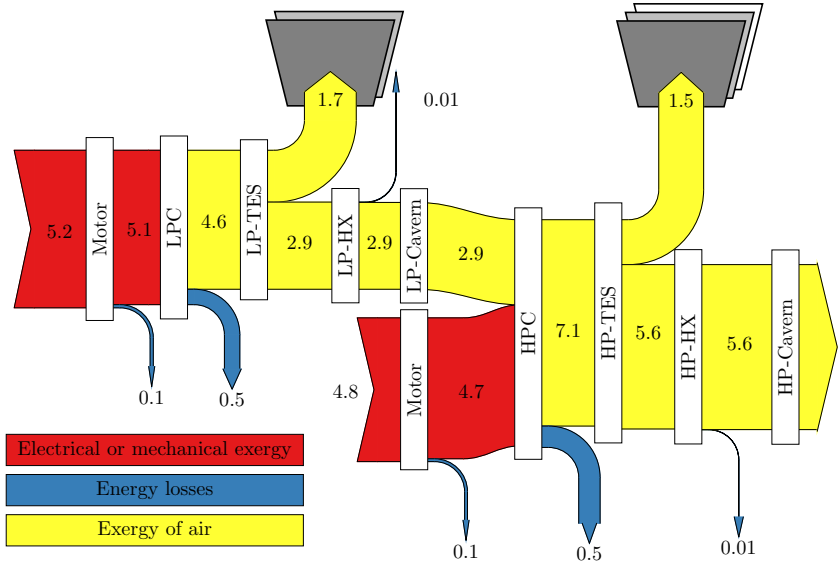


Figure 4.10: Sankey diagram showing the charging exergy flows of the diabatic, MTTES QSS simulation with KPIs presented in table 4.6. The total exergy values calculated with eq. (4.21) were multiplied by a factor of 10 to make the diagram more readable.

destroy excessive amounts of exergy, but more than in the single-tank plant because mixing TCC delivers a constant, higher outflow temperature to the HXs during charging, for the benefit of increasing the thermocline steepness in the MTTES. The shares of stored exergy are equal to the single-tank plant with 36% stored in the MTTES and 64% stored in the HP-Cavern.

Figure 4.11 shows the exergy flows during discharging of the single-tank plant. The main losses again are created in the HPT and LPT. The exergy losses in the TES units are very small in comparison, resulting in an overall efficiency of 71.7%, as readable in fig. 4.11 by summation of the electrical exergies from the two generators $3.79 + 3.38$ and considering the factor 10. The losses of the TES units are very small with values of 0.06 and 0.07,

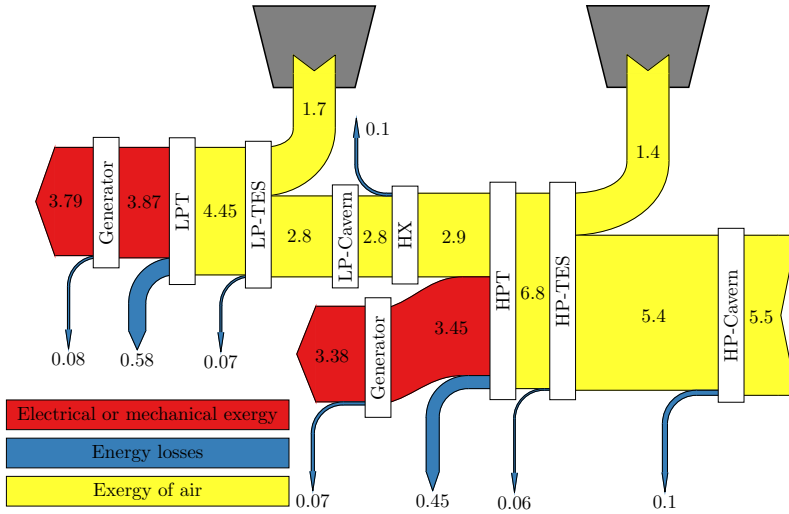


Figure 4.11: Sankey diagram showing the discharging exergy flows of the diabatic, single-tank QSS simulation with KPIs presented in table 4.4. The total exergy values calculated with eq. (4.21) were multiplied by a factor of 10 to make the diagram more readable. This means that the sum of the electrical exergy flowing into the motors of LPC and HPC correspond to $E_{el,mot}$ from table 4.4.

respectively, compared to the other losses.

Figure 4.12 shows the discharging exergy flows for the MTTES plant. There are increased losses from the two MTTES systems and the HP-Cavern compared to the single-tank plant, resulting in an overall lower efficiency of 69.3%. The increased cavern losses can be attributed to the heat losses to the cavern walls during idling, while the increased losses through the MTTES come from higher pressure losses and losses from the mixing TCC method that enables the constant power output of the plant. The HPT and LPT are still destroying the largest amount of exergy, but the TES units come second, indicating a potential to optimize the design of MTTES.

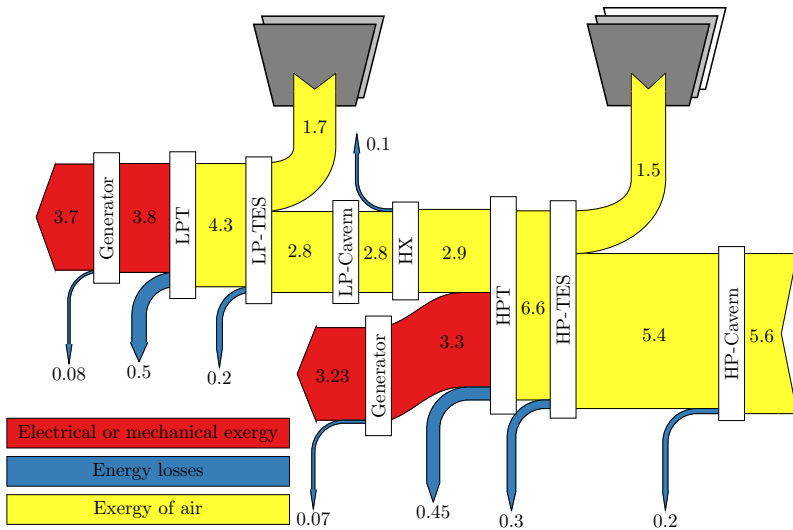


Figure 4.12: Sankey diagram showing the discharging exergy flows of the diabatic, MTTES QSS simulation with KPIs presented in table 4.6. The total exergy values calculated with eq. (4.21) were multiplied by a factor of 10 to make the diagram more readable.

4.7.3 Variable operating conditions

As described in the introduction, AA-CAES plants ultimately have to be designed considering the integration of the plant into the electricity grid, which leads to variable operating schedules. Due to a lack of grid data from simulations or literature, we created a 48-hour variable operating profile, that was defined with one hour segments as shown in fig. 4.13. The profile qualitatively mimics two days of daily energy storage, derived from today's electricity demand and prices, where the plant is charging during the night and in the afternoon, justified by low energy prices during nighttime and declining demand in the early afternoon, while discharging is concentrated in the morning, noon, and early evening, justified by high demand in those periods and lower renewable generation in the morning and

early evening. The simulations were performed for a plant using MTES, identical to section 4.7.2, and for comparison using a single-tank TES setup where mixing was performed with cavern air. The control works identical to section 4.7.2 except for the replacement of the MTES with the single TES system shown in table 4.2, using the same power distribution ratio of 0.876 between the HP, and LP turbine for both simulations. The simulations were performed for two-week periods, repeating the 48-hour profile. Figures 4.13 and 4.14 show the results for the last two days of the operating schedule. While the plant with MTES seems to be capable of following the requested power levels, see fig. 4.13, power drops are clearly visible for the plant with single-tank TES, see fig. 4.14. To quantify the results, the KPIs, as presented in section 4.6, of load-following quality and power quality during charging and discharging, and the periodic plant efficiency are calculated with the results listed in table 4.7.

For load-following qualities of 100% for charging and discharging, the periodic plant efficiency would be $\eta_{p,\max} = 67.06\%$, allowing the conclusion that for this particular simulation, the plant seems to work reasonably well, underlined by the load following qualities being close to 100% with a small advantage for the MTES plant during discharging. The power qualities for both cases are 100% during charging, while during discharging only the plant equipped with MTES achieves a power quality of 100. The power quality for the plant with single-tank TES is 99.4, which seems very high as well, however the power drops visible in fig. 4.14 are in the range of several MWs. A potential problem is indicated by the high HX energy demands for both cases, which is due to the fact that the turbine powers are only controlled with TIT, leading to an overheating of the TES systems over time.

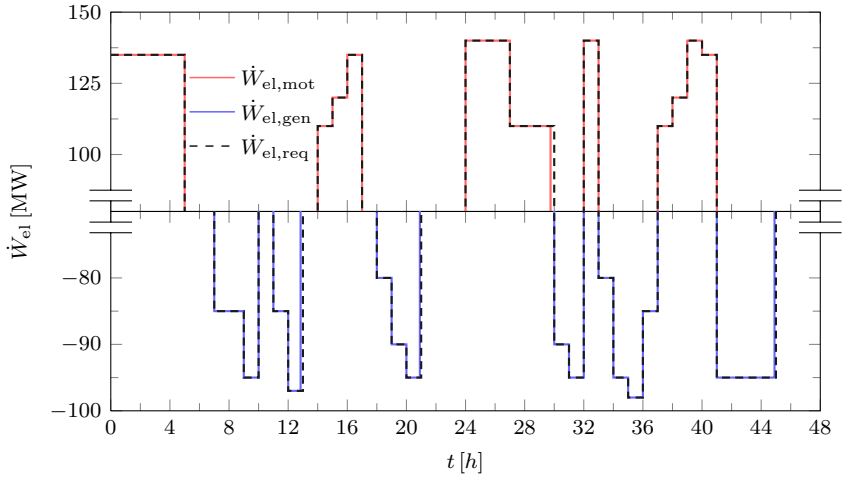


Figure 4.13: The last two days of a two-week simulation with repeating 48-hour operating profile with MTTES TIT control. The dashed line shows the profile requested from the plant, while red and blue correspond to the actual profiles the plant delivered.

Table 4.7: KPIs and additional results for the variable operating conditions using MTTES in the two caverns.

Parameter	MTTES	Single TES
η_p	66.5%	66.4%
Γ_{gen}	98.0%	97.8%
Γ_{mot}	98.9%	98.9%
$1 - L_{\text{gen}}^2$	100%	99.4%
$1 - L_{\text{mot}}^2$	100%	100%
$E_{\text{el,gen}}$	1602.03 MWh	1598.59 MWh
$E_{\text{el,mot}}$	2407.72 MWh	2407.32 MWh
$E_{\text{hx,d}}$	128.07 MWh _{th}	121.54 MWh _{th}
$E_{\text{hx,c,lp}}$	185.66 MWh _{th}	180.77 MWh _{th}
$E_{\text{hx,c,hp}}$	174.56 MWh _{th}	184.76 MWh _{th}

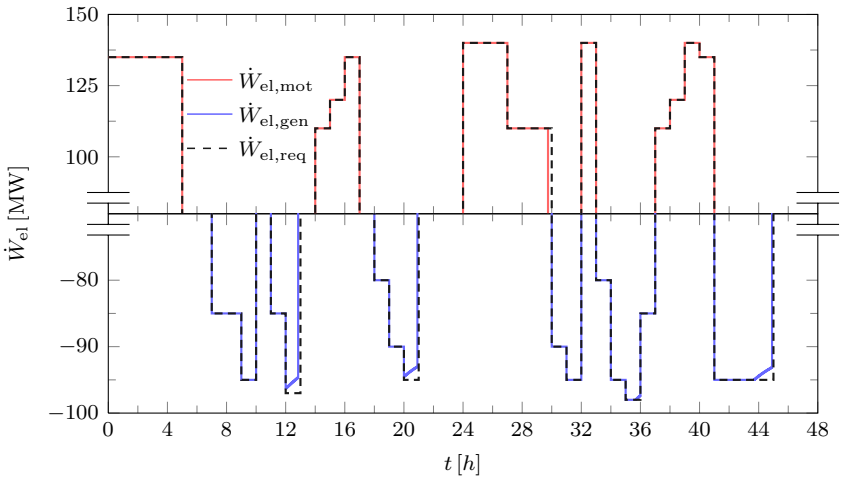


Figure 4.14: The last two days of a two-week simulation with repeating 48-hour operating profile with single-tank TES TIT control. The dashed line shows the profile requested from the plant, while red and blue correspond to the actual profiles the plant delivered.

4.8 Summary, conclusions, and future work

The present work provides a detailed numerical analysis of AA-CAES plants for QSS and variable, realistic operating conditions including a new approach to fast plant sizing, and a model verification, both using an analytical plant model.

The presented numerical plant model was first verified with an analytical model, see chapter 3. Using the analytical model and the work presented chapter 2, the plant was sized in a fast and convenient way using only a few design parameters shown in table 4.1 for a target of $100 \text{ MW}_{\text{el}}/500 \text{ MWh}_{\text{el}}$ discharge power and capacity, respectively.

Constant mass flow QSS simulations under diabatic and adiabatic conditions with single TES units in the LP and HP cavern showed that the cavern and mass flow dimensioning with the analytical model, and the TES sizing with the non-dimensional volume approach created a plant design that was within 5% of the desired targets for storage capacity, electrical output power, and plant efficiency despite the inclusion of thermal losses in the numerical simulation. The simulation also showed the potential performance of the presented plant layout, achieving QSS plant efficiencies of 71.7% including thermal losses. The main problem with this plant operating mode was shown to be the unsteady power in- and outputs, due to the sliding pressure in the HP cavern, which would prohibit a participation in the electricity market, where constant powers are required, see for example Swissgrid [86].

Achieving constant power was addressed with the power control operation mode, enabled by MTTES systems in the caverns employing mixing TCC to control the TIT during discharging, and mass flow control during charging. The results showed a lower, but still comparable performance with a plant efficiency of 69.3%, electrical discharge capacity of 464.04 MWh, and discharge power of 95.5 MW. These results are encouraging, showing that TIT is a reasonable solution to achieve constant discharge power for AA-CAES plants with sliding pressure caverns. Also, the total TES volume of the MTTES systems was 33% smaller, enabling decreased TES dimensions to potentially

better fit in the pressurized storage cavern. The exergy efficiencies of the MTES systems were lower compared to the single TES constant mass flow operation, achieving 96.6% and 94.9% for the LP and HP TES, respectively, compared to 98.9% and 99.0%, which was mainly attributed to the mixing TCC method.

The assessment on variable operation with a realistic daily operating profile showed that it is generally possible to use this plant layout with power control and MTES to provide energy storage services to an electricity grid, achieving a periodic plant efficiency of 66.5%, load following qualities above 98%, and power qualities of 100% over a two week period. In comparison, when using single TES and power control, the periodic plant efficiency dropped to 66.4%, the load following quality during discharging dropped to 97.8%, and the discharging power quality dropped to 99.4%. While these seem like very small differences, they could prove to be crucial to enable the electricity market participation of AA-CAES plants, because failures in load following or power quality can lead to monetary penalties from the grid operator, or even render the technology unfit to pass a qualification test by the grid operator, see Swissgrid [87]. The main problem using TIT for load following lies in the overheating of the MTES systems, due to the thermal throttling applied to reduce the turbine powers. While it would be generally possible to empty the MTES systems during charging by releasing excess energy to the HXs, it is questionable whether such an approach would be economical.

Future work should be focused on plant design optimization for operating profiles, that ideally come from grid data or grid simulations which would create the possibility to couple the performance assessment with economical considerations. Additionally, we intend to use numerical optimization algorithms to automatically design plants for given operating profiles, creating the possibility to examine a much broader space of design variables and connect the load following and power qualities with plant costs. The problem of MTES overheating due to TIT control and load following is something that needs to be addressed by testing and quantifying the possibility and the

impacts of releasing excess heat during charging to the HXs, or for example by combining TIT and TIP control. Regarding the model, future work should include efficiency maps for the turbines and compressors. Another important aspect are the thermal losses in the HP cavern, as the pressure decrease during idling due to the thermal losses is a major contributor to lower storage capacities of the plant.

MULTI-OBJECTIVE OPTIMIZATION OF AA-CAES PLANTS ¹

5.1 Introduction

The design space of AA-CAES with respect to the plant efficiency, in its simplified form and assuming constant turbomachinery efficiencies, can be described by three pressure ratios, $p_{\text{hpcav,max}}/p_{\text{hpcav,min}}$, $p_{\text{hpcav,max}}/p_{\text{atm}}$, $p_{\text{lpcav}}/p_{\text{atm}}$, and the temperature ratio T_{atm}/T_3 according to the analytical plant model described in chapter 3, eq. (3.60). Assuming ten values for all four variables, this results already in 10^4 combinations. While these could be computed by brute-force simulations, once more complex assumptions are made, for example the inclusion of more realistic TES models where the tank geometry and insulation materials and thicknesses, the number of

¹Material in this chapter has been extracted from P. Gassmann, “Development of an automated AA-CAES plant design tool based on numerical optimization”, Master Thesis, ETH Zurich, 2020, performed under the supervision of the author.

TES units per cavern, turbomachine efficiency maps, or variable operating conditions have to be defined, the brute-force approach becomes impractical. This is where numerical-optimization algorithms can help to decrease the computational time and potentially enable insights to designs that are not intuitive.

Marti et al. [45] showed that for a single-tank TES optimization with a gradient-based algorithm, using an objective function composed of the exergy efficiency and material costs, with the packed-bed height, top and bottom radii, insulation layer thicknesses, and rock diameters as design variables, the computational time could be reduced by 91 – 99% compared to the brute-force approach. Their results indicate that considerable cost reductions are achievable for small decreases in exergy efficiency.

Ahrens et al. [46], Sharma et al. [88], and Ahrens et al. [89] were the first to our knowledge to present work on computer-aided optimal design of D-CAES systems. They divided the optimization problem into three sub-systems, namely the compression train including the aquifer, the expansion train, and the utility grid defining the operation of the plant. Their optimum design was defined by the minimum normalized system cost, and they found that compared to a previously defined intuitive design, the optimized solution had only 22% of the capital cost, 52% of the operating costs, and only 54 boreholes compared to the initial 700.

Succar et al. [47] presented an optimization study for wind-turbine arrays coupled to D-CAES. They showed that the co-optimized wind and D-CAES systems were substantially different from stand-alone systems, requiring a lower storage capacity and lower power rating of the wind farm. This was possible because the wind turbines could be derated when storage was present, lowering the levelized cost of electricity, reducing storage power and capacity requirements, and increasing the wind energy transmitted directly to the grid.

Hong and Chen [48] presented a study on numerical optimization for an AA-CAES plant using artificial air storage vessels. They were using a simple TES model with a constant storage efficiency and used the round-trip

efficiency, system costs, and profit, defined with a constant ratio between the price of electricity during charging and discharging, as optimization objectives. They concluded that the different objectives are competing, but that a good trade-off can be found where the system is more efficient and economic compared to the initial design, reaching an increase in profit of 8.9% compared to the conventional design.

In summary, it can be stated that only few studies exist on the numerical optimization of AA-CAES plants and they are usually not comparable due to widely differing system layouts, and operating environments. Our main goal in this work is to perform numerical optimization simulations, using the newly developed numerical plant model presented in chapter 4, with a more general plant layout to create optimal designs defined by the plant costs and efficiency. The optimization includes cost models for the relevant components, constant and variable efficiency maps for the turbomachinery, the two TES models (TES-A and TES-M), presented in section 4.2.3, and constant operating conditions.

5.2 Design method

The design method is established by coupling the numerical AA-CAES model, presented in chapter 4, with the black-box optimization software NOMAD (Nonlinear Optimization by Mesh Adaptive Direct Search), see Abramson et al. [90] and Le Digabel [91].

5.2.1 AA-CAES and TES model

CASSI, as presented in chapter 4, is used as the numerical plant model for the optimizations. The general plant layout used for the optimization is shown in fig. 4.1, representing a two-stage compression and expansion configuration, using two caverns each of which contains TES systems.

Table 5.1: Specific cost figures for the capital cost calculation.

Parameter	Variable	Cost
Cavern excavation	c_{exc}	175 CHF/m ³
Cavern lining	c_{lin}	60 CHF/m ²
Compressor	c_c	560.23 CHF/kW
Turbine	c_t	336.02 CHF/kW

The capital cost of the plant is calculated as,

$$C_{\text{plant}} = C_{\text{cav}} + C_{\text{tm}} + C_{\text{TES}}, \quad (5.1)$$

$$C_{\text{cav}} = c_{\text{exc}} V_{\text{cav}} + c_{\text{lin}} S_{\text{cav}}, \quad (5.2)$$

$$C_{\text{tm}} = c_c P_c + c_t P_t + C_{\text{mot}} + C_{\text{gen}}, \quad (5.3)$$

where C_{plant} denotes the plants capital cost, C_{cav} the cavern cost, C_{tm} the turbomachinery cost, and C_{TES} the TES material cost. The specific cost figures are presented in table 5.1 (showing costs relative to the cavern volume and the surface area, and compressor and turbine power) extracted from a previous project that performed a life-cycle analysis of an AA-CAES plant, see Motmans [92], and input from industry partners. The TES costs were neglected for the simulations with TES-A and TES-M.

Additional costs for the motor and generator of the plant are calculated using eqs. (5.4) and (5.5), with P_c and P_t defining the maximum power of the respective turbomachines,

$$C_{\text{mot}} = 3.15 \cdot 10^6 \left(\frac{P_c}{50} \right)^{0.4} \quad (5.4)$$

$$C_{\text{gen}} = 3.15 \cdot 10^6 \left(\frac{P_t}{50} \right)^{0.4} \quad (5.5)$$

5.2.2 Optimization package

NOMAD is an open-source optimization software package, see Abramson et al. [90], that solves black-box optimization problems, defined as

$$\min_{x \in \Omega} f(x), \quad (5.6)$$

where the minimum of the objective function $f(x)$ is searched in the design space Ω for designs defined by trial points x . The trial points x can contain real, integer, binary (one or zero), and categorical (a set of none discontinuous choices, e.g. a finite number of different insulation materials) design variables, and are sent to the black-box model, where the trial point is translated, simulated and the objective function is evaluated. The design space is defined by bounds for the design variables and constraints defined as nonlinear inequalities $c_j(x) \leq 0 \forall j \in J = \{1, 2, \dots, m\}$. The constraints are treated by the extreme barrier (EB) or progressive barrier (PB) algorithm. The former rejects all infeasible trial points by setting their objective function to infinity, while the latter allows constraint violations up to a user-defined threshold that is progressively tightened, rejecting infeasible points that exceed the threshold.

5.2.3 Coupling

The coupling of NOMAD with the plant model is schematically shown in fig. 5.1. The resulting design tool is divided in three blocks, the NOMAD optimizer, the plant model, and an interface that connects the two codes. The interface is divided into two parts: The input preparation that translates the trial point from NOMAD to a plant-model input, checks EB constraints, and writes the input files for the execution of CASSI. The second part includes the output processing, where the CASSI output is read, and PB constraints and the objective function are calculated. NOMAD handles the objective and PB constraint evaluation, the trial-point generation (including a neighborhood generator that creates possible combinations of categorical design variables if defined in the input), and the simulation progress, ending

the simulation once the solution has converged and an optimal design has been found.

The user input is divided in three parts: The NOMAD input, where mesh sizes for design variables defining the minimum step size Δx between two points, options for the optimization algorithm, constraints and objectives with corresponding weights are chosen; the plant input, where the plant setup and operating conditions are defined; and the TES-Q1d input, where the TES geometry, storage, structure, and insulation materials and thicknesses are defined if this model is used.

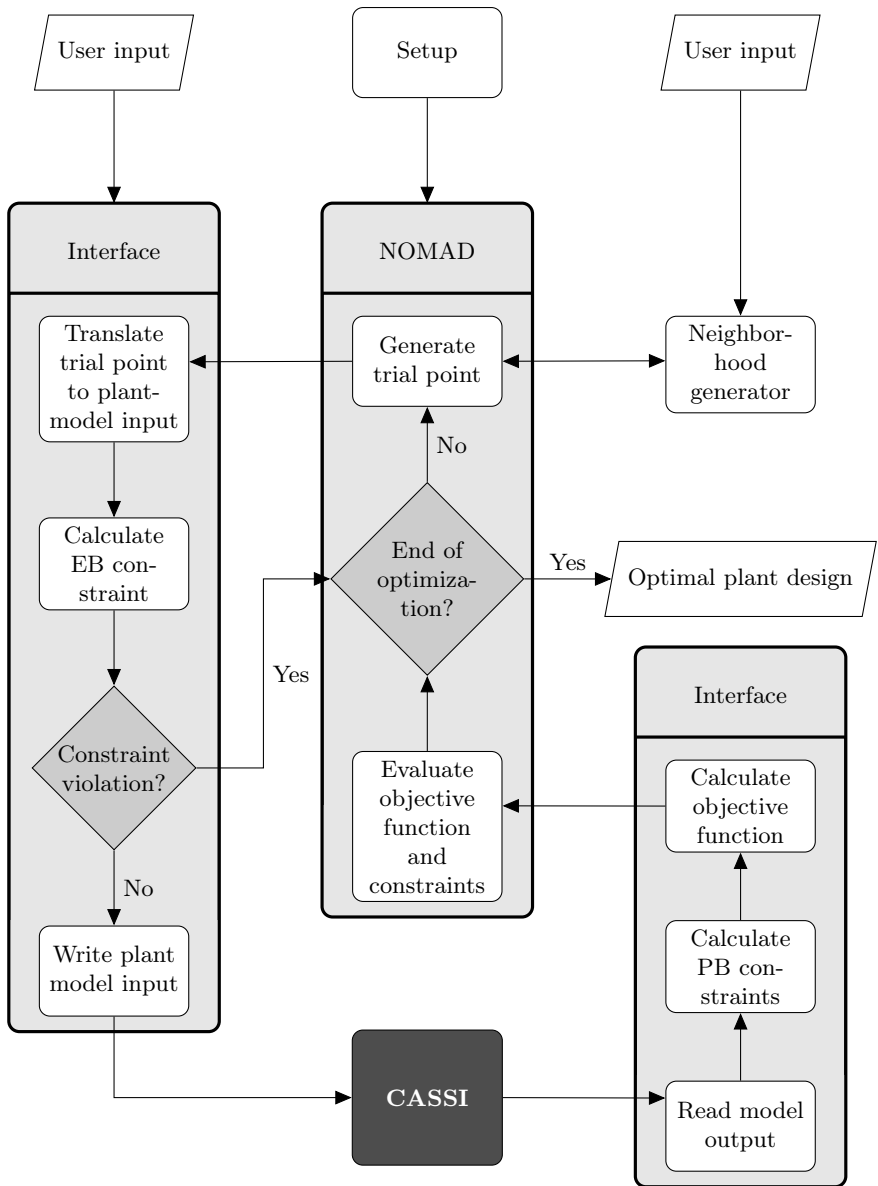


Figure 5.1: Flow chart of the AA-CAES design tool showing the coupling between NOMAD and CASSI.

5.3 Formulation of optimization problems

The optimization problems solved in this work use the TES-A and TES-M models in CASSI to generate Pareto fronts for the objective function composed of the plant efficiency and capital costs, defined as

$$f(x) = \sum_{i=1}^2 w_i f_i(x) = w_1 \frac{C_{\text{plant}}}{C_{\text{norm}}} - w_2 \eta, \quad (5.7)$$

where w_i are the weights, C_{plant} denotes the plant costs, see eq. (5.1), C_{norm} is a reference cost value for the normalization of the system costs, and η the plant efficiency. To generate a Pareto front, multiple optimization runs have to be performed with $0 \leq w_1 \leq 1$, where $w_2 = 1 - w_1$. A constraint is added in all simulations, $E_{\text{el,gen}} \geq 500$ MWh. The design variables are defined in table 5.2, with overlapping bounds for the cavern pressures that are rejected by an EB if the trial points do not satisfy $p_{\text{lpcav}} \leq p_{\text{hpcav,min}} < p_{\text{hpcav,max}}$.

The fixed plant parameters are shown in table 5.3. Cycles are defined as C/D without idle periods, and the charging and discharging was stopped when the respective target pressures of the trial point were reached. The plant simulations of each trial point were run until QSS was reached, defined by a relative change in the cavern temperatures and pressures smaller than 10^{-7} .

The compressor and turbine efficiencies were modeled using two representations of performance maps. The first consists of operating bounds with constant efficiencies and the simulations were performed for TES-A and

Table 5.2: Design variables for the optimization simulations.

Design variable	Lower bound	Upper bound	Starting point
$p_{\text{hpcav,min}}$	5 bar	100 bar	80 bar
$p_{\text{hpcav,max}}$	5 bar	100 bar	100 bar
p_{lpcav}	5 bar	100 bar	9 bar
l_{hpcav}	1 m	10 000 m	2600 m

Table 5.3: Fixed plant parameters used in the optimization simulations.

Quantity	Symbol	Value
Mass flow rate	\dot{m}_c, \dot{m}_d	200 kg/s
Ambient pressure	p_{amb}	1 atm
Ambient temperature	T_{amb}	20 °C
HX target temperatures	T_3, T_6, T_{3-d}	20 °C
Cavern diameters	D_{cav}	10 m
LP cavern length	$l_{\text{lp cav}}$	254.7 m
Motor & generator efficiency	$\eta_{\text{mot}}, \eta_{\text{gen}}$	0.98
Compressor & turbine mech. efficiency	η_m	0.98

TES-M. The bounds for the compressors are shown in figs. 5.2 and 5.3 and constant polytropic efficiencies of $\eta_{p,\text{lpc}} = 0.83$ and $\eta_{p,\text{hpc}} = 0.81$ were used. Constant polytropic turbine efficiencies of $\eta_{p,\text{lpt}} = 0.91$ and $\eta_{p,\text{hpt}} = 0.87$ were used for the bounds $250\text{ °C} \leq T_{t,\text{in}} \leq 527\text{ °C}$ and $6 \leq \pi_t \leq 12$, applying to HPT and LPT.

The second definition consists of variable efficiency maps that were used for simulations with TES-M. The compressor maps including the bounds are shown in figs. 5.2 and 5.3. The compressor efficiencies were modeled using surface polynomials of order five in both the mass flow rate and the pressure ratio. The turbines were modeled using the same bounds as for the constant-efficiency simulations, with efficiency polynomials described as

$$\eta_{\text{lpt}}(T_{\text{lpt},\text{in}}) = 0.911 + 0.008 \cdot T_{\text{lpt},\text{in}} - 0.006 \cdot T_{\text{lpt},\text{in}}^2 \quad (5.8)$$

$$\eta_{\text{hpt}}(T_{\text{hpt},\text{in}}, \pi_{\text{hpt}}) = 0.870 + 0.002 \cdot T_{\text{hpt},\text{in}} - 0.002 \cdot \pi_{\text{hpt}}. \quad (5.9)$$

The efficiency maps were extracted, simplified, and generalized from real turbomachinery data supplied by a project partner. The real data is confidential, which is why it had to be changed.

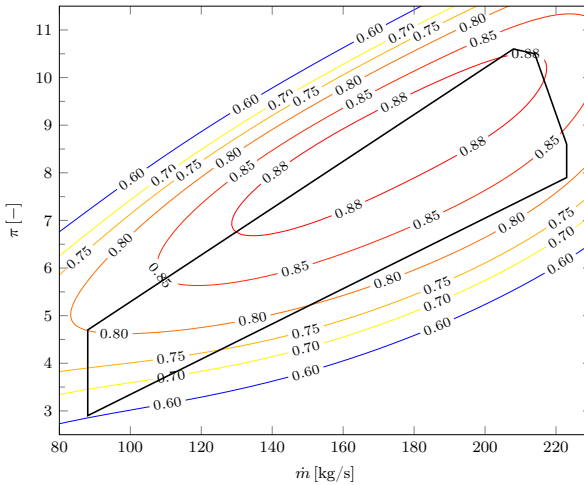


Figure 5.2: Variable efficiency map of the LPC, defined as polynomial surface function, including operating bounds (black lines).

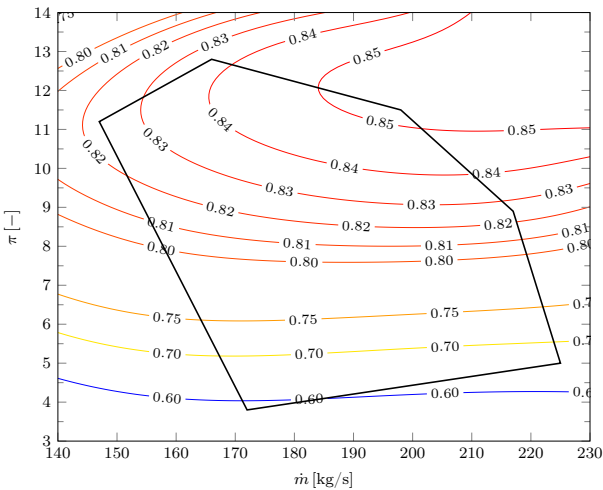


Figure 5.3: Variable efficiency map of the HPC, defined as polynomial surface function, including operating bounds (black lines).

5.4 Results

5.4.1 Verification

A verification, checking whether the optimizer would find the correct solution when the minimum and maximum are known, was performed using the analytical efficiency definition for the two-stage plant given by eq. (3.60). Three cases, where the optimizer was set up to find the maximum and minimum efficiencies, were defined to verify the functionality of the optimizer and increase the trustworthiness of more complex simulations and their results. The cases were run for three values of $p_{\text{hpcav,max}}/p_{\text{hpcav,min}}$, and constant $p_{\text{hpcav,max}}/p_{\text{atm}} = 100$. The optimizer was allowed to set the pressure in the LP cavern within $1.01 \leq p_{\text{lp cav}}/p_{\text{atm}} \leq p_{\text{hpcav,min}}/p_{\text{atm}}$. Figure 5.4 shows the results of the verification study. The minima and maxima, indicated by the three marker types (one type for each case), match well with the theory, the maximum relative difference is about $3 \cdot 10^{-4}$.

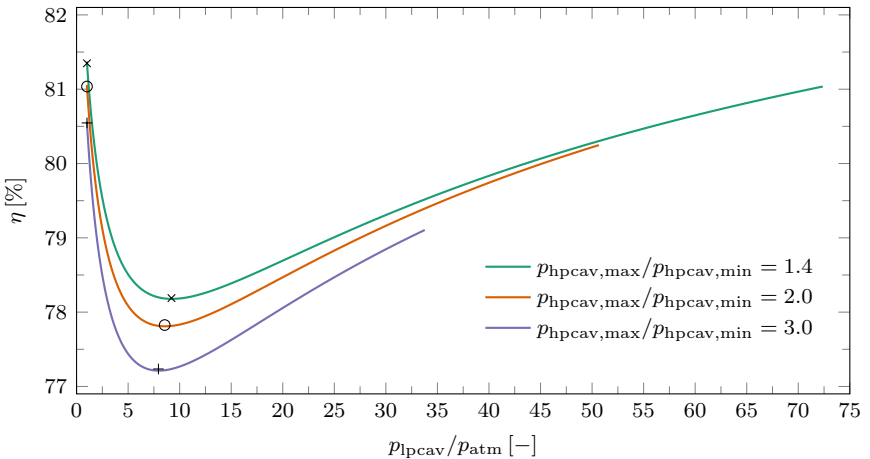


Figure 5.4: Verification results showing the efficiency curves defined by eq. (3.60), and the maximum and minimum efficiency found by NOMAD. The three marker types indicate the maximum and minimum for each case.

5.4.2 Constant efficiencies

The resulting Pareto fronts of the optimization simulations using TES-A and constant turbomachine efficiencies with operating bounds are shown in fig. 5.5. The simulations were performed for $0.0 \leq w_1 \leq 1.0$ with steps of 0.01 for $0.0 \leq w_1 \leq 0.1$ and steps of 0.1 for $0.1 \leq w_1 \leq 1.0$ and five time steps ranging from 5 s to 100 s. The results show a weak dependence of the plant costs for lower efficiencies ranging from 72.8% to 73.6%, after which large cost increases are necessary to achieve diminishing efficiency gains.

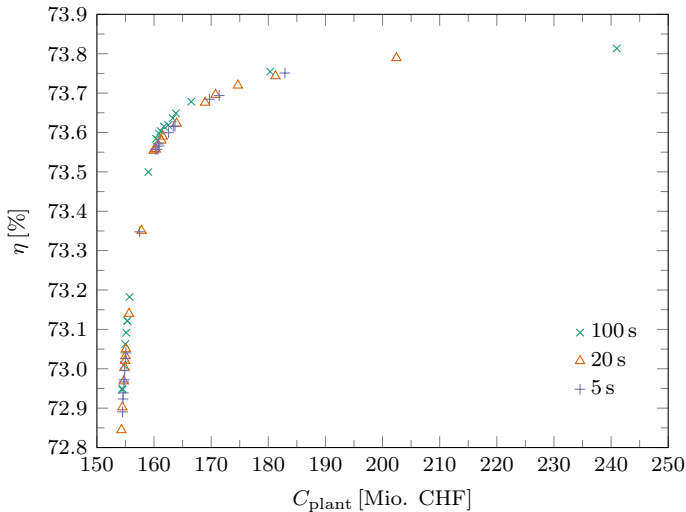


Figure 5.5: Pareto front of the optimizations using TES-A and constant efficiencies with operating bounds.

Table 5.4 shows selected results from the Pareto front and illustrates the large increase in costs, once efficiency is weighted with $w_2 \geq 0.95$. The constraint for $E_{\text{el,gen}} \geq 500$ MWh is approached for all points, except for $w_1 = 0$ which makes sense because for maximum efficiency, the energy storage capacity of the plant has no direct effect. The main factor driving the efficiency is a low $p_{\text{hpcav,max}}/p_{\text{hpcav,min}}$, which seems to make it difficult to for

Table 5.4: Selected results from the Pareto front with $\Delta t = 5$ s from fig. 5.5 using TES-A and constant efficiencies.

w_1	η	C_{plant}	V_{hpcav}	$C_{\text{cav}}/C_{\text{plant}}$	$E_{\text{el,gen}}$
[–]	[%]	[Mio. CHF]	[m ³]	[%]	[MWh]
0.00	73.82	264.7	628 320	47.2	567.2
0.01	73.75	182.9	219 510	23.9	500.6
0.05	73.60	162.5	122 170	15.0	500.0
0.10	73.56	160.2	110 250	13.7	500.1
0.40	72.97	154.7	108 190	13.9	500.0
0.60	73.02	155.0	103 650	13.3	500.1
0.80	72.97	154.8	107 750	13.9	500.0
1.00	72.94	154.6	110 360	14.2	500.0

the optimizer in the given case to hit the capacity target. For $0.05 \leq w_1 \leq 1.0$ the cost and efficiency are very stable, indicating that for these simulation conditions a wide range of potential plant designs is possible.

Table 5.5 shows the HP cavern cut-off pressures and the LP cavern pressures for selected weights w_1 . The results show the reason for the increasing cavern volume for small w_1 , which lies in the decreasing operating pressure range of the HP cavern. An interesting result is indicated by values of w_1 close to one, where high pressure ratios increase the energy density of the plant, but also lower maximum HP cavern pressures are chosen by the optimizer. These results are supported by the analytical plant model described in chapter 3.

The resulting Pareto fronts of the optimization simulations using TES-M and constant turbomachine efficiencies with operating bounds are shown in fig. 5.6. The simulations were performed for $0.0 \leq w_1 \leq 1.0$ with steps of 0.01 for $0.0 \leq w_1 \leq 0.1$ and steps of 0.1 for $0.1 \leq w_1 \leq 1.0$ and three time steps ranging from 5 s to 50 s. The results show a weak dependence of the plant costs for lower efficiencies ranging from 73.0% to 73.7%, after which large cost increases are necessary to achieve diminishing efficiency

Table 5.5: Selected optimal design-point pressure values of the Pareto front with $\Delta t = 5$ s from fig. 5.5 using TES-A and constant efficiencies.

w_1 [—]	$p_{\text{hpcav,max}}$ [bar]	$p_{\text{hpcav,min}}$ [bar]	p_{lpcav} [bar]
0.00	99.98	93.02	10.34
0.01	99.99	82.06	10.34
0.05	99.08	65.74	10.34
0.10	99.61	62.42	10.34
0.40	92.42	46.68	7.78
0.60	95.92	48.19	8.03
0.80	92.67	46.82	7.80
1.00	87.65	45.99	7.67

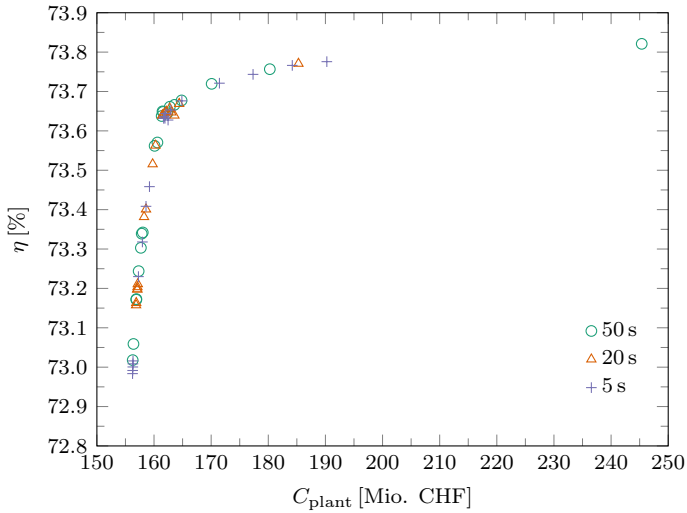


Figure 5.6: Pareto front of the optimizations using TES-M and constant efficiencies with operating bounds.

gains. TES-M gives generally higher plant efficiencies because no exergy is lost in this simplified TES model.

Table 5.6: Selected results from the Pareto front with $\Delta t = 5$ s from fig. 5.6 using TES-M and constant efficiencies.

w_1 [–]	η [%]	C_{plant} [Mio. CHF]	V_{hpcav} [m ³]	$C_{\text{cav}}/C_{\text{plant}}$ [%]	$E_{\text{el,gen}}$ [MWh]
0.00	73.78	190.24	253 151	26.5	513.4
0.01	73.77	162.9	222 788	24.1	500.2
0.05	73.65	162.5	117 022	14.3	500.0
0.10	73.63	161.8	111 945	13.8	500.0
0.40	73.32	158.0	100 041	12.6	500.0
0.60	72.99	156.3	118 675	15.1	500.1
0.80	73.01	156.3	116 518	14.8	500.0
1.00	72.98	156.2	119 392	15.2	500.0

Table 5.6 shows selected results from the Pareto front and illustrates the large increase in costs, once efficiency is weighted with $w_2 \geq 0.95$. Otherwise, the same trends described for the simulations with TES-A apply including the optimal design-point pressure values.

5.4.3 Variable efficiencies

The resulting Pareto fronts of the optimization simulations using TES-M and efficiency maps are shown in fig. 5.7. The simulations were performed for $0.0 \leq w_1 \leq 1.0$ with steps of 0.01 for $0.0 \leq w_1 \leq 0.1$ and steps of 0.1 for $0.1 \leq w_1 \leq 1.0$ and three time steps ranging from 50 s to 5 s. The results show generally higher efficiencies than the constant efficiency simulations, with efficiencies ranging from 74.6% to 76.8%, but a higher spread of the plant efficiency between the highest and lowest values.

Table 5.7 shows selected results of the Pareto front from fig. 5.7. The constraint of $E_{\text{el,gen}} \geq 500$ MWh has been reached for all presented simula-

tions. The highest efficiency is only 2.3% higher than the lowest efficiency, while the relative difference in plant cost is about 48%.

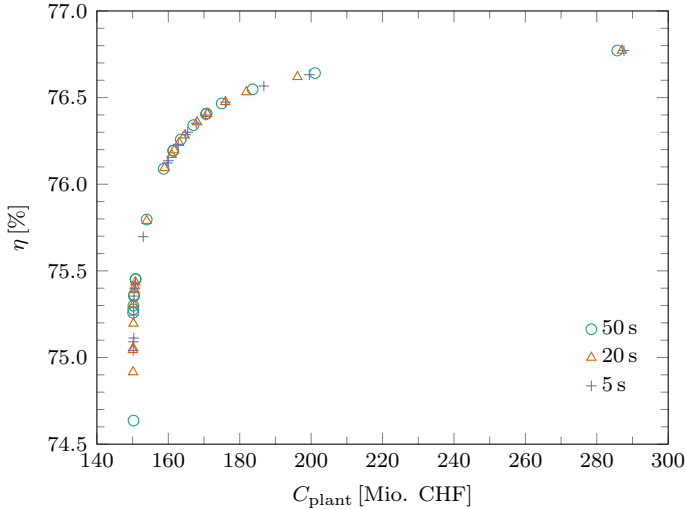


Figure 5.7: Pareto front of the optimizations using TES-M and efficiency maps.

Table 5.8 shows the HP cavern cut-off pressures and the LP cavern pressures for selected weights w_1 . The results show the reason for the increasing cavern volume for small w_1 , which lies in the decreasing operating pressure range of the HP cavern. Interestingly for large values of w_1 , the high pressure ratios still increase the energy density of the plant, but lower maximum HP cavern pressures are not clearly visible as compared to the TES-A simulations, see table 5.5. This result is only partly explained by the analytical plant model described in chapter 3 and illustrates the importance of including more accurate component properties such as turbomachine efficiency maps.

Table 5.7: Selected results from the Pareto front with $\Delta t = 5$ s from fig. 5.7 using TES-M and variable efficiencies.

w_1 [—]	η [%]	C_{plant} [Mio. CHF]	V_{hpcav} [m ³]	$C_{\text{cav}}/C_{\text{plant}}$ [%]	$E_{\text{el,gen}}$ [MWh]
0.00	76.77	287.6	785 342	54.3	500.0
0.01	76.63	199.5	342 687	34.2	500.0
0.05	76.35	167.8	183 425	21.8	500.0
0.10	76.12	159.7	142 499	17.8	500.0
0.40	75.40	150.6	96 381	12.7	500.0
0.60	75.11	150.3	97 512	12.9	500.0
0.80	75.24	150.3	95 589	12.7	500.0
1.00	75.04	150.2	95 424	12.6	500.0

Table 5.8: Selected optimal design-point pressure values of the Pareto front with $\Delta t = 5$ s from fig. 5.7 using TES-M and variable efficiencies.

w_1 [—]	$p_{\text{hpcav,max}}$ [bar]	$p_{\text{hpcav,min}}$ [bar]	p_{ipcav} [bar]
0.00	100.00	94.90	9.60
0.01	99.99	88.20	9.56
0.05	100.00	79.16	9.50
0.10	100.00	70.81	9.44
0.40	99.99	55.64	9.27
0.60	97.15	52.86	8.81
0.80	98.83	53.86	8.98
1.00	97.34	52.03	8.67

5.5 Summary, conclusions, and future work

The connection of the newly developed plant model CASSI with the NOMAD optimization software was presented and the results in this chapter provided an insight into the possibilities that unfold using this approach. The results showed that considerable plant cost reductions of up to 48% were feasible, while the exergy efficiency only decreased from 76.8% to 75%. The inclusion of turbomachinery efficiency maps in the simulations showed how important the inclusion of more complexity is, because the results predicted a different optimum in terms of pressure ratios for reaching maximum energy density compared to the analytical plant model presented in chapter 3.

Future work should conduct more complex optimization simulations, including single-tank TES and MTES geometry and insulation-layer and material optimizations. A more complex cost model, for example including construction costs or more detailed component costs, would also give the analysis more credibility. Finally the optimization of plants subjected to variable operating conditions should be performed, as this is the area where it is least obvious how suitable plant designs should look like. The inclusion of profitability calculations would be extremely valuable, but requires assumptions regarding energy prices and a dispatch optimization. Currently, the co-optimization of dispatch and plant design does not seem feasible but an iterative process between the two would make sense.

CONCLUSIONS AND RECOMMENDATIONS FOR FUTURE WORK

This thesis investigated analytical and numerical models describing AA-CAES plants, thermal-energy storage, and the application of numerical optimization algorithms to enable automated system designs.

6.1 Multi-tank thermal-energy storage

Multi-tank packed-bed thermocline TES systems were investigated, presented in chapter 2, as a potential practical implementation of thermocline control. The results support the conclusion that MTTES and TCC outperform conventional single-tank TES systems in terms of system size (2.5 times smaller volume) for the same temperature drop during discharging and material costs (1.5 times lower), while the exergy efficiency decreases from over 98% to less than 92%. The main advantage of MTTES systems using mixing TCC lies in their ability to control the outflow temperatures, which

especially during discharging is very valuable for AA-CAES (but also for other electricity storage technologies using TES, (for example pumped thermal electricity storage). The MTTES approach also provides a path towards a simple implementation of TCC and additionally enables TES units to become standardized and modular systems could be possible. This presented work advanced the understanding of MTTES applying TCC in terms of exergy efficiency (including pressure and thermal losses, which had not been found in such detail in previous works), and considerations towards the implementation in AA-CAES where temperature and therefore power output control is essential.

Future work should include the piping and valve thermal and pressure losses, and their costs to complete the MTTES system analysis. This could be achieved by a simple zero-dimensional representation of the pipes, applying pressure loss calculations using empirical correlations and calculating the thermal losses with a resistance model. When doing so, it would also make sense to think about how to place the TES next to each other, for example having the hottest tank surrounded by cooler tanks would be beneficial regarding thermal losses, opposed to exposing all of them to the cavern air.

Experimental work should be performed to prove that temperature control can be realized, which would include building a suitable valve system and a control system. The focus for the control system should lie on a low-cost application using as few sensors as possible (for example a sensor at the in- and outlets of each tank only). A lab-scale prototype is a feasible solution where several small packed-bed tanks could be connected and temperatures could be kept below 100 °C, if necessary. The direct realization of a pilot-scale MTTES system is also thinkable, because the TES itself have been experimentally tested at this scale, and the connection elements could be tested separately.

The presented MTTES analysis could also be extended to include higher charging temperatures and include PCM storage modules, the latter could be used as high-temperature booster storages, providing constant outflow temperatures, or low-temperature heat dump storages, which could decrease

the required maximum power of heat exchangers that perform aftercooling during charging.

The large number of design variables make numerical optimization algorithms an attractive approach for automated MTES design. While the topic of numerical optimization is covered in chapter 5, more work on this topic is justified, especially regarding the optimization the TES geometry, and insulation layer materials and thicknesses. The tool to perform such optimizations has been presented in this work, but further work is necessary to make the optimizations, including thermal losses, faster.

6.2 Analytical modeling of AA-CAES

An analytical AA-CAES plant model was developed and presented in chapter 3. The model was developed by solving the time integrals describing the quasi-steady state of the plant. All components are considered to be adiabatic and have no pressure losses. The TES is modeled to deliver constant outflow temperatures during charging and discharging. The resulting model is complementary to numerical models, as it enables physical insights and can be used to predict the plant performance, size components, and verify codes. This model is a big step towards the better understanding of AA-CAES plants physics and makes it possible to predict the performance of plant designs reliably and fast. Previously developed models often lacked the consideration of the sliding pressure inside the CAES cavern, making accurate predictions impossible. With this contribution, a more complete theoretical description of AA-CAES plants was developed.

Further work should focus on continuing the model development by extending the theory to include pressure and thermal losses of the TES and caverns. Thermal losses of the TES could be represented by a constant storage efficiency, while the pressure losses could be defined as a constant depending on the TES geometry. For the cavern losses, similar constant loss mechanisms could be possible, for example the cavern temperature could be set to a user-defined cavern wall temperature that is lower than $T_{\text{hpcav,max}}$

after charging, resulting in a pressure drop between charging and discharging. Including a representation of the idle phase, calculating the thermal and pressure losses of the TES and cavern, could also be investigated, however the algebra involved could prove prohibitive to such an approach.

The model could quite easily be extended to also provide the performance equations for polytropic efficiencies, a process that was started, but is not completed yet. Furthermore, the model should be extended to provide all equations shown for the one- and two-stage model for plants with N-stages.

The application of the model is also a region where further work is justified. It would be interesting to analyze quasi-isothermal concepts with the N-stage model, and also to investigate the performance of small-scale AA-CAES concepts that generally use lower storage temperatures.

Lastly, the model could be completed with a simple cost estimation of the components, based on the sizing equations provided in the model.

6.3 Numerical modeling of AA-CAES

In chapter 4, a new numerical AA-CAES plant model was presented, including an MTTES implementation using mixing TCC. Quasi-steady state analyses with a focus on constant power outputs, and the plant performance under realistic plant operating profiles were assessed. The results show that AA-CAES plants can generally operate at quasi-steady-state using MTTES and mixing TCC, providing constant power output at efficiencies above 69%. The simulations under variable operating conditions showed that a plant with MTTES was able to follow a load curve over 98% of the time, with power qualities of 100% and periodic efficiencies of about 66.5%. The developed model and the performed simulations provide new insights into the performance potential of AA-CAES plants providing constant power output during discharging using MTTES with mixing TCC as presented in chapter 2 which has previously not been done. The simulations on dynamic operation of the plant were provide new and unique insights at using the MTTES control approach to follow a grid load and show the importance of

including such dynamic operating conditions in future works on the topic as they influence the plant requirements and design.

The inclusion of temperature- and pressure-dependent thermophysical air properties, and the inclusion of a humid-air model are certainly very important additions that could be implemented in the future. Wolf [42] showed that the most important influence of humid air is visible during the charging period of a TES at the cold outlet where condensation occurs, which showed to change the stored heat by the TES of up to 10%. Furthermore, it would be interesting to know how much liquid water would occur, as this impacts the design of the draining mechanism.

The inclusion of efficiency maps has been presented briefly in chapter 5, but further work should focus on finding more data on efficiency maps and automatic scaling of these maps to make it possible to use a map for a multitude of compressor and turbine power ratings, which is a necessity for numerical optimization. Further work should also perform a detailed analysis of the plant simulation including efficiency maps, as this will provide more insights into the operating boundaries that such a plant faces.

The load-following ability and power quality of the plant should be further analyzed for variable operating conditions. To increase the power ranges in which the plant can operate, multiple parallel compressor and turbine trains are a possibility, but also other balancing technologies, such as flywheels, batteries, or super-capacitors should be evaluated.

It has been shown that the thermal losses in the cavern lead to a decrease in the maximum storage pressure during idling phases, leading to a decrease in power output. To cover this process more accurately, the cavern model could be extended to a discretized representation of the cavern walls, enabling also the possibility of recovering some of the lost heat during discharging when the cavern air cools down. A temperature- and mass-flow-dependent cavern wall heat-transfer coefficient could also help to increase the accuracy of the plant model, but to do this accurately the heat-transfer mechanisms in the plant have to be understood and analyzed in detail.

Finally, the plant model should be used to design a first demonstration

plant. Once experimental data is available, the model can be validated, which is an important open point in this work. Should it not be possible to build an AA-CAES demonstration plant, the model's suitability to assess small-scale CAES systems could be explored, because it is more likely that a pilot plant in the order of 100 kW could be built within a research project and used for the validation of the code.

6.4 Numerical optimization

Chapter 5 showed first results of the newly developed plant optimization tool. The optimizer was allowed to adjust the HP and LP cavern pressure ratios, and the cavern length, with the task to minimize the weighted objective function for plant costs and efficiency. The resulting Pareto fronts showed that the plant costs could be reduced up to 48%, while the exergy efficiency only decreased from 76.8% to 75%. These results are a clear indication for the value of applying numerical optimization methods to the design of MTTES and AA-CAES. The presented and developed models in this work enable such analyses in an efficient manner and provide guidelines for future works on this topic regarding the required detail of the models and the methodology to follow.

Future work should increase the complexity of the conducted simulations, including the quasi-one dimensional TES model enabling the optimization of MTTES geometry and insulation layer thicknesses and material choices. By including a more complex cost model and including profitability calculations of the plant, the results would gain credibility and the design tool could be used for the design of real plant projects. Finally, the inclusion of variable operating conditions would enable new insights because it is still unclear how this affects the plant design.

NUMERICAL MODEL

The TES simulations were performed with the quasi-one-dimensional heat-transfer model described by Geissbühler et al. [29], around which a MATLAB routine was wrapped to enable the model to be used for MTTES systems. The resulting simulation process is depicted in fig. A.1 and can be divided into three components:

- (1) The inputs, see the red box in fig. A.1, include the number of tanks, the total system volume, the tank aspect ratios, the operating conditions (the durations of the charging, discharging, and idle phases; adiabatic or diabatic conditions), the operating mode (serial or extraction/mixing TCC), the target outflow temperatures for charging and discharging, thermophysical properties of the HTF and the storage material, and the convergence criteria.
- (2) The MATLAB routine consists of five nested loops:
 - Iteration for the target temperature: Because $\Delta\tilde{T}_{d,\text{out,max}}$ is not known a priori, it has to be found iteratively. The iteration

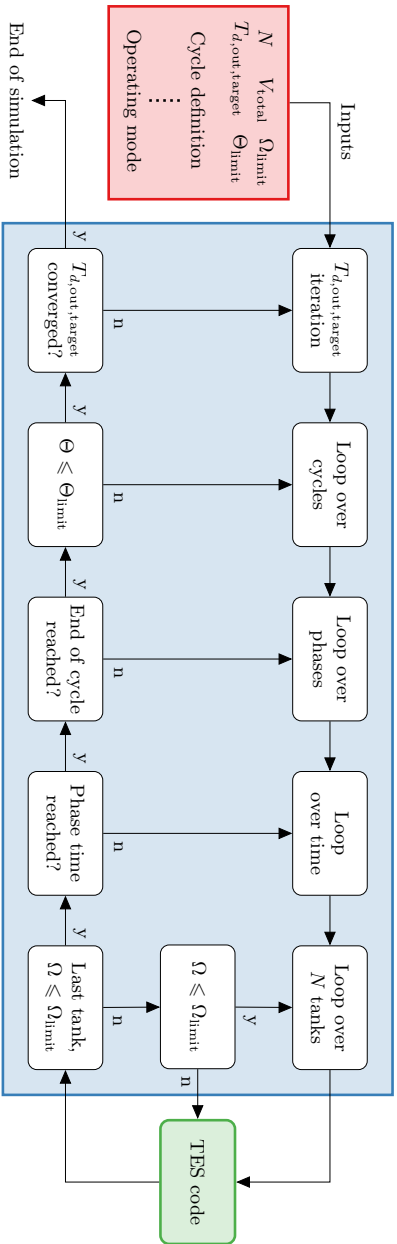


Figure A.1: Schematic depiction of the main components of the simulation process for MTTES systems.

increases/decreases $T_{d,\text{out},\text{target}}$ if $T_{d,\text{out}}(t_{d,\text{end}})$ is larger/smaller than $T_{d,\text{out},\text{target}}$. If at the end of discharging, $T_{d,\text{out}}$ is lower than $T_{d,\text{out},\text{target}}$, the target temperature is increased, and decreased if $T_{d,\text{out}}$ is higher than $T_{d,\text{out},\text{target}}$. This iteration is performed in step sizes of 0.1% for $\Delta\tilde{T}_{d,\text{out},\text{max}}$ for all simulations conducted in this study. (It should be noted that the target outflow temperature for the charging phase was set such that the relative increase in the outflow temperature during charging is equal to the relative decrease in the outflow temperature during discharging. Whether the target temperature for the charging phase could actually be met was not checked because the focus of this work is on the outflow temperatures at the end of the discharging phase.)

- Loop over cycles: Cycles are simulated until a quasi-steady state has been reached, which is judged to have occurred when

$$\Theta = \max_j \left(\frac{T(x_j, t_{d,\text{end}}^n) - T(x_j, t_{d,\text{end}}^{n-1})}{T_{c,\text{in}} - T_{d,\text{in}}} \right) \leq \Theta_{\text{limit}}, \quad (\text{A.1})$$

where x_j are the locations of the temperatures in the grid and $t_{d,\text{end}}^n$ and $t_{d,\text{end}}^{n-1}$ are the end times of the discharging phases of two consecutive cycles. The tolerance was set to $\Theta_{\text{limit}} = 10^{-3}$ for all simulations.

- Loop over phases: The sequences of phases are charging/discharging for adiabatic and charging/idle/discharging/idle for diabatic conditions.
- Loop over time: The duration of each phase is resolved with constant time steps.
- Loop over tanks: The tanks are simulated by calling the TES code in ascending order for charging and idle phases and in descending order for discharging phases. The loop is exited if all tanks have

been simulated and $\Omega \leq \Omega_{\text{limit}}$, where

$$\Omega = \begin{cases} \max_k |T_{d,\text{out,target}}(t^k) - T_{d,\text{out}}(t^k)| & \text{for discharging,} \\ \max_k |T_{c,\text{out,target}}(t^k) - T_{c,\text{out}}(t^k)| & \text{for charging,} \end{cases} \quad (\text{A.2})$$

where Ω_{limit} is a user-specified tolerance that was set to 10^{-4} for all simulations, and t^k are the discrete times during a phase. (The reason why the tanks have to be simulated repeatedly is that when the outflows from two tanks are being mixed, for example, the tank with the increasing mass flow rate has a non-constant outflow temperature that is unknown upon the first execution, leading to $T_{d,\text{out}}(t^k)$ deviating from $T_{d,\text{out,target}}(t^k)$.)

- (3) The TES code [29] is called for each time step and TES tank, with the MATLAB routine reading the relevant outputs and handling the connections between the tanks. For all simulations, the time step was 10 s and the grid spacing was 0.05 m. Grid- and time-refinement studies showed that the results presented in this work can be considered to be independent of the grid spacing and the time step.

The MTTES simulation process depicted in fig. A.1 was verified by comparing the simulations of adiabatic cylindrical MTTES, where a TES unit was sliced into up to four tanks, with simulations of the single tank conducted with the previously verified and validated standalone TES code, see Geissbühler et al. [29]. A verification for diabatic surroundings was not performed because the temperatures cannot be similar due to the increased thermal losses caused by the top/bottom surfaces of the multi-tank systems. The largest difference between the thermoclines of the multi- and the single-tank simulations was less than 0.05% of the relative temperature differences between the quasi-steady thermoclines evaluated at the ends of charging and discharging.

LIST OF FIGURES

- 2.1 Two-tank TES system for (a) parallel and (b) serial operation during charging (left) and discharging (right). The flow paths are indicated by the red and blue arrows. The system inflow and outflow streams are depicted by purple arrows. 16
- 2.2 Charging and discharging of an MTTES system consisting of four tanks with extraction TCC. In subfigure (a), the charging and discharging paths are indicated by full and dashed lines, respectively, and red, blue, green, and orange lines representing the HTF flowing towards, through, and out of tanks one, two, three, and four, respectively. In subfigure (b), the top and bottom plots show the non-dimensional mass flows (same colors as in subfigure (a)) and the non-dimensional outflow temperatures (purple lines) as a function of non-dimensional time during discharging and charging, respectively. The plots in the middle show the thermoclines in the four tanks at the four times during charging and discharging that are indicated in the top and bottom plots. The dotted lines in subfigure (b) indicate the maximum allowable outflow temperatures. . . 23

- 2.3 Charging and discharging of an MTTES system consisting of four tanks with mixing TCC. In subfigure (a), the charging and discharging paths are indicated by full and dashed lines, respectively, and red, blue, green, and orange lines representing the HTF flowing towards, through, and out of tanks one, two, three, and four, respectively. In subfigure (b), the top and bottom plots show the non-dimensional mass flows (same colors as in subfigure (a)) and the non-dimensional outflow temperatures (purple lines) as a function of non-dimensional time during discharging and charging, respectively. The plots in the middle show the thermoclines in the four tanks at the three times during charging and discharging that are indicated in the top and bottom plots. The dotted lines in subfigure (b) indicate the maximum allowable outflow temperatures. 24
- 2.4 Schematic depiction of the tank geometry and the construction and insulation material layers. The materials and thicknesses of the layers are given in table 2.2. 30
- 2.5 Non-dimensional storage volume as a function of $\Delta\tilde{T}_{d,\text{out,max}}$ and N for adiabatic conditions. The behaviors of the multi-tank systems highlighted by the gray and orange disks are discussed in the text and shown in figs. 2.6 to 2.8, respectively. 33
- 2.6 Thermoclines at the ends of charging and discharging (bottom plot) and outflow temperatures during discharging (top four plots) for the four two-tank systems with the extraction method highlighted by the gray disk in fig. 2.5. The dashed line and the parentheses indicate the division into two tanks. 34
- 2.7 Thermoclines at the ends of charging and discharging (bottom plot) and outflow temperatures during discharging (top three plots) for the systems with equal \tilde{V} highlighted by the orange disks in fig. 2.5. The line colors match those in fig. 2.5. The breaks in the thermoclines indicate the division into tanks. 36

2.8	Thermoclines at the ends of charging and discharging (bottom plot) and outflow temperatures during discharging (top three plots) for the systems with similar $\Delta\tilde{T}_{d,\text{out,max}}$ highlighted by the orange disks in fig. 2.5. The line colors match those in fig. 2.5. The breaks in the thermoclines indicate the division into tanks.	37
2.9	Non-dimensional storage volume as a function of $\Delta\tilde{T}_{d,\text{out,max}}$ and N for diabatic conditions and the mixing method ($N > 1$). For the systems highlighted by the orange disks, additional information is provided in table 2.7 and the thermoclines and outflow temperatures during discharging are shown in fig. 2.12.	39
2.10	Exergy efficiency determined from eq. (2.31) as a function of $\Delta\tilde{T}_{d,\text{out,max}}$ and N for diabatic conditions and the mixing method ($N > 1$). For the systems highlighted by the orange disks, a breakdown of the exergy losses is presented in table 2.6.	40
2.11	Specific material costs as a function of $\Delta\tilde{T}_{d,\text{out,max}}$ and N for diabatic conditions and the mixing method ($N > 1$).	42
2.12	Thermoclines at the ends of charging and discharging (bottom plot) and outflow temperatures during discharging (top two plots) for the systems highlighted by the orange disks in fig. 2.9. The line colors match those in fig. 2.9. The breaks in the green lines indicate the division into two tanks.	43
3.1	Layout of plant with one-stage turbomachinery and state numbering.	54
3.2	$p_{\text{cav}}(t)/p_{\text{min}}$ as a function of time during charging and discharging, determined from eqs. (3.9) and (3.11), respectively, and the entropy during charging as a function of time for $p_{\text{cav,max}}/p_{\text{cav,min}} = 2$ and $\gamma = 1.4$. During discharging, $s_{\text{cav}}(t) = s_{\text{cav,min}}$	57
3.3	The function f_{η} given by eq. (3.28) as a function of $p_{\text{cav,max}}/p_{\text{cav,min}}$ and $p_{\text{cav,max}}/p_{\text{atm}}$ for $\eta_{s,c} = \eta_{s,t} = 0.85$ and $\gamma = 1.4$	61

- 3.4 The plant efficiency given by eq. (3.27) as a function of $p_{\text{cav,max}}/p_{\text{cav,min}}$ and $\eta_{s,c}$ and $\eta_{s,t}$ for $p_{\text{cav,max}}/p_{\text{atm}} = 100$, $\eta_{\text{mot}} = \eta_{\text{gen}} = \eta_{m,c} = \eta_{m,t} = 0.98$, and $\gamma = 1.4$ 62
- 3.5 $E_{\text{el,gen}}/p_{\text{cav,max}}V_{\text{cav}}$ given by eq. (3.29) as a function of $p_{\text{cav,max}}/p_{\text{cav,min}}$ and $p_{\text{cav,max}}/p_{\text{atm}}$ for $\eta_{\text{gen}} = \eta_{m,t} = 0.98$, $\eta_{s,c} = \eta_{s,t} = 0.85$, $T_3/T_{\text{atm}} = 1$, and $\gamma = 1.4$ 64
- 3.6 $E_{\text{el,gen}}/V_{\text{cav}}$ derived from eq. (3.29) as a function of $p_{\text{cav,max}}$ and $p_{\text{cav,max}}/p_{\text{cav,min}}$ for $p_{\text{atm}} = 1 \text{ atm}$, $\eta_{\text{gen}} = \eta_{m,t} = 0.98$, $\eta_{s,c} = \eta_{s,t} = 0.85$, $T_3/T_{\text{atm}} = 1$, and $\gamma = 1.4$ 66
- 3.7 V_{cav} required for $E_{\text{el,gen}} = 10 \text{ MWh}$ derived from eq. (3.29) as a function of $p_{\text{cav,max}}/p_{\text{cav,min}}$ and $p_{\text{cav,max}}/p_{\text{atm}}$ for $\eta_{s,c} = \eta_{s,t} = 0.85$, $\eta_{\text{gen}} = \eta_{m,t} = 0.98$, $T_3/T_{\text{atm}} = 1$, $p_{\text{atm}} = 1 \text{ atm}$, and $\gamma = 1.4$ 67
- 3.8 The relative error in the generated electrical energy defined by eq. (3.33) as a function of $p_{\text{cav,max}}/p_{\text{cav,min}}$ and $p_{\text{cav,max}}/p_{\text{atm}}$ for $\eta_{s,c} = 0.85$ and $\gamma = 1.4$. Note the unequal spacing of the isolines. 68
- 3.9 The compressor outflow temperature as a function of the pressure ratio for an inflow temperature of 15°C , $\eta_{s,c} = 0.85$, and $\gamma = 1.4$ 70
- 3.10 Layout of plant with two-stage turbomachinery and state numbering. 71
- 3.11 f_η given by eq. (3.61) as a function of $p_{\text{hpcav,max}}/p_{\text{hpcav,min}}$ and $p_{\text{hpcav,max}}/p_{\text{atm}}$ for selected values of $p_{\text{lpcav}}/p_{\text{atm}}$ and for $\eta_{s,\text{lpc}} = \eta_{s,\text{hpc}} = \eta_{s,\text{hpt}} = \eta_{s,\text{lpt}} = 0.85$, $T_3/T_{\text{atm}} = 1$, and $\gamma = 1.4$. Gray shading indicates areas where $p_{\text{hpcav,min}}/p_{\text{lpcav}} < 1$. 78
- 3.12 f_η given by eq. (3.61) as a function of $p_{\text{lpcav}}/p_{\text{atm}}$ and $p_{\text{hpcav,max}}/p_{\text{atm}}$ for selected values of $p_{\text{hpcav,max}}/p_{\text{hpcav,min}}$ and for $\eta_{s,\text{lpc}} = \eta_{s,\text{hpc}} = \eta_{s,\text{hpt}} = \eta_{s,\text{lpt}} = 0.85$, $T_3/T_{\text{atm}} = 1$, and $\gamma = 1.4$. Gray shading indicates areas where $p_{\text{hpcav,min}}/p_{\text{lpcav}} < 1$ 80

- 3.13 $E_{\text{el,gen}}/p_{\text{hpcav,max}}V_{\text{hpcav}}$ given by eq. (3.67) as a function of $p_{\text{hpcav,max}}/p_{\text{hpcav,min}}$ and $p_{\text{hpcav,max}}/p_{\text{atm}}$ for selected values of $p_{\text{lpcav}}/p_{\text{atm}}$ for $\eta_{s,\text{lpc}} = \eta_{s,\text{hpc}} = \eta_{s,\text{hpt}} = \eta_{s,\text{lpt}} = 0.85$, $\eta_{\text{gen}} = \eta_m = 0.98$, $T_3/T_6 = T_3/T_{\text{atm}} = 1$, and $\gamma = 1.4$. Gray shading indicates areas where $p_{\text{hpcav,min}}/p_{\text{lpcav}} < 1$ 85
- 3.14 V_{hpcav} required for $E_{\text{el,gen}} = 10$ MWh derived from eq. (3.67) as a function of $p_{\text{hpcav,max}}/p_{\text{hpcav,min}}$ and $p_{\text{hpcav,max}}/p_{\text{atm}}$ for $\eta_{s,\text{lpc}} = \eta_{s,\text{hpc}} = \eta_{s,\text{hpt}} = \eta_{s,\text{lpt}} = 0.85$, $\eta_{\text{gen}} = \eta_m = 0.98$, $T_3/T_6 = T_3/T_{\text{atm}} = 1$, and $\gamma = 1.4$ 86
- 3.15 Upper limit on $V_{\text{lpcav}}/V_{\text{hpcav}}$ given by eq. (3.74) that ensures inequality (3.71) as a function of $p_{\text{hpcav,max}}/p_{\text{hpcav,min}}$ and $p_{\text{hpcav,max}}/p_{\text{atm}}$ for $p_{\text{lpcav}}/p_{\text{atm}} = 10$ and $T_6/T_3 = 1$ 88
- 3.16 Enthalpy flows during the charging phase (left) and discharging phase (right). 89
- 3.17 The fractions of energy stored in the high-pressure cavern, the high-pressure TES, and the low-pressure TES, given by eqs. (3.75) to (3.77), as a function of $p_{\text{hpcav,max}}/p_{\text{atm}}$ and $p_{\text{hpcav,max}}/p_{\text{hpcav,min}}$ for $\eta_{s,\text{lpc}} = \eta_{s,\text{hpc}} = 0.85$, $p_{\text{lpcav}}/p_{\text{atm}} = 10$, $T_3/T_{\text{atm}} = T_6/T_3 = 1$, and $\gamma = 1.4$ 91
- 3.18 The fractions of energy stored in the high-pressure cavern, the high-pressure TES, and the low-pressure TES and the fraction of energy rejected by the heat exchanger, given by eqs. (3.78) to (3.81), as a function of $p_{\text{hpcav,max}}/p_{\text{atm}}$ and $p_{\text{hpcav,max}}/p_{\text{hpcav,min}}$ for $\eta_{s,\text{lpc}} = \eta_{s,\text{hpc}} = \eta_{s,\text{hpt}} = 0.85$, $p_{\text{lpcav}}/p_{\text{atm}} = 10$, $T_3/T_{\text{atm}} = T_6/T_3 = 1$, and $\gamma = 1.4$ 94
- 3.19 The relative error in the total turbine work defined by eq. (3.84) as a function of $p_{\text{hpcav,max}}/p_{\text{hpcav,min}}$, $p_{\text{hpcav,max}}/p_{\text{atm}}$, and $p_{\text{lpcav}}/p_{\text{atm}}$ for $\eta_{s,\text{hpc}} = \eta_{s,\text{lpc}} = 0.85$, $\eta_{s,\text{hpt}} = \eta_{s,\text{lpt}}$, $T_3/T_{\text{atm}} = 1$, and $\gamma = 1.4$. Note the unequal spacing of the isolines below $1 \cdot 10^{-3}$ 96

4.1	Schematic showing the main components of the AA-CAES plant. Red arrows indicate the charging process while the blue arrows indicate the discharging process.	112
4.2	Order-verification study of the numerical model showing the relative error E defined by eq. (4.19) as a function of the time step for several values of $p_{\text{hpcav,max}}/p_{\text{hpcav,min}}$ and $p_{\text{hpcav,max}}/p_{\text{atm}}$ and for $p_{\text{ipcav}}/p_{\text{atm}} = 10$	120
4.3	Results for QSS plant operation, indicating turbomachinery in- and outflow temperatures, in- and outflow pressures, and power in- and output shown for charging and discharging.	121
4.4	Thermoclines as a function of the non-dimensional TES height in the low- and high-pressure caverns at the QSS, left and right, at the end of charging (red) and discharging (blue), respectively.	122
4.5	Pressure and temperature evolution in the low- and high-pressure caverns over the 24 hour C/I/D/I cycle.	123
4.6	Results for QSS constant power plant operation, indicating turbomachinery in- and outflow temperatures, in- and outflow pressures, and power in- and output shown for charging and discharging.	127
4.7	Mass flow and outflow temperature evolutions for charging (bottom) and discharging (top) for the MTTES system in the LP cavern, with the thermoclines of the two TES tanks at the end of charging and discharging (middle). The colors of the thermoclines match the colors of the corresponding mass flow rates and the black dashed line indicates the overall mass flow rate of the system.	129

-
- 4.8 Mass flow and outflow temperature evolutions for charging (bottom) and discharging (top) for the MTTES system in the HP cavern, with the thermoclines of the three TES tanks at the end of charging and discharging (middle). The colors of the thermoclines match the colors of the corresponding mass flow rates and the black dashed line indicates the overall mass flow rate of the system. 130
- 4.9 Sankey diagram showing the charging exergy flows of the diabatic, single-tank QSS simulation with KPIs presented in table 4.4. The total exergy values calculated with eq. (4.21) were multiplied by a factor of 10 to make the diagram more readable. This means that the sum of the electrical exergy flowing into the motors of LPC and HPC correspond to $E_{el,mot}$ from table 4.4. 132
- 4.10 Sankey diagram showing the charging exergy flows of the diabatic, MTTES QSS simulation with KPIs presented in table 4.6. The total exergy values calculated with eq. (4.21) were multiplied by a factor of 10 to make the diagram more readable. 133
- 4.11 Sankey diagram showing the discharging exergy flows of the diabatic, single-tank QSS simulation with KPIs presented in table 4.4. The total exergy values calculated with eq. (4.21) were multiplied by a factor of 10 to make the diagram more readable. This means that the sum of the electrical exergy flowing into the motors of LPC and HPC correspond to $E_{el,mot}$ from table 4.4. 134
- 4.12 Sankey diagram showing the discharging exergy flows of the diabatic, MTTES QSS simulation with KPIs presented in table 4.6. The total exergy values calculated with eq. (4.21) were multiplied by a factor of 10 to make the diagram more readable. 135

4.13	The last two days of a two-week simulation with repeating 48-hour operating profile with MTTES TIT control. The dashed line shows the profile requested from the plant, while red and blue correspond to the actual profiles the plant delivered.	137
4.14	The last two days of a two-week simulation with repeating 48-hour operating profile with single-tank TES TIT control. The dashed line shows the profile requested from the plant, while red and blue correspond to the actual profiles the plant delivered.	138
5.1	Flow chart of the AA-CAES design tool showing the coupling between NOMAD and CASSI.	149
5.2	Variable efficiency map of the LPC, defined as polynomial surface function, including operating bounds (black lines).	152
5.3	Variable efficiency map of the HPC, defined as polynomial surface function, including operating bounds (black lines).	152
5.4	Verification results showing the efficiency curves defined by eq. (3.60), and the maximum and minimum efficiency found by NOMAD. The three marker types indicate the maximum and minimum for each case.	153
5.5	Pareto front of the optimizations using TES-A and constant efficiencies with operating bounds.	154
5.6	Pareto front of the optimizations using TES-M and constant efficiencies with operating bounds.	156
5.7	Pareto front of the optimizations using TES-M and efficiency maps.	158
A.1	Schematic depiction of the main components of the simulation process for MTTES systems.	168

LIST OF TABLES

2.1	Operating conditions used in assessment of MTES systems.	29
2.2	Thicknesses of construction and insulation layers shown in fig. 2.4. Note: UHPC and LDC stand for ultra-high-performance and low-density concrete, respectively.	31
2.3	Thermophysical properties and costs of materials. Whenever a range of a property is given without further indication, the values are temperature-dependent as described by Zanganeh et al. [61] with the exception of *, where the temperature-dependent properties were taken from manufacturer data [64].	32
2.4	Summary of selected characteristics and key performance indicators for the systems with equal \tilde{V} highlighted by orange disks in fig. 2.5.	35
2.5	Summary of characteristics and selected key performance indicators for the systems with nearly equal $\Delta\tilde{T}_{d,out,max}$ highlighted by the orange disks in fig. 2.5.	38
2.6	Exergy loss breakdown for the systems highlighted by the orange disks in fig. 2.9.	41
2.7	Summary of characteristics and selected key performance indicators for the systems highlighted by the orange disks in fig. 2.9.	44

4.1	Design parameters of the proposed AA-CAES plant, see fig. 4.1, used in the assessment.	114
4.2	TES geometry and TCC method for three TES systems with N TES units, top and bottom radii and heights were rounded to single digits.	116
4.3	Parameters used for the model verification.	119
4.4	KPIs and additional results from the QSS single TES simulation for diabatic and adiabatic conditions.	124
4.5	KPI's and additional results from additional 48 h, and 96 h QSS single TES simulation for diabatic conditions.	125
4.6	KPIs and additional results from the QSS constant power simulation.	128
4.7	KPIs and additional results for the variable operating conditions using MTES in the two caverns.	137
5.1	Specific cost figures for the capital cost calculation.	146
5.2	Design variables for the optimization simulations.	150
5.3	Fixed plant parameters used in the optimization simulations.	151
5.4	Selected results from the Pareto front with $\Delta t = 5$ s from fig. 5.5 using TES-A and constant efficiencies.	155
5.5	Selected optimal design-point pressure values of the Pareto front with $\Delta t = 5$ s from fig. 5.5 using TES-A and constant efficiencies.	156
5.6	Selected results from the Pareto front with $\Delta t = 5$ s from fig. 5.6 using TES-M and constant efficiencies.	157
5.7	Selected results from the Pareto front with $\Delta t = 5$ s from fig. 5.7 using TES-M and variable efficiencies.	159
5.8	Selected optimal design-point pressure values of the Pareto front with $\Delta t = 5$ s from fig. 5.7 using TES-M and variable efficiencies.	159

BIBLIOGRAPHY

- [1] IPCC. *Global warming of 1.5°C*, volume 2. 2018.
- [2] C. A. Horowitz. Paris Agreement. *International Legal Materials*, 55(4), 2016. doi: 10.1017/s0020782900004253.
- [3] European Commission. A Clean Planet for all A European long-term strategic vision for a prosperous, modern, competitive and climate neutral economy. Technical Report November, 2018.
- [4] R. Ramer. Klimaziel 2050: Netto-Null Treibhausgasemissionen. Technical report, Bundesamt für Umwelt BAFU, 2020. <https://www.bafu.admin.ch/bafu/de/home/themen/klima/fachinformationen/klimaziel-2050.html>.
- [5] M. Haller, S. Ludig, and N. Bauer. Decarbonization scenarios for the EU and MENA power system: Considering spatial distribution and short term dynamics of renewable generation. *Energy Policy*, 47:282–290, 2012. doi: 10.1016/j.enpol.2012.04.069.
- [6] M. A. Delucchi and M. Z. Jacobson. Providing all global energy with wind, water, and solar power, Part II: Reliability, system and transmission costs, and policies. *Energy Policy*, 39(3):1170–1190, 2011. doi: 10.1016/j.enpol.2010.11.045.
- [7] T. M. Gür. Review of electrical energy storage technologies, materials and systems: Challenges and prospects for large-scale grid storage.

- Energy and Environmental Science*, 11(10):2696–2767, 2018. doi: 10.1039/c8ee01419a.
- [8] M. Z. Jacobson and M. A. Delucchi. Providing all global energy with wind, water, and solar power, Part I: Technologies, energy resources, quantities and areas of infrastructure, and materials. *Energy Policy*, 39(3):1154–1169, 2011. doi: 10.1016/j.enpol.2010.11.040.
- [9] Department of Energy / Office of Electricity. DOE Global Energy Storage Database. <https://www.sandia.gov/ess-ssl/global-energy-storage-database-home/>.
- [10] F. Geth, T. Brijs, J. Kathan, J. Driesen, and R. Belmans. An overview of large-scale stationary electricity storage plants in Europe: Current status and new developments. *Renewable and Sustainable Energy Reviews*, 52:1212–1227, 2015. doi: 10.1016/j.rser.2015.07.145.
- [11] W. Zappa, M. Junginger, and M. van den Broek. Is a 100% renewable European power system feasible by 2050? *Applied Energy*, 233-234(July 2018):1027–1050, 2019. doi: 10.1016/j.apenergy.2018.08.109.
- [12] K. A. Zach and H. Auer. Contribution of bulk energy storage to integrating variable renewable energies in future European electricity systems. *Wiley Interdisciplinary Reviews: Energy and Environment*, 5(4):451–469, 2016. doi: 10.1002/wene.195.
- [13] C. R. Matos, J. F. Carneiro, and P. P. Silva. Overview of Large-Scale Underground Energy Storage Technologies for Integration of Renewable Energies and Criteria for Reservoir Identification. *Journal of Energy Storage*, 21(March 2018):241–258, 2019. doi: 10.1016/j.est.2018.11.023.
- [14] B. Zakeri and S. Syri. Electrical energy storage systems: A comparative life cycle cost analysis. *Renewable and Sustainable Energy Reviews*, 42:569–596, 2015. doi: 10.1016/j.rser.2014.10.011.

- [15] F. Crotagino, K.-U. Mohmeyer, and R. Scharf. Huntorf CAES: More than 20 Years of Successful Operation. *Solution Mining Research Institute (SMRI) Spring Meeting*, (April):351–357, 2001.
- [16] M. Budt, D. Wolf, R. Span, and J. Yan. A review on compressed air energy storage: Basic principles, past milestones and recent developments. *Applied Energy*, 170:250–268, 2016. doi: 10.1016/j.apenergy.2016.02.108.
- [17] A. Sciacovelli, Y. Li, H. Chen, Y. Wu, J. Wang, S. Garvey, and Y. Ding. Dynamic simulation of Adiabatic Compressed Air Energy Storage (A-CAES) plant with integrated thermal storage - Link between components performance and plant performance. *Applied Energy*, 185:16–28, 2017. doi: 10.1016/j.apenergy.2016.10.058.
- [18] V. Tola, V. Meloni, F. Spadaccini, and G. Cau. Performance assessment of Adiabatic Compressed Air Energy Storage (A-CAES) power plants integrated with packed-bed thermocline storage systems. *Energy Conversion and Management*, 151(August):343–356, 2017. doi: 10.1016/j.enconman.2017.08.051.
- [19] L. Geissbühler, V. Becattini, G. Zanganeh, S. Zavattoni, M. Barbato, A. Haselbacher, and A. Steinfeld. Pilot-scale demonstration of advanced adiabatic compressed air energy storage, part 1: Plant description and tests with sensible thermal-energy storage. *Journal of Energy Storage*, 17:129–139, 2018. doi: 10.1016/j.est.2018.02.004.
- [20] V. Becattini, L. Geissbühler, G. Zanganeh, A. Haselbacher, and A. Steinfeld. Pilot-scale demonstration of advanced adiabatic compressed air energy storage, part 2: Tests with combined sensible/latent thermal-energy storage. *Journal of Energy Storage*, 17:140–152, 2018. doi: 10.1016/j.est.2018.02.003.
- [21] S. Kuravi, J. Trahan, D. Y. Goswami, M. M. Rahman, and E. K. Stefanakos. Thermal energy storage technologies and systems for con-

- centrating solar power plants. *Progress in Energy and Combustion Science*, 39(4):285–319, 2013. doi: 10.1016/j.pecs.2013.02.001.
- [22] U. Pelay, L. Luo, Y. Fan, D. Stitou, and M. Rood. Thermal energy storage systems for concentrated solar power plants. *Renewable and Sustainable Energy Reviews*, 79(March):82–100, 2017. doi: 10.1016/j.rser.2017.03.139.
- [23] K. Rouindej, E. Samadani, and R. A. Fraser. CAES by design: A user-centered approach to designing Compressed Air Energy Storage (CAES) systems for future electrical grid: A case study for Ontario. *Sustainable Energy Technologies and Assessments*, 35(March):58–72, 2019. doi: 10.1016/j.seta.2019.05.008.
- [24] A. Gil, M. Medrano, I. Martorell, A. Lázaro, P. Dolado, B. Zalba, and L. F. Cabeza. State of the art on high temperature thermal energy storage for power generation. Part 1-Concepts, materials and modellization. *Renewable and Sustainable Energy Reviews*, 14(1):31–55, 2010. doi: 10.1016/j.rser.2009.07.035.
- [25] S. Ströhle, A. Haselbacher, Z. R. Jovanovic, and A. Steinfeld. Upgrading sensible-heat storage with a thermochemical storage section operated at variable pressure: An effective way toward active control of the heat-transfer fluid outflow temperature. *Applied Energy*, 196:51–61, 2017. doi: 10.1016/j.apenergy.2017.03.125.
- [26] V. Becattini and A. Haselbacher. Toward a new method for the design of combined sensible/latent thermal-energy storage using non-dimensional analysis. *Applied Energy*, 247(March):322–334, 2019. doi: 10.1016/j.apenergy.2019.03.022.
- [27] M. Medrano, A. Gil, I. Martorell, X. Potau, and L. F. Cabeza. State of the art on high-temperature thermal energy storage for power generation. Part 2-Case studies. *Renewable and Sustainable Energy Reviews*, 14(1): 56–72, 2010. doi: 10.1016/j.rser.2009.07.036.

- [28] G. Zanganeh, A. Pedretti, A. Haselbacher, and A. Steinfeld. Design of packed bed thermal energy storage systems for high-temperature industrial process heat. *Applied Energy*, 137:812–822, 2015. doi: 10.1016/j.apenergy.2014.07.110.
- [29] L. Geissbühler, M. Kolman, G. Zanganeh, A. Haselbacher, and A. Steinfeld. Analysis of industrial-scale high-temperature combined sensible / latent thermal energy storage. *Applied Thermal Engineering*, 101: 657–668, 2016. doi: 10.1016/j.applthermaleng.2015.12.031.
- [30] H. Bindra, P. Bueno, and J. F. Morris. Sliding flow method for exergetically efficient packed bed thermal storage. *Applied Thermal Engineering*, 64(1-2):201–208, 2014. doi: 10.1016/j.applthermaleng.2013.12.028.
- [31] A. J. White, J. D. McTigue, and C. N. Markides. Analysis and optimisation of packed-bed thermal reservoirs for electricity storage applications. *Proceedings of the Institution of Mechanical Engineers, Part A: Journal of Power and Energy*, 230(7):739–754, 2016. doi: 10.1177/0957650916668447.
- [32] L. Geissbühler, A. Mathur, A. Mularczyk, and A. Haselbacher. An assessment of thermocline-control methods for packed-bed thermal-energy storage in CSP plants, part 1: Method descriptions. *Solar Energy*, 178(December 2018):341–350, 2019. doi: 10.1016/j.solener.2018.12.015.
- [33] L. Geissbühler, A. Mathur, A. Mularczyk, and A. Haselbacher. An assessment of thermocline-control methods for packed-bed thermal-energy storage in CSP plants, part 2: Assessment strategy and results. *Solar Energy*, 178:351–364, jan 2019. doi: 10.1016/j.solener.2018.12.016.
- [34] N. Hartmann, O. Vöhringer, C. Kruck, and L. Eltrop. Simulation and analysis of different adiabatic Compressed Air Energy Storage plant configurations. *Applied Energy*, 93:541–548, 2012. doi: 10.1016/j.apenergy.2011.12.007.

- [35] E. Barbour, D. Mignard, Y. Ding, and Y. Li. Adiabatic Compressed Air Energy Storage with packed bed thermal energy storage. *Applied Energy*, 155:804–815, 2015. doi: 10.1016/j.apenergy.2015.06.019.
- [36] S. Wang, X. Zhang, L. Yang, Y. Zhou, and J. Wang. Experimental study of compressed air energy storage system with thermal energy storage. *Energy*, 103:182–191, 2016. doi: 10.1016/j.energy.2016.02.125.
- [37] K. Rouindej, E. Samadani, and R. A. Fraser. A comprehensive data-driven study of electrical power grid and its implications for the design, performance, and operational requirements of adiabatic compressed air energy storage systems. *Applied Energy*, 257(October 2019):113990, 2020. doi: 10.1016/j.apenergy.2019.113990.
- [38] P. Zaugg. Air-storage power generating plants. *Brown Boveri Review*, 7/8:338–347, 1975.
- [39] I. Glendenning. Long-term prospects for compressed air storage. *Applied Energy*, 2(1):39–56, 1976. doi: 10.1016/0306-2619(76)90038-6.
- [40] H. U. Frutschi. Efficiency of thermal power generation in air-storage power plants. *Brown Boveri Review*, 72(3):125–129, 1985.
- [41] G. Grazzini and A. Milazzo. A thermodynamic analysis of multistage adiabatic CAES. *Proceedings of the IEEE*, 100(2):461–472, 2012. doi: 10.1109/JPROC.2011.2163049.
- [42] D. Wolf. *Methods for Design and Application of Adiabatic Compressed Air Energy Storage Based on Dynamic Modeling*. PhD thesis, 2011. <http://publica.fraunhofer.de/documents/N-154651.html>.
- [43] P. Roos, P. Gassmann, and A. Haselbacher. Compressed Air Storage Simulation, 2020. <https://cas-si.org>.
- [44] P. Zhao, L. Gao, J. Wang, and Y. Dai. Energy efficiency analysis and off-design analysis of two different discharge modes for compressed

- air energy storage system using axial turbines. *Renewable Energy*, 85: 1164–1177, 2016. doi: 10.1016/j.renene.2015.07.095.
- [45] J. Marti, L. Geissbühler, V. Becattini, A. Haselbacher, and A. Steinfeld. Constrained multi-objective optimization of thermocline packed-bed thermal-energy storage. *Applied Energy*, 216:694–708, 2018. doi: 10.1016/j.apenergy.2017.12.072.
- [46] F. W. Ahrens, A. Sharma, and K. M. Ragsdell. Optimal Design of Compressed Air Energy Storage Systems. In *6th Annual UMR-DNR Conference and Exposition on Energy*, 1979.
- [47] S. Succar, D. C. Denkenberger, and R. H. Williams. Optimization of specific rating for wind turbine arrays coupled to compressed air energy storage. *Applied Energy*, 96:222–234, 2012. doi: 10.1016/j.apenergy.2011.12.028.
- [48] W. Hong and L. Chen. Thermo-economic multi-objective optimization of adiabatic compressed air energy storage (A-CAES) system. *ACM International Conference Proceeding Series*, pages 132–138, 2018. doi: 10.1145/3194452.3194472.
- [49] S. H. Madaeni, R. Sioshansi, and P. Denholm. How thermal energy storage enhances the economic viability of concentrating solar power. *Proceedings of the IEEE*, 100(2):335–347, 2011. doi: 10.1109/JPROC.2011.2144950.
- [50] M. Schroedter-Homscheidt and S. Wilbert. *Methods to Provide Meteorological Forecasts for Optimum CSP System Operations*. Elsevier Ltd., 2017. doi: 10.1016/B978-0-08-100447-0.00008-0.
- [51] G. Wolff and S. Feuerriegel. Short-term dynamics of day-ahead and intraday electricity prices. *International Journal of Energy Sector Management*, 11(4):557–573, 2017. doi: 10.1108/IJESM-05-2016-0009.

- [52] T. Nikolakakis and V. Fthenakis. Compressed Air Energy Storage Models for Energy Arbitrage and Ancillary Services: Comparison Using Mixed Integer Programming Optimization with Market Data from the Irish Power System. *Energy Technology*, 6(7):1290–1301, 2018. doi: 10.1002/ente.201700821.
- [53] J. D. McTigue, C. N. Markides, and A. J. White. Performance response of packed-bed thermal storage to cycle duration perturbations. *Journal of Energy Storage*, 19(September):379–392, 2018. doi: 10.1016/j.est.2018.08.016.
- [54] A. Schwob, E. Cagnat, S. Chen, A. W. Chan, and C. C. Ng. Tuen Mun-Chek Lap Kok Link: An outstanding subsea tunnel project in Hong Kong. *Proceedings of the Institution of Civil Engineers: Civil Engineering*, 173(5):33–40, 2019. doi: 10.1680/jcieng.19.00027.
- [55] Y. Koyama. Present status and technology of shield tunneling method in Japan. *Tunnelling and Underground Space Technology*, 18(2-3):145–159, 2003. doi: 10.1016/S0886-7798(03)00040-3.
- [56] L. Chen, S. Jin, and G. Bu. Experimental investigation of a novel multi-tank thermal energy storage system for solar-powered air conditioning. *Applied Thermal Engineering*, 123:953–962, 2017. doi: 10.1016/j.applthermaleng.2017.05.160.
- [57] R. M. Dickinson, C. A. Cruickshank, and S. J. Harrison. Charge and discharge strategies for a multi-tank thermal energy storage. *Applied Energy*, 109:366–373, 2013. doi: 10.1016/j.apenergy.2012.11.032.
- [58] R. M. Dickinson, C. A. Cruickshank, and S. J. Harrison. Thermal behaviour of a modular storage system when subjected to variable charge and discharge sequences. *Solar Energy*, 104:29–41, 2014. doi: 10.1016/j.solener.2013.09.038.
- [59] I. Ortega-Fernández, S. A. Zavattoni, J. Rodríguez-Aseguinolaza, B. D’Aguanno, and M. C. Barbato. Analysis of an integrated packed

- bed thermal energy storage system for heat recovery in compressed air energy storage technology. *Applied Energy*, 205:280–293, 2017. doi: 10.1016/j.apenergy.2017.07.039.
- [60] B. Cárdenas and S. D. Garvey. A load-based approach for optimizing a packed-bed thermal store. *Journal of Energy Storage*, 25(February): 100835, 2019. doi: 10.1016/j.est.2019.100835.
- [61] G. Zanganeh, A. Pedretti, S. Zavattoni, M. Barbato, and A. Steinfeld. Packed-bed thermal storage for concentrated solar power - Pilot-scale demonstration and industrial-scale design. *Solar Energy*, 86(10):3084–3098, 2012. doi: 10.1016/j.solener.2012.07.019.
- [62] V. Becattini, T. Motmans, A. Zappone, C. Madonna, A. Haselbacher, and A. Steinfeld. Experimental investigation of the thermal and mechanical stability of rocks for high-temperature thermal-energy storage. *Applied Energy*, 203:373–389, 2017. doi: 10.1016/j.apenergy.2017.06.025.
- [63] P. S. Iliev, E. Giacomazzi, F. K. Wittel, M. Mendoza, A. Haselbacher, and H. J. Herrmann. Behavior of confined granular beds under cyclic thermal loading. *Granular Matter*, 21(3):1–7, 2019. doi: 10.1007/s10035-019-0914-6.
- [64] Etex Industry, Promat, Microtherm. Microtherm technical data sheet, 2017. <https://www.promat.com/siteassets/industry/downloads/technical-data-sheets-tds/microporous/eng/promat-microtherm-overstitched-product-data-sheet.pdf?v=49cc93/Download>.
- [65] F. P. Incropera. *Fundamentals of Heat and Mass Transfer*. Wiley, Hoboken, N.J, 6th ed. edition, 2007.
- [66] A. Bradshaw, A. Johnson, N. McLachlan, and Y.-T. Chiu. Heat Transfer Between Air and Nitrogen and Packed Beds of Non-Reacting Solids. *Chemical Engineering Research and Design*, 48, 1970.

- [67] F. Crotagino and P. Quast. Compressed-air storage caverns at Huntorf. In M. Bergman, editor, *Subsurface Space*, volume 2, pages 593–600, Oxford, 1980. Pergamon Press.
- [68] J. Daly, R. M. Loughlin, M. DeCorso, D. Moen, and L. Davis. CAES—reduced to practice. ASME GT2001-397, 2001.
- [69] I. Glendenning, P. E. Chew, R. Grant, R. Glanville, and M. H. Moye. Technical and economic assessment of advanced compressed air storage (ACAS) concepts. EPRI EM-1289, Electric Power Research Institute, Palo Alto, CA, 1979.
- [70] G. Grazzini and A. Milazzo. Thermodynamic analysis of CAES/TES systems for renewable energy plants. *Renewable Energy*, 33:1998–2006, 2008.
- [71] P. Zaugg. Centrales à accumulation pneumatique. In *11th International Congress on Combustion Engines*, 1977.
- [72] W. L. Oberkampf and C. J. Roy. *Verification and Validation in Scientific Computing*. Cambridge University Press, Cambridge, 2010.
- [73] H. I. H. Saravanamuttoo, G. F. C. Rogers, H. Cohen, and P. V. Straznicky. *Gas Turbine Theory*. Pearson Education Limited, 6th edition, 2009.
- [74] A. Haselbacher and P. Roos. Simple models of diabatic and adiabatic compressed air energy storage plants. Technical report, Swiss Federal Institute of Technology Zurich, Zurich, Switzerland, 2020.
- [75] P. Roos and A. Haselbacher. Thermocline control through multi-tank thermal-energy storage systems. *Applied Energy*, 281(October 2020): 115971, jan 2021. doi: 10.1016/j.apenergy.2020.115971.
- [76] J. A. Owczarek. *Fundamentals of Gas Dynamics*. International Textbook Company, Scranton, PA, 1968.

- [77] R. Kushnir, A. Ullmann, and A. Dayan. Thermodynamic models for the temperature and pressure variations within adiabatic caverns of compressed air energy storage plants. *Journal of Energy Resources Technology*, 134:021901–1 to 021901–10, 2012.
- [78] J. F. Osterle. The thermodynamics of compressed air exergy storage. *Journal of Energy Resources Technology*, 113(1):7–11, 1991.
- [79] J. Giesecke, S. Heimerl, and E. Mosonyi. *Wasserkraftanlagen: Planung, Bau und Betrieb*. Springer Vieweg, Berlin, 6th edition, 2014.
- [80] R. Kushnir, A. Dayan, and A. Ullmann. Temperature and pressure variations within compressed air energy storage caverns. *International Journal of Heat and Mass Transfer*, 55:5616–5630, 2012.
- [81] W. Zhang, X. Xue, F. Liu, and S. Mei. Modelling and experimental validation of advanced adiabatic compressed air energy storage with off-design heat exchanger. *IET Renewable Power Generation*, 14(3): 389–398, 2020. doi: 10.1049/iet-rpg.2019.0652.
- [82] A. Abdon, X. Zhang, D. Parra, M. K. Patel, C. Bauer, and J. Worlitschek. Techno-economic and environmental assessment of stationary electricity storage technologies for different time scales. *Energy*, 139: 1173–1187, 2017. doi: 10.1016/j.energy.2017.07.097.
- [83] J. Hentschel, U. Babić, and H. Spliethoff. A parametric approach for the valuation of power plant flexibility options. *Energy Reports*, 2:40–47, 2016. doi: 10.1016/j.egy.2016.03.002.
- [84] R. Jiang, F. G. Qin, B. Chen, X. Yang, H. Yin, and Y. Xu. Thermodynamic performance analysis, assessment and comparison of an advanced trigenerative compressed air energy storage system under different operation strategies. *Energy*, 186:115862, 2019. doi: 10.1016/j.energy.2019.115862.

- [85] J. Caldwell. Description of the damage in steam turbine blading due to erosion by water droplets. *Philosophical Transactions of the Royal Society of London. Series A, Mathematical and Physical Sciences*, 260 (1110):204–208, 1966.
- [86] Swissgrid. Test for secondary control capability. (November): 1–9, 2017. <https://www.swissgrid.ch/dam/swissgrid/customers/topics/ancillary-services/prequalification/4/D171130-Test-for-secondary-control-capability-V3R0-EN.pdf>.
- [87] Swissgrid. Framework Agreement for the Supply of Secondary Control Power. (October):1–14, 2016. <https://www.swissgrid.ch/dam/swissgrid/customers/topics/legal-system/ancillary-services/2/V180206-SRL-RV-EN.pdf>.
- [88] A. Sharma, H. H. Chiu, F. W. Ahrens, R. K. Ahluwalia, and K. M. Ragsdell. Design of Optimum Compressed Air Energy-Storage Systems. *Energy*, 4:201–216, 1979.
- [89] F. W. Ahrens, A. Sharma, and K. M. Ragsdell. Computer Aided Optimal Design of Compressed Air Energy Storage Systems. In *Design Automation Conference*, 1979.
- [90] M. Abramson, C. Audet, G. Couture, J. J. Dennis, S. L. Digabel, and C. Tribes. The Nomad project. <https://www.gerad.ca/nomad/>.
- [91] S. Le Digabel. Algorithm 909: NOMAD: Nonlinear Optimization with the MADS algorithm. *ACM Transactions on Mathematical Software*, 37(4):1–15, 2011.
- [92] T. Motmans. *Environmental and Economic Assessment of Advanced Adiabatic Compressed Air Energy Storage*. Master thesis, ETH Zurich, 2017.

CURRICULUM VITAE

Name	Philipp Roos
Nationality	Swiss
Citizen of	Entlebuch (LU)
Date of birth	November 9, 1990
2017–2020	Doctoral studies, Professorship of Renewable Energy Carriers, Department of Mechanical and Process Engineering, ETH Zurich. Supervisor: Prof. Dr. Aldo Steinfeld
2017–2020	Teaching assistant, Department of Mechanical and Process Engineering, ETH Zurich
2014–2017	MSc in Mechanical Engineering, ETH Zurich
2015–2016	Internship, BMW Motorsport, Munich, Germany
2010–2015	BSc in Mechanical Engineering, ETH Zurich
2012–2014	Formula Student Electric, AMZ racing team, ETH Zurich
2009	Matura at Gymnasium Lucerne Alpenquai, Lucerne, Switzerland

LIST OF PUBLICATIONS

Journal articles

P. Roos and A. Haselbacher, “Thermocline control through multi-tank thermal-energy storage systems”, *Applied Energy*, 281, January 2021.

P. Roos and A. Haselbacher, “Analytical modeling of advanced adiabatic compressed air energy storage plants”, to be submitted for publication to *Energy and Environmental Science*, 2021.

P. Roos, P. Gassmann, A. Haselbacher, “Numerical investigation of AA-CAES plant design”, to be submitted for publication to *Applied Energy*, 2021.

S. Zoller, E. Koepf, P. Roos, A. Steinfeld, “Heat Transfer Model of a 50 kW Solar Receiver-Reactor for Thermochemical Redox Cycling Using Cerium Dioxide”, *Journal of Solar Energy Engineering*, 2019.

Conference presentations (oral)

P. Roos, A. Haselbacher, A. Steinfeld, “Thermal-energy storage design and operating strategies for advanced adiabatic compressed air energy storage plants under realistic operating conditions”, ASME 13th International Conference on Energy Sustainability, Bellevue WA, USA, 2019, ES2019-4005.

P. Roos, A. Haselbacher, A. Steinfeld, “Thermal-energy storage system integration with focus on advanced adiabatic compressed air energy storage plants”, SFERA-III - 1st Doctoral Colloquium, Odeillo, France, 2019.

P. Roos, A. Haselbacher, A. Steinfeld, “Thermal energy storage: Investigation of plant and grid integration scenarios for AA-CAES applications”, 13th SOLLAB doctoral colloquium, Berlin, Germany, 2017.